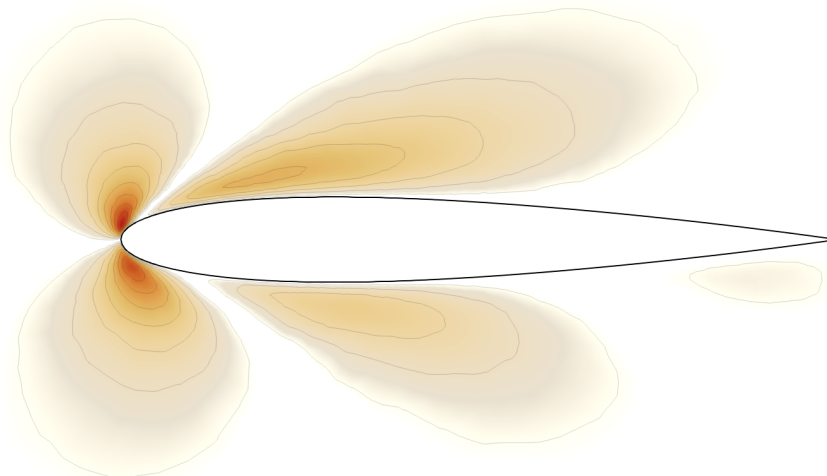


Analytical and Numerical Approaches for the Computation of Aeroelastic Sensitivities Using the Direct and Adjoint Method

Lukas Scheucher, B.Sc.
Master Thesis



SUPERVISOR:

Prof. Charbel Farhat, Dr.-Ing. Alexander Popp, Dipl.-Ing. Georg Hammerl
popp@lnm.mw.tum.de

Own work declaration

Hereby I confirm that this is my own work and I referenced all sources and auxiliary means used and acknowledged any help that I have received from others as appropriate.

(location, date)

(signature)

Abstract

Modern science and engineering is synonymous with optimization problems and the solution of constrained Partial Differential Equations (PDE). In Computational Fluid Dynamics (**CFD**) the classic approach consists of computing a flow solution, manually analyzing the results and then making empirical decisions about design changes. The new design is then evaluated again and the whole process is being iterated until a satisfying improvement is obtained.

This is not only cumbersome and unattractive, but actually unfeasible for several reasons. First of all, this approach gives not indication whether an optimum design, meaning a local minima or maxima, has been found. More over, for complex geometries, identifying the right tweaks and modifications is not straightforward, and might be unintuitive. Finally, it is simply too time consuming for big and complex problems.

The goal is therefore to do a fully automated gradient based optimization. This thesis deals with the derivation of those gradients. Particularly we look into viscous as well as turbulent flows and also generalize from a body-fitted formulation to an immersed boundary framework(**FIVER**). This thesis particularly deals with fully analytic Sensitivity Analysis (**SA**) for a number of reasons. Compared to Finite Differences (**FD**) based gradients, there is no error introduced in the gradient formulation. Moreover, only one steady state solution is necessary to obtain the gradient field. Additionally analytic gradients are generally more stable to compute than their Finite Differences (**FD**) counterparts. Finally, for the embedded formulation, we will show that **FD** sensitivities are not even well defined.

The thesis provides a general overview over the solution of flow problems via Finite Volumes (**FV**) methods and introduces the Immersed Boundary Method (**IBM**) and its implementation in details. Then, it provides the general concepts of **SA** in the fluid context. Details on the implementation on both body-fitted grids as well as immersed boundaries are also given. The thesis concludes with a verification of the implemented sensitivities. We have been able to validate the implementation of both the body-fitted and the embedded analytic sensitivities against classical **FD** based ones. A simple optimization example is shown to conclude the thesis. We close with a future outlook and some final remarks.

Zusammenfassung

In der modernen Wissenschafts- und Ingenieurswelt ist die Lösung von Optimierungsproblemen auf Basis partieller Differentialgleichung unverzichtbar geworden. In der numerischen Fluidmechanik besteht der klassische Ansatz darin eine Lösung zu berechnen. Auf Basis dieser Lösung trifft der erfahrene Ingenieur Designentscheidungen. Das Design wird dann erneut evaluiert, und dieser Prozess solange iteriert bis eine zufriedenstellende Lösung gefunden wurde.

Diese Methode hat jedoch entscheidende Nachteile, sie ist nicht nur unattraktive sondern auch unpraktikabel. Zum einen gibt es keine Indikatoren dafür, dass tatsächlich eine, in einem Gewissen Sinne optimale Lösung gefunden wurde. Darüberhinaus kann es für komplexe Geometrien und Strömungsfelder äußerst schwierig sein Entscheidungen über Designänderungen zu treffen, auch deshalb weil korrekte Verbesserungen oftmals un-intuitiv erscheinen können. Zu guter Letzt ist dieser Ansatz für praktische, große und komplexe Probleme zu Zeitaufwändig.

Die Lösung kann daher nur in einer automatisierten, Gradienten-basierten Optimierung liegen. Das ist die Motivation für die hier präsentierte Arbeit. Im speziellen betrachten wir viskose und turbulente Strömungen und verallgemeinern unsere Formulierungen auch von einer konformen Netz Formulierung hin zu einer eingebetteten nicht konformen(FIVER). Die Thesis befasst sich ausschließlich mit analytisch hergeleiteten Gradienten; diese haben entscheidende Vorteile. Zum einen wird durch eine analytische Evaluierung nicht bereits in der Formulierung der Sensitivitäten ein Approximationsfehler eingebracht. Des Weiteren, benötigt eine analytische Gradienten Evaluierung lediglich eine konvergierte Fluid Lösung, im Gegensatz zum Finite Differenzen Ansatz, und ist somit günstiger. Nicht zu unterschätzen ist auch der Gewinn an Stabilität; in der Tat werden wir im Kontext der eingebetteten Randbedingungen zeigen, dass Finite Differenzen Gradienten nicht immer wohl definiert sind.

Diese Arbeit stellt am Beginn einen generellen Überblick über die Lösung von Strömungsproblemen im Kontext von Finite Volumen Methoden bereit. Im Anschluss wird das Konzept der eingebetteten Randbedingungen näher beleuchtet, und die wichtigsten Implementierungsdetails diskutiert. Generell werden in dieser Arbeit sowohl die konformen als auch die eingebetteten Randbedingung behandelt. Im Anschluss werden die Grundgleichungen der Sensitivitätsanalyse vorgestellt und einzelne Terme, beziehungsweise deren Herleitung, näher betrachtet. Die Thesis schließt mit einer Validierung der implementierten analytischen im Vergleich zu klassisch Finite Differenzen basierten Gradienten ab, und gibt noch einen kurzen Ausblick über mögliche zukünftige Entwicklungen.

Contents

1 Basic equations of fluid mechanics	1
1.1 Eulerian and Lagrangian view	1
1.1.1 Material derivative	1
1.1.2 Eulerian derivative	2
1.2 Basic equations of fluid mechanics	2
1.2.1 Incompressible Navier Stokes Equations	3
1.2.2 Compressible Navier Stokes Equations	3
1.2.3 Euler equations	4
1.2.4 Conservative form of a Partial Differential Equation	5
1.2.5 Conservative form of the Euler equations	7
1.2.6 Equations of state	7
1.2.7 Reynolds Averaged Navier-Stokes (RANS) Equations	7
2 The Finite Volume method	11
2.1 Basic Finite Volumes formulation	11
2.2 Finite Volume method for fluid mechanics	12
2.3 Finite Elements (FE)-like treatment of the viscous term	13
2.3.1 Derivation of the mixed FV-FE formulation	15
2.4 Second Order FV methods	17
2.4.1 Linear reconstruction	17
2.4.2 The Total Variation Diminishing (TVD) property	18
2.4.3 Monotonic Upwind scheme for Conservation Laws (MUSCL) .	19
2.4.4 The Immersed Boundary Method (IBM)	19
3 Fluid structure interaction	23
3.1 Motivation	23
3.2 Coupled three-field formulation	23
3.2.1 Staggered algorithm	26
4 Optimization	29
4.1 Optimization Model	31
4.2 Design Model	33
4.3 Analysis Model	34

5 Fluid Sensitivity Analysis (SA)	37
5.1 General concepts	37
5.2 Sensitivity derivation	38
5.2.1 Calculation of $\frac{\partial q_j}{\partial s_i} \Big _{\mathbf{w}_0}$	39
5.2.2 Calculation of $\frac{\partial q_j}{\partial \mathbf{w}} \Big _{\mathbf{w}_0}$	39
5.2.3 Calculation of $\frac{d\mathbf{w}}{ds_i} \Big _{\mathbf{w}_0}$	40
5.3 Full sensitivity equation	42
6 Derivatives of the fluid residual	43
6.1 Fluid Jacobian $\frac{\partial \mathbf{R}}{\partial \mathbf{w}}$	43
6.1.1 Derivative of the convective Jacobian $\frac{\partial \mathbf{R}^c}{\partial \mathbf{w}}$	44
6.1.2 Derivative of the viscous Jacobian $\frac{\partial \mathbf{R}^v}{\partial \mathbf{w}}$	45
6.2 Analytic Jacobian of the Roe flux $\frac{\partial \phi}{\partial \mathbf{w}}$	46
6.3 Derivative with respect to the abstract variable $\frac{\partial \mathbf{R}}{\partial s}$	53
6.3.1 Convective contribution to $\frac{\partial \mathbf{R}}{\partial s}$	54
6.3.2 Viscous contribution to $\frac{\partial \mathbf{R}}{\partial s}$	55
7 Aero-elastic Sensitivity Analysis	57
7.1 Direct and adjoint approach	58
7.1.1 Direct Sensitivity Analysis for the Euler equations	60
7.1.2 Adjoint Sensitivity Analysis for the Euler equations	62
8 The Embedded Boundary Method - FIVER	65
8.1 Setup	66
8.2 Evaluation of the inviscid term at the interface	66
8.2.1 First order Finite Volume Method with exact two-phase Riemann Integrals (FIVER)	67
8.2.2 Second order FIVER	68
8.3 Evaluation of the viscous terms at the interface	69
8.3.1 Reconstruction of the fluid-state at ghost-nodes	70
8.4 Evaluation of forces	71
8.5 The level-set method	71
9 Verification	73
9.1 Approach	73
9.2 Verification of $\frac{\partial \mathbf{w}}{\partial s}$	75
9.2.1 Mach-sensitivity	75
9.2.2 Shape-sensitivity	84
9.3 Verification of Lift and Drag results	93

10 Examples	97
10.1 Lift over Drag Ratio (LDR) shape-optimization of a NACA0012 airfoil	97
10.1.1 Setup	97
10.1.2 Results	98
10.2 Multi-element airfoil with large kinematics	98
10.2.1 Setup	99
10.2.2 Results	99
11 Conclusions	101
11.1 Summary	101
11.2 Outlook	102

List of Figures

2.1	FV semi-discretization of an unstructured mesh	13
2.2	Geometric considerations on a primitive cell	16
2.3	Van Albada flux limiter function	19
2.4	Body-fitted vs. immersed wall boundary	21
3.1	Staggered algorithm scheme	26
4.1	Optimization scheme: block-diagram	30
4.2	Design-model: geometric approach	34
4.3	Design element visualization	35
5.1	Sensitivity Analysis approaches	38
6.1	Visualization of a face intersection in 3D	54
8.1	Immersed boundary method via FIVER: setup	67
8.2	Riemann problem setup	68
8.3	Ghost Point population	70
9.1	Verification setup	75
9.2	Verification $\frac{dw}{dM_\infty}$ Euler equations body-fitted	76
9.3	Verification $\frac{dw}{dM_\infty}$ Laminar equations body-fitted	77
9.4	Verification $\frac{dw}{dM_\infty}$ RANS equations body-fitted	78
9.5	Verification of $\frac{dw}{dM_\infty}$ for Euler equations, embedded	79
9.6	Verification of $\frac{dw}{dM_\infty}$ for Laminar equations, embedded	80
9.7	Verification of $\frac{dw}{dM_\infty}$ for RANS equations, embedded	81
9.8	Comparison of analytic $\frac{dw}{dM_\infty}$ for all equation types body-fitted	82
9.9	Comparison of analytic $\frac{dw}{dM_\infty}$ for all equation types embedded	83
9.10	Verification of $\frac{dw}{ds}$ Euler for equations, body-fitted	85
9.11	Verification of $\frac{dw}{ds}$ Laminar for equations, body-fitted	86
9.12	Verification of $\frac{dw}{ds}$ RANS for equations, body-fitted	87
9.13	Verification $\frac{dw}{ds}$ Euler equations embedded	88
9.14	Verification $\frac{dw}{ds}$ Laminar equations embedded	89
9.15	Verification $\frac{dw}{ds}$ RANS equations embedded	90
9.16	Comparison of analytic $\frac{dw}{dM_\infty}$ for all equation types, body-fitted	91
9.17	Comparison of analytic $\frac{dw}{dM_\infty}$ for all equation types, embedded	92

9.18	Validation of the lift and drag results for Mach-sensitivity: body-fitted Euler equations	94
9.19	Validation of the lift and drag results for Mach-sensitivity: body-fitted Laminar equations	94
9.20	Validation of the lift and drag results for Mach-sensitivity: body-fitted RANS equations	95
9.21	Validation of the lift and drag results for Mach-sensitivity: body-fitted Euler equations	95
9.22	Validation of the lift and drag results for Mach-sensitivity: body-fitted Laminar equations	96
9.23	Validation of the lift and drag results for Mach-sensitivity: body-fitted RANS equations	96
10.1	NACA0012 LDR optimization - convergence	98
10.2	NACA0012 LDR optimization - solution fields	98
10.3	Multi-element example: setup	99
10.4	Multi-element example: lift and drag	100
10.5	Multi-element example: LDR-ratio	100

Nomenclature

Operators

Algebraic operations

Q^T	Transpose of a tensor
Q^{-1}	Inverse of a tensor
\bar{q}	Average component of a quantity
q'	Fluctuating component of a quantity
$\ q\ $	Norm of a quantity
\tilde{q}	Quantity being expressed in primitive variables

Representation of scalars, tensors and other quantities

q	Scalar quantity
\mathbf{q}	Vector quantity
\mathbf{Q}	Matrix quantity
\mathbf{Q}	Tensor quantity
$ q $	Norm of a vector
Q, q	Continous quantity
Q, q	Discrete quantity
$q^{(k)}$	Iteration index in the optimization loop
$q^{(n)}$	Iteration index in the staggered algorithm
\bar{Q}	Fictitious entity
$\mathcal{O}(n)$	Order of magnitude

Analytic operations

\dot{q}	First time derivative at a fixed reference position
\ddot{q}	Second time derivative at a fixed refrence position
$\frac{\partial q_1}{\partial q_2}$	Partial derivative of one argument with respect to the other
$\frac{\partial^2 q_1}{\partial q_2^2}$	Second partial derivative of one argument with respect to the other
$\frac{Dq_1}{Dq_2}$	Material time derivative

Symbols

Numerical formulation

w	Fluid state vector
a_w	Adjoint fluid state vector
w_{RANS}	Augumented fluid state vector in the RANS formulation
\tilde{w}	Primitive fluid state vector
x	Fluid mesh position
\dot{x}	Fluid mesh motion
a_x	Adjoint fluid mesh motion
T_u	Interface projection matrix from structure to fluid mesh
T_p	Interface projection matrix from fluid to structure mesh
\mathcal{F}_{gov}	State equation of the fluid
\mathcal{S}_{gov}	State equation of the structure
\mathcal{D}_{gov}	State equation of the mesh motion
\mathbf{R}	Discrete fluid residual
u	Structure displacement
a_u	Adjoint structure displacement
H_2	Second order Jacobian of the flux
J	Jacobian of the mesh motion
\mathbf{R}^c	Convective part of the flux matrix
\mathbf{G}	Diffusive part of the flux matrix
P_F	Fluid load
P_T	Structure load
\mathbf{A}	Diagonal matrix with vell volumes
S	Source term in the RANS equations
χ	Additional fluid state variables introduced by the turbulence model

Fluid Mechanics

ρ	Density
p	Pressure
p_{tot}	Total pressure
\mathbf{v}	Fluid velocity vector
M	Mach number
e	Internal energy
E	Total energy
c	Speed of sound
\mathcal{F}	Convective fluxes
\mathcal{G}	Diffusive fluxes
ϕ	Numerical flux
\mathbb{K}	Diffusive tensor
μ	Dynamic viscosity
ν	Kinematic viscosity
μ_t	Turbulent eddy viscosity
R_e	Reynolds number
ϵ	Deviatoric fluid strain tensor
τ	Deviatoric fluid stress tensor
k	Thermal conductivity of the fluid
T	Fluid temperature
γ	Specific heat ratio
\mathbf{I}	Identity matrix
\mathbf{M}	Averaging function associated with the Roe flux
\mathcal{A}	Flux Jacobian
Λ	Diagonal matrix that contains the eigenvalues of the jacobian matrix of \mathbf{R}^c
\mathbf{P}	Matrix that contains the eigenvectors of the jacobian matrix of \mathbf{R}^c
\mathbf{A}_{Roe}	Averaging matrix of the Roe flux
\mathbf{q}	Heat flux vector

Discretization

\mathbf{X}	Mesh vertex
κ	Set of vertices
λ	Set of elements related to vertex i
\mathcal{P}_h	Primal mesh
\mathcal{C}	Dual cell
\mathcal{D}_h	Dual mesh
\mathbf{n}	Normal vector
$\boldsymbol{\nu}$	Weighted normal
n_1	x-component of the cell normal
n_2	y-component of the cell normal
n_3	z-component of the cell normal

Optimization

d	Physical design parameters
z	Target cost function
q	Optimization criterion
q	Vector of optimization criteria
s	Abstract optimization variable
s	Vector of abstract optimization variables
L	Lagrangian function of the optimization problem
ϵ^{SA}	Specified tolerance in the Sensitivity analysis
h	Equality constraints
n_h	Number of equality constraints
η	Lagrange multipliers of the equality constraints
g	Non-equality constraints
n_g	Number of non-equality constraints
γ	Lagrange multipliers of the inequality constraints
L	Lift of an airfoil
D	Drag of an airfoil
α_∞	Angle of attack

Structural Analysis

u	Displacement vector
u	Discrete displacement vector
d	Interface displacement vector
x	Mesh motion
K	FE stiffness matrix

Abbreviations

ALE	Arbitrary Lagrangian Eulerian
BFGS	Broyden-Fletcher-Goldfarb-Shanno algorithm
CFD	Computational Fluid Dynamics
CG	Conjugate Gradient
DFP	Davidon-Fletcher Powell formula
EOS	Equation of State
FV	Finite Volumes
FD	Finite Differences
FE	Finite Elements
FIVER	Finite Volume Method with exact two-phase Riemann Integrals
FRG	Farhat Research Group
FSI	Fluid Structure Interaction
GFM	Ghost Fluid Method
GFMP	Ghost Fluid Method of the Poor
GSE	Global Sensitivity Equations
IBM	Immersed Boundary Method
JWL	Jones-Wilkins-Lee
LDR	Lift over Drag Ratio
LNM	Lehrstuhl für Numerische Mechanik (Institute for Computational Mechanics)
MUSCL	Monotonic Upwind scheme for Conservation Laws
NSCE	Continuity part of the Navier Stokes Equations
NSE	Navier Stokes Equations
NSEE	Energy part of the Navier Stokes Equations
NSME	Momentum part of the Navier Stokes Equations
PCG	Preconditioned Conjugate Gradient
PDE	Partial Differential Equation

PG	Perfect Gas
RANS	Reynolds Averaged Navier-Stokes
SA	Sensitivity Analysis
SG	Stiffened Gas
SLSQP	Sequential Least Squares Programming
SQP	Sequential Quadratic Programming
TUM	Technical University of Munich
TVD	Total Variation Diminishing
VOF	Volume of Fluid Method

Chapter 1

Basic equations of fluid mechanics

Contents

1.1 Eulerian and Lagrangian view	1
1.1.1 Material derivative	1
1.1.2 Eulerian derivative	2
1.2 Basic equations of fluid mechanics	2
1.2.1 Incompressible Navier Stokes Equations	3
1.2.2 Compressible Navier Stokes Equations	3
1.2.3 Euler equations	4
1.2.4 Conservative form of a Partial Differential Equation	5
1.2.5 Conservative form of the Euler equations	7
1.2.6 Equations of state	7
1.2.7 Reynolds Averaged Navier-Stokes (RANS) Equations . .	7

1.1 Eulerian and Lagrangian view

In time dependent analytical physics there are two basic concepts of how to view a system of interest: the Eulerian and the Lagrangian approach. It shall be stressed here, that Eulerian view and Euler equations are two unrelated concepts.

The issue of Lagrangian vs. Eulerian perspective can be explained in many ways, in the end it boils down to the interpretation of the time derivative. Since we will be using the different derivatives frequently in this thesis, a short introduction shall be provided.

1.1.1 Material derivative

The material derivative of a property, is a derivative(rate of change), that follows a specific particle 'p'. That means that at every time instance the material derivative

gives as the current value of the property of a specific particle. Since in general, a particle will move its position in time quite a lot, some mean is required to track the particles motion. The material derivative is also known as the Lagrangian concept, and is commonly used in solid mechanics, since the motion of the solid particles is typically little, or at least nearly uniform over the body, which makes position tracking easy.

1.1.2 Eulerian derivative

The Eulerian derivative takes a different approach. It refers to a fixed frame of reference in the domain, and regards the rate of change of a quantity of interest at that specific position. Due to the particle movement, it typically refers to different particles at different times.

Material and Eulerian derivatives can be linked via the so-called convective rate of change as:

$$\underbrace{\frac{DG}{Dt}}_{\text{Lagrangian rate of change}} = \underbrace{\frac{\partial G}{\partial t}}_{\text{Eulerian rate of change}} + \underbrace{\mathbf{v} \cdot \nabla G}_{\text{Convective rate of change}} \quad (1.1)$$

In fluid mechanics the Eulerian concept is typically preferred.

However, when looking at fluid-structure interaction problems, the interface is typically moving. To account for that motion in the fluid, one either has to come up with a cell-intersection approach, or the fluid-mesh has to be deformed too.

An appealing and straightforward way to do so, is the so called Arbitrary Lagrangian Eulerian (**ALE**) approach. As the name suggest, it is a hybrid between Eulerian and Lagrangian point of view. The **ALE** approach allows to utilize the best of both approaches. The mesh can either be fixed, moved with the continuum in an Eulerian manner, or be moved in some arbitrarily specified manner in between. The **ALE** method can handle larger distortions than a pure Eulerian would, while still allowing to keep interface continuity between the structure and the fluid, such that no intersection of fluid cells is necessary.

In this thesis, both Eulerian and **ALE** methods will be covered. In general, no recommendation on to prefer one or the other method can be given. Instead, one should always be aware of the pros and cons of either method and choose the appropriate one for a specific problem accordingly.

For a more in depth-analysis, the interested reader is referred to [14]

1.2 Basic equations of fluid mechanics

The physics of fluid motion are governed by the so-called Navier Stokes Equations (**NSE**). These equations were derived independently of one another by Claude-Louis Navier and George Gabriel Stokes as a generalization of the Euler-equations by including viscosity effects. In general one distinguishes the incompressible and the compressible **NSE**. The validity of their application depends on the problem

setup. As a rule of thumb, flows with Mach-numbers lower than 0.3 can usually be safely approximated by the incompressible **NSE**.

The Navier Stokes equation consist of the Momentum part of the Navier Stokes Equations (**NSME**), the Continuity part of the Navier Stokes Equations (**NSCE**) and, if the compressible equations are solved, the Energy part of the Navier Stokes Equations (**NSEE**). In the literature, the term **NSE** is often synonymously used for the **NSCE**, in this thesis however, with **NSE** we will always refer to the full set of equations and will explicitly name the momentum, continuity or energy equation otherwise.

1.2.1 Incompressible Navier Stokes Equations

The incompressible Navier Stokes Equations (**NSE**) are derived by putting a few assumptions on the Cauchy stress tensor:

- Galilean invariance of the fluid stress tensor
- Isotropy of the fluid
- The stokes stress constitutive equation applies: $\tau = 2\mu\epsilon$ with $\epsilon = \frac{1}{2}(\nabla\mathbf{v} + (\nabla\mathbf{v})^T)$

In convective form, the incompressible **NSME** can be written as

$$\underbrace{\frac{\partial \mathbf{v}}{\partial t} + (\mathbf{v} \cdot \nabla) \mathbf{v}}_{\substack{\text{Inertia per volume} \\ \text{Variation}}} + \underbrace{(\mathbf{v} \cdot \nabla) \mathbf{v}}_{\substack{\text{Convection}}} - \underbrace{\nu \nabla^2 \mathbf{v}}_{\substack{\text{Diffusion}}} = - \underbrace{\nabla w}_{\substack{\text{Divergence of stress} \\ \text{Internal source}}} + \underbrace{g}_{\substack{\text{External source}}} \quad (1.2)$$

where w is the specific thermodynamic work, which satisfies

$$\nabla w = \frac{1}{\rho} \nabla p \quad (1.3)$$

And the incompressible **NSCE** can be written as

$$\nabla \cdot \mathbf{v} = 0 \quad (1.4)$$

It shall be noted, that in the incompressible **NSE**, the pressure can only be solved up to a certain constant. The pressure at a certain point therefore has to be fixed, or the system will be singular.

1.2.2 Compressible Navier Stokes Equations

Compared to the incompressible Navier Stokes Equations (**NSE**), the compressible **NSE** introduces an additional unknown, since the density can now vary. To close the system, one additional equation is required: the energy equation.

The compressible **NSE** are derived by making the following assumptions:

- Galilean invariance of the stress tensor
- Linearity of the stress in the velocity gradient: $\boldsymbol{\tau}(\nabla \mathbf{v}) = \mathbf{C} : (\nabla \mathbf{v})$, where \mathbf{C} is called the viscosity or elasticity tensor.
- Isotropy of the fluid

The compressible **NSME** can be written as

$$\frac{\partial \mathbf{v}}{\partial t} + \mathbf{v} \cdot \nabla \mathbf{v} = -\frac{\partial \rho}{\partial p} \nabla p + \nu \nabla^2 \mathbf{v} + \frac{1}{3} \nu \nabla (\nabla \cdot \mathbf{v}) + g \quad (1.5)$$

where it shall be noted that for the special case of an incompressible flow, the volume of the fluid elements is constant, resulting in a solenoidal velocity field. Thus $\nabla \cdot \mathbf{v} = 0$ and $\nabla p = 0$, which gives equation 1.2.

The **NSCE** now takes into accounts for the variable density

$$\frac{\partial \rho}{\partial t} = \nabla \cdot (\rho \mathbf{v}) = 0 \quad (1.6)$$

And finally the **NSEE** writes

$$\frac{\partial s}{\partial t} = -\mathbf{v} \cdot \mathbf{s} + \frac{Q}{T} \quad (1.7)$$

where s is the entropy per unit mass, Q is the heat transferred, and T is the temperature. F

1.2.3 Euler equations

The Euler equations can be regarded as a special case of the Navies stokes equations where the diffusive(viscous) contributions are neglected. Dimension analysis [2] reveals that this is usually justified for high Mach numbers and distant from walls. In fact, boundary Layer theory suggests that a lot of problems can be well approximated by solving the full, diffusive equations only near the wall boundary and using the Euler equations everywhere else. Although the Euler equations can be derived for both incompressible and compressible flows, the statement above suggests that only the compressible ones give actual, physically correct results. We therefore restrict our considerations to the compressible Euler equations.

Summing up, these equations can be written in convective form as

$$\begin{cases} \frac{\partial \rho}{\partial t} + \mathbf{v} \cdot \nabla \rho + \rho \nabla \cdot \mathbf{v} = 0 & \text{Continuity Equation} \\ \frac{\partial \mathbf{v}}{\partial t} + \mathbf{v} \cdot \nabla \mathbf{v} + \frac{p}{\rho} \mathbf{g} = \mathbf{g} & \text{Momentum Equation} \\ \frac{\partial e}{\partial t} + \mathbf{v} \cdot \nabla e + \frac{p}{\rho} \nabla \cdot \mathbf{v} = 0 & \text{Energy Equation} \end{cases} \quad (1.8)$$

1.2.4 Conservative form of a Partial Differential Equation

For the purpose of **FV** discretization one usually brings the equations into the so-called conservative form, which can be written generally as

$$\frac{d\boldsymbol{\xi}}{dt} + \nabla \cdot \mathbf{f}(\boldsymbol{\xi}) = \mathbf{0} \quad (1.9)$$

where $\boldsymbol{\xi}$ is the conserved quantity of interest and $\mathbf{f}(\boldsymbol{\xi})$ is denoted as "flux function". This equation can then be transformed into an integral form using the divergence theorem

$$\frac{d}{dt} \int_V \boldsymbol{\xi} dV + \int_{\partial V} \mathbf{f}(\boldsymbol{\xi}) \cdot \mathbf{n} dS \quad (1.10)$$

This equations states that the rate of change of the integral of the quantity $\boldsymbol{\xi}$ over an arbitrary control volume V is equal to the negative of the "flux" through the boundary of the control volume ∂V .

A simple choice for f would be $f(\boldsymbol{\xi}) = \boldsymbol{\xi}\mathbf{v}$, which means that the quantity $\boldsymbol{\xi}$ follows the fluid field and gives the so-called "advection equation".

Although one form is derived from the other, these two are not equivalent. Particularly, it is possible to find solutions to the integral equations that are non-differentiable and therefore not a solutions to the differential form. This leads to so called "weak solutions" and is the cause for many numerical difficulties in the finite volume simulation of such problems.

This thesis focuses on the compressible **NSE** only. They can be brought to conservative form as:

$$\frac{\partial \mathbf{w}}{\partial t} + \nabla \cdot \mathcal{F}(\mathbf{w}) + \nabla \cdot \mathcal{G}(\mathbf{w}) = \mathbf{0} \quad (1.11)$$

where, comparing to the general conservative form, one can see that $\boldsymbol{\xi} = \mathbf{w}$ and $\mathbf{f}(\boldsymbol{\xi}) = \mathcal{F}(\mathbf{w}) + \mathcal{G}(\mathbf{w})$

In the conservative form of the **NSE** the so-called "fluid state vector" \mathbf{w} is defined as

$$\mathbf{w} = \begin{bmatrix} \rho \\ \rho\mathbf{v} \\ E \end{bmatrix} \quad (1.12)$$

with

$$\mathbf{v} = \begin{bmatrix} v_1 \\ v_2 \\ v_3 \end{bmatrix} \quad (1.13)$$

denoting the fluid velocity vector.

The total energy E can be computed as a sum of the so called internal energy and the kinematic energy due to fluid velocity as

$$\underbrace{E}_{\text{total energy}} = \underbrace{\rho e}_{\text{internal energy}} + \underbrace{\frac{1}{2} \mathbf{v}^T \mathbf{v}}_{\text{kinematic energy}} \quad (1.14)$$

Bringing the convective form of the compressible NSE (1.5) into the conservative form (1.11), one can derive the convective fluxes \mathcal{F} as

$$\mathcal{F} = \mathbf{w} \mathbf{v}^T + p \begin{bmatrix} 0 \\ \mathbf{I} \\ \mathbf{v}^T \end{bmatrix} \quad (1.15)$$

$$= \begin{bmatrix} \rho \mathbf{v}^T \\ \rho (\mathbf{v} \mathbf{v}^T) + p \mathbf{I} \\ (E + p) \mathbf{v}^T \end{bmatrix} \quad (1.16)$$

$$= \begin{bmatrix} \rho v_1 & \rho v_2 & \rho v_3 \\ p + \rho v_1^2 & \rho v_1 v_2 & \rho v_1 v_3 \\ \rho v_2 v_1 & p + \rho v_2^2 & \rho v_2 v_3 \\ \rho v_3 v_1 & \rho v_3 v_2 & p + \rho v_3^2 \\ v_1(E + p) & v_1(E + p) & v_1(E + p) \end{bmatrix} \quad (1.17)$$

depending on the algorithm, one or another form can be advantageous.
The diffusive fluxes can be written as

$$\mathcal{G} = \begin{bmatrix} \mathbf{0} \\ \boldsymbol{\tau} \\ \boldsymbol{\tau} \mathbf{v} + \mathbf{q} \end{bmatrix} \quad (1.18)$$

$$= \begin{bmatrix} 0 & 0 & 0 \\ -\tau_{xx} & -\tau_{yx} & -\tau_{zx} \\ -\tau_{xy} & -\tau_{yy} & -\tau_{zy} \\ -\tau_{xz} & -\tau_{yz} & -\tau_{zz} \\ -q_x - v_1 \tau_{xx} - v_1 \tau_{yx} - v_1 \tau_{zx} & -q_y - v_1 \tau_{xy} - v_1 \tau_{yy} - v_1 \tau_{zy} & -q_z - v_1 \tau_{xz} - v_1 \tau_{yz} - v_1 \tau_{zz} \end{bmatrix}^T \quad (1.19)$$

The definition of the stress tensor depends of the fluid model used. For the simple case of a Newtonian fluid, it can be written as

$$\boldsymbol{\tau} = \mu(\nabla \mathbf{v} + (\nabla \mathbf{v})^T) + \lambda(\nabla \cdot \mathbf{v}) \mathbf{I} \quad (1.20)$$

For the relation between Temperature and heat flux an assumption has to be made. Most often, a simple Fourier's law is assumed

$$\mathbf{q} = -k \nabla T \quad (1.21)$$

1.2.5 Conservative form of the Euler equations

The Euler equations are a simplified form of the Navier-Stokes Equations (1.2)(1.5), where the viscous effects are neglected by setting $\mathcal{G} = \mathbf{0}$.

$$\frac{\partial \mathbf{w}}{\partial t} + \nabla \cdot \mathcal{F}(\mathbf{w}) = \mathbf{0} \quad (1.22)$$

The Euler equations are appropriate for a wide range of applications. A typical indicator is the Reynolds number, which describes the ratio between inertial forces and viscous forces:

$$R_e = \frac{\rho \mathbf{v} L}{\mu} = \frac{\mathbf{v} L}{\nu} \quad (1.23)$$

where L describes a characteristic length.

A high Reynolds number thus indicates that the flow is dominated by inertial forces, thus the Euler Equations should give satisfying results. However, an Euler flow lacks the ability to represent stick wall boundary conditions, thus it is unable to represent boundary layers.

1.2.6 Equations of state

Looking at the above Equations, one might notice that the number of unknowns is greater than the number of equations. Particularly, the pressure only appears in Equation (1.15) and is not linked to the other formulas. This problem is solved by introducing an Equation of State (**EOS**) that relates pressure, internal energy and density. The **EOS** depends on the fluid model, some well-known ones are: Perfect Gas (**PG**), Stiffened Gas (**SG**) or Jones-Wilkins-Lee (**JWL**).

For the simplest one, PG, the **EOS** can be written as

$$p = (\gamma - 1)\rho e \quad (1.24)$$

1.2.7 Reynolds Averaged Navier-Stokes (**RANS**) Equations

The Reynolds Averaged Navier-Stokes (**RANS**) Equations are time-averaged equations of motion for the fluid.

$$\mathbf{w} \rightarrow \bar{\mathbf{w}} = \lim_{T \rightarrow \infty} \frac{1}{T} \int_{t^0}^{t^0+T} \mathbf{w} dt \quad (1.25)$$

The main idea of the approach is to decompose an instantaneous quantity into time-averaged and fluctuating components

$$\mathbf{w} = \underbrace{\bar{\mathbf{w}}}_{time-average} + \underbrace{\mathbf{w}'}_{fluctuation} \quad (1.26)$$

When substituting this decomposition back into the **NSE**(and injecting several other approximations), a closure problem induced by the arising non-linear Reynolds stress

term $R_{eij} = -v_i' v_j'$ arises. Additional modeling is therefore required to close the **RANS** equations, which has led to many different turbulence models.

Whatever turbulence model is chosen, the fluid-state vector is augmented by the m parameters of the turbulence model

$$\boldsymbol{w}_{RANS} \leftarrow \begin{bmatrix} \boldsymbol{w} \\ \chi_1 \\ \vdots \\ \chi_m \end{bmatrix} = \begin{bmatrix} \rho \\ \rho \boldsymbol{v}^T \\ E \\ \chi_1 \\ \vdots \\ \chi_m \end{bmatrix} \quad (1.27)$$

The **RANS** equations can then be written as

$$\frac{\partial \bar{\boldsymbol{w}}}{\partial t} + \nabla \cdot \mathcal{F}(\bar{\boldsymbol{w}}) + \nabla \cdot \mathcal{G}(\bar{\boldsymbol{w}}) = \mathbf{S}(\bar{\boldsymbol{w}}, \chi_1, \dots, \chi_m) \quad (1.28)$$

Spalart Allmaras turbulence model As explained in the previous chapter, the **RANS** equations necessitate additional modeling to close the system of equations. This is typically performed by applying the Boussinesq assumption and assuming that the fluid stress tensor can be written as

$$\boldsymbol{\tau}_{ij} = 2\mu_t \left(\bar{S}_{ij} - \frac{1}{3} \frac{\partial \bar{v}_k}{\partial x_k} \delta_{ij} \right) - \frac{2}{3} \bar{\rho} k \delta_{ij} \quad (1.29)$$

$$\bar{S}_{ij} = \frac{1}{2} \left(\frac{\partial \bar{v}_i}{\partial x_j} + \frac{\partial \bar{v}_j}{\partial x_i} \right) \quad (1.30)$$

$$k = \frac{1}{2} (v_i' v_i') \quad (1.31)$$

where μ_t denotes the turbulent viscosity and k is the mean turbulent kinetic energy. Both μ_t and k need to be modeled, thus an additional two equations are required to close the system. A variety of different turbulence models have been proposed in the literature, this thesis however, focuses on the very particular case of the Spalart-Allmaras model, introduced in [26].

Herein, the last term of equation (1.29) is being neglected, thus a single additional equation is sufficient to close the system. Specifically, Spalart-Allmaras introduces the single, scalar, viscosity-like turbulent variable

$$\nu^* = \frac{\mu_t}{\bar{\rho} f_{v1}} \quad (1.32)$$

and the corresponding transport equation

$$\begin{aligned} \frac{\partial}{\partial t} (\bar{\rho} \nu^*) + \frac{\partial}{\partial x_j} (\bar{\rho} \bar{v}_j \nu^*) &= \frac{1}{\sigma} \left[\frac{\partial}{\partial x_j} \left(\bar{\rho} (\nu + \nu^*) \frac{\partial \nu^*}{\partial x_j} \right) + c_{b2} \bar{\rho} \left(\frac{\partial \nu^*}{\partial x_j} \frac{\partial \nu^*}{\partial x_j} \right) \right] + \\ &c_{b1} (1 - f_{t2}) S^* \bar{\rho} \nu^* - \bar{\rho} (c_{w1} f_w - \frac{c_{b1}}{\kappa^2} f_{t2}) \left(\frac{\nu^*}{d} \right)^2 \end{aligned} \quad (1.33)$$

with

$$f_{v1} = \frac{\chi^3}{\chi^3 + c_{v1}^3}, \quad \chi = \frac{\nu^*}{\nu}, \quad S^* = \omega + \frac{\nu^*}{k^2 d^2} f_{v2} \quad (1.34)$$

where ω is the vorticity magnitude and d is the nearest distance to the wall.

CHAPTER 1. BASIC EQUATIONS OF FLUID MECHANICS

Chapter 2

The Finite Volume method

Contents

2.1	Basic Finite Volumes formulation	11
2.2	Finite Volume method for fluid mechanics	12
2.3	FE-like treatment of the viscous term	13
2.3.1	Derivation of the mixed FV-FE formulation	15
2.4	Second Order FV methods	17
2.4.1	Linear reconstruction	17
2.4.2	The Total Variation Diminishing (TVD) property	18
2.4.3	Monotonic Upwind scheme for Conservation Laws (MUSCL)	19
2.4.4	The Immersed Boundary Method (IBM)	19

2.1 Basic Finite Volumes formulation

Like **FD** or Finite Elements (**FE**), the Finite Volumes (**FV**) method is a mean of solving a Partial Differential Equation (**PDE**) by transforming it into a discrete algebraic form. In the field of fluid mechanics, the finite volume method is the most popular approach. Other than **FD** or **FE**, the **FV** is conservative by construction. In contrast to **FD** it can easily be implemented for unstructured grids. Compared to the **FE** method, where boundary conditions come naturally from the formulation, this causes some difficulties in **FV**.

It shall also be mentioned that the introduction of stabilization schemes (like streamline upwinding), is much easier in an **FV** formulation. Overall, for **CFD**, **FV** has so far shown to be the best compromise between accuracy, stability and efficiency.

Finite volume methods are typically derived from the so called conservative form of a **PDE**. It is shown in Section 1.2.4, that the **NSE** equation can be brought to the

conservative form. In general, the conservative form can be written as:

$$\frac{d\boldsymbol{\xi}}{dt} + \nabla \cdot \mathbf{f}(\boldsymbol{\xi}) = \mathbf{0} \quad (2.1)$$

$$(2.2)$$

where $\boldsymbol{\xi}$ represents a vector of states and \mathbf{f} is the so-called flux tensor.

After subdividing the domain into finite volumes, also called cells, one can write for each particular cell i

$$\int_{V_i} \frac{d\boldsymbol{\xi}}{dt} dV_i + \int_{V_i} \nabla \cdot \mathbf{f}(\boldsymbol{\xi}) dV_i \quad (2.3)$$

It shall be stressed again that reformulating the equations in integral form has already changed the space of admissible solutions. Particularly, the integral form is capable of capturing discontinuities, like shocks whereas the derivative term would be undefined at a shock in equation (2.1).

After applying the divergence theorem to the second term this gives:

$$\frac{d}{dt} \int_{V_i} \boldsymbol{\xi} dV_i + \int_{\partial V_i} \mathbf{f}(\boldsymbol{\xi}) \cdot \mathbf{n} dS_i \quad (2.4)$$

And after integration the first term to get the volume average

$$V_i \frac{d\bar{\boldsymbol{\xi}}}{dt} + \int_{\partial V_i} \mathbf{f}(\boldsymbol{\xi}) \cdot \mathbf{n} dS_i \quad (2.5)$$

So that finally, the equation can be written as

$$\frac{d\bar{\boldsymbol{\xi}}}{dt} + \frac{1}{V_i} \int_{\partial V_i} \mathbf{f}(\boldsymbol{\xi}) \cdot \mathbf{n} dS_i \quad (2.6)$$

which can easily be interpreted: The cell average of the conserved properties changes according to the total flux through the cells surface. Of course, the conservative value is defined as being constant within one cell, so there will be different values on faces or edges, depending on which side one is looking at. There are different approaches on how to choose an appropriate value, and the choice may greatly effect the numerical properties. In a **FV** solver, the numerical flux at the interface is typically constructed such, that upwinding is achieved.

2.2 Finite Volume method for fluid mechanics

It has already been shown in Section 1.2.4, that the **NSE** can be brought into the conservative form (1.11). The flux has been shown to consist of a convective and a diffusive part(1.15)(1.18). For this thesis, a **MUSCL** type **FV** framework for unstructured three-dimensional grids, as described in [16] has been used.

In equivalent manner as in equations (2.1) to (2.6) one can now write the conservative form of the **NSE** as

$$\frac{\partial \bar{\mathbf{w}}_i}{\partial t} + \frac{1}{\|\Omega_i\|} \int_{\partial \Omega_i} \mathcal{F}(\mathbf{w}) \cdot dS + \frac{1}{\|\Omega_i\|} \int_{\partial \Omega_i} \mathcal{G}(\mathbf{w}, \nabla \mathbf{w}) \cdot dS = \mathbf{0} \quad (2.7)$$

2.3 FE-like treatment of the viscous term

It would be totally feasible to now solve both terms of equation 2.7 with classical **FV** methods. However, we note two things: First, there is no need for upwinding in the diffusive term due to its elliptic nature. Secondly, the integration of the second term also becomes much more cumbersome than the first one due to the gradient of the fluid state vector demanding at least a first order representation.

For this reasons, we introduce the following, mixed **FV-FE** formulation

$$\frac{\partial \mathbf{w}_i}{\partial t} + \int_{\partial C_i} \mathcal{F}(\mathbf{w}) \cdot dS - \int_{\Sigma_{T_i}} \mathbb{K} \mathbf{w} \nabla \phi_i dx = \mathbf{0} \quad (2.8)$$

where \mathbb{K} is the diffusive tensor introduced in [12] and ϕ_i is a linear P1 shape-function over the triangle. Please also note that the convective term is now integrated over the dual cell related to vertex i , whereas the diffusive term is integrated over all primal triangles connected to vertex i .

We will justify this re-formulation in chapter 2.3.1. See also figure 2.1.

As can be seen from Figure 2.1, the dual cells themselves can have very random shapes. This makes the integration over the boundary of the second term in Equation (2.8) more cumbersome than in a primal approach. Also, the volume integral in the **FE**-like expression has to be splitted into regular shaped subdomains, e.g. tetrahedra, such that standard integration rules, like gauss-rule, can be applied.

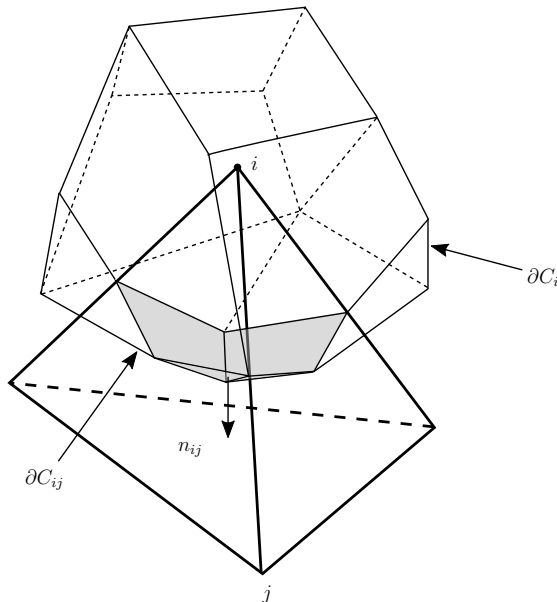


Figure 2.1: **FV** semi-discretization of an unstructured mesh. Vertex i is the center of dual cell C_i . The primal element is drawn in thick black lines, the dual cell in dashed lines. The boundary of the dual cell is denoted as ∂C_{ij}

For a closer look into the convective fluxes integral, we decompose the boundary as $\partial\Omega_i = \sum_{j \in \kappa(i)} \partial\Omega_{ij}$, where $\kappa(i)$ denotes the set of vertices connected by an edge to vertex i .

In this thesis, the surface integral in equation (2.8) is then approximated using a Riemann solver [22] and a MUSCL [28] technique. This approximation can be written as

$$\int_{\partial\Omega_i} \mathcal{F}(\mathbf{w}) \cdot dS \approx \sum_{j \in \kappa(i)} \phi_{ij}(\mathbf{w}_{ij}, \mathbf{w}_{ji}, \mathbf{n}_{ij}) \quad (2.9)$$

where ϕ_{ij} denotes the chosen numerical flux function along the edge $i - j$ and the two extrapolated fluid states at the i and the j -side of the the intersection of the cell boundary $\partial\Omega_{ij}$ and edge $i - j$ are denoted by \mathbf{w}_{ij} and \mathbf{w}_{ji} respectively. The area-weighted normal of edge $i - j$ is denoted as \mathbf{n}_{ij} .

A popular choice for the numerical approximation of the convective fluxes is the so-called Roe flux. Appropriate upwinding is directly built into the definition of the Roe flux [22]. In 1D it is defined as:

$$\phi_{ij} = \frac{1}{2} (\mathcal{F}(\mathbf{w}_j) + \mathcal{F}(\mathbf{w}_i)) - \frac{1}{2} |\mathbf{A}| (\mathbf{w}_j - \mathbf{w}_i) \quad (2.10)$$

where \mathbf{A} is the flux Jacobian.

To evaluate a roe-flux between two points in 2D or 3D, a normal vector is required to project the higher, dimensional flux on the connecting line.

As for the volume integral of the diffusive term in Equation (2.8), it shall be noted that the shape function is still defined in the primal cell. Since the gradient of the test function is constant, as is the diffusive flux itself, the integral becomes a summation of the primal sub-tetrahedral contributions.

The final numerical approximation can therefore be summarized as

$$\frac{\partial \bar{\mathbf{w}}_i}{\partial t} + \sum_{j \in \kappa(i)} \phi_{ij}(\mathbf{w}_{ij}, \mathbf{w}_{ji}, \mathbf{v}_{ij}) - \sum_{T_i \in \lambda(i)} \int_{T_j} \mathbb{K} \nabla \mathbf{w} \nabla \phi_j dx = \mathbf{0} \quad (2.11)$$

where $\kappa(i)$ is the set of vertices connected to vertex i by an edge, and $\lambda(i)$ is the set of primal elements connected to vertex i .

2.3.1 Derivation of the mixed FV-FE formulation

The equivalence of the finite volume representation of the viscous term, with the finite element-like representation provided in Equation (2.8) might not be obvious to the reader. This chapter is therefore denoted to a **FE** discretization of the governing equations, that can then be reformulated such that the mixed **FV-FE** formulation is obtained.

First, we start with the full **NSE** in conservative form, as provided in Equation (1.11). Next, a test function is defined. We chose the function $(\chi_i)_{i \in \mathcal{P}_h}$ where \mathcal{P}_h represents the primal mesh, as step functions over the dual cells of \mathcal{D}_h . A multiplication with the test-functions and subsequent integration thus gives the following weak form

$$\int_{\Omega} \frac{\partial \mathbf{w}}{\partial t} \chi_i dx + \int_{\Omega} \nabla \cdot \mathcal{F}(\mathbf{w}) \chi_i dx + \int_{\Omega} \nabla \cdot \mathcal{G}(\mathbf{w}, \nabla \mathbf{w}) \chi_i dx = \mathbf{0} \quad (2.12)$$

where by using the divergence theorem, we obtain

$$\begin{aligned} \int_{\Omega} \nabla \cdot \mathcal{F}(\mathbf{w}) \chi_i dx &= \int_{\partial C_i} \mathcal{F}(\mathbf{w}) \cdot \mathbf{n} ds \\ \int_{\Omega} \nabla \cdot \mathcal{G}(\mathbf{w}, \nabla \mathbf{w}) \chi_i dx &= \underbrace{\int_{\partial C_i} \mathbb{K} \nabla \mathbf{w} \cdot \mathbf{n} ds}_{II} \end{aligned} \quad (2.13)$$

Where the first term is already equivalent to what we have derived by the **FV** approach in (2.7).

If the diffusive tensor \mathbb{K} is approximated to be constant over the triangle, which is justified in chapter 2.3.1, the product $\mathbb{K}\mathbf{w}$ is constant, one can now write the above integral as

$$II = \sum_{T \in \mathcal{D}_i} \mathbb{K} \nabla \mathbf{w} \int_{\partial C_i \cap T} \mathbf{n}_C ds \quad (2.14)$$

Now, we use a particular geometric relation, that holds for primitive elements like triangles and tetrahedra, and is derived in Section 2.3.1

$$\int_{C_i \cap T} \mathbf{n} ds = \frac{\mathbf{n}_i^T}{2} \quad (2.15)$$

where \mathbf{n}_i^T is the normal to the primal mesh triangle T on the edge opposite of node i . This is where the geometric considerations of chapter 2.3.1 comes into place. As shown in equation (2.24), the integral over the dual face edge can be written via the normal of the primal mesh triangle as

$$-\sum_{T \in \mathcal{D}_i} \mathbb{K} \nabla \mathbf{w} \frac{\mathbf{n}_i^T}{2} \quad (2.16)$$

Also, we have shown in Section 2.3.1, that for the case of a simple triangle (but equally applicable to tetrahedra), the last term of the above equation can be written as

$$-\sum_{T \in \mathcal{D}_i} \mathbb{K} \nabla \mathbf{w} \int_T \nabla \phi_i dx \quad (2.17)$$

where ϕ_i is the P1 shape-function defined in (2.19). Finally we can go the opposite way, and join the summations over integrals over triangular contributions back to an overall integral over the whole dual cell. Doing this finally leads to

$$II = - \int_{\mathcal{D}_i} \mathbb{K} \nabla \mathbf{w} \cdot \nabla \phi_i dx \quad (2.18)$$

which is exactly the term provided in equation (2.11). Since we used the same step-function based test-functions for all terms in equation (2.12), this approach is not only consistent, for the special case of linear triangles we have shown that our finite element term is equivalent to a FV approximation.

Geometric considerations

This chapter is dedicated to the derivation of a particular link between the shape-function of a linear triangle/tetrahedra and its outward facing normals that we use in chapter 2.3.1 to proof the equivalence of the FE-formulation of the viscous term with the FV formulation.

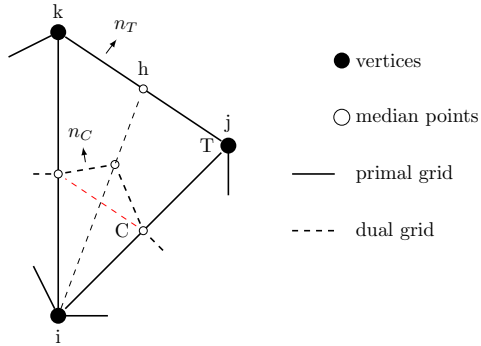


Figure 2.2: One Triangle T out of the set of triangles \sum_T , that are connected to vertex i . C denotes the dual cell related to vertex i .

We first look at one triangle of the set of triangles \sum_T that belong to node i . The setup is visualized in Figure 2.2.

The reader can easily verify, that a linear shape-function of node i can be written as:

$$\phi_i(\mathbf{x}) = \frac{\mathbf{h} \mathbf{x} \cdot \mathbf{h} i}{\|\mathbf{h} i\|^2} \quad (2.19)$$

where \mathbf{hx} is the vector from point h to any point x in the triangle, and \mathbf{hi} is the vector from point h to point i . For this particular representation of the shape function, the gradient can be elegantly written as

$$\nabla \phi_i(\mathbf{x}) = \frac{\mathbf{hi}}{\|\mathbf{hi}\|^2} = \frac{\hat{\mathbf{hi}}}{\|\mathbf{hi}\|} \quad (2.20)$$

where $\hat{\mathbf{hi}}$ is the normalized vector in $h - i$ direction. Moreover, simple geometry tells us that

$$\|\mathbf{hi}\| \|\mathbf{kj}\| = 2|T| \quad (2.21)$$

where $|T|$ is the area of the triangle T

Substituting equation 2.21 into equation 2.20 therefore leads to

$$\nabla \phi_i(\mathbf{x}) = \mathbf{hi} \cdot \frac{\|\mathbf{kj}\|}{2|T|} = -\frac{\boldsymbol{\nu}}{2|T|} \quad (2.22)$$

where $\boldsymbol{\nu}$ is the weighted outward facing normal to edge jk .

$$\boldsymbol{\nu} = -\hat{\mathbf{hi}} \|\mathbf{kj}\| = - \int_{[jk]} \mathbf{n}_T d\Gamma \quad (2.23)$$

Referring to previous chapter we remind the reader that in the vertex based FV approach, an integration over the dual face interface (dashed line in Figure 2.2) via the weighted interface normal is typically performed. By simple geometrical considerations we can now determine, that the following relation holds

$$\int_{\Gamma_C \cap T} \text{const. } \mathbf{n}_c = \frac{1}{2} \int_{\Gamma_T} \text{const. } \mathbf{n}_T \quad (2.24)$$

$$= \frac{\boldsymbol{\nu}_i^T}{2} \quad (2.25)$$

2.4 Second Order FV methods

The FV scheme, we have so far introduced in chapters 2.1, 2.2 and 2.3 is first order accurate. This chapter is dedicated to introducing the second order scheme, used in AEROF.

However, Godunov's theorem [8] states that only first-order accurate schemes can have the property of not generating new extrema(spurious oscillations)[8]. To address this problem, the concept of a flux limiter will be quickly introduced.

2.4.1 Linear reconstruction

In a classic FV scheme, a constant approximation, that represents the temporal average(see equation (2.6)) is used in each cell. The constant approximations inside

the cell makes the scheme first order. What is more, it is not able to handle shocks or discontinuities; they tend to become smeared when evolved in time.

To address this issue, a linear reconstruction is being introduced:

$$\mathbf{w}(\mathbf{x}) = \mathbf{w}_i + \nabla \mathbf{w}_i (\mathbf{x} - \mathbf{x}_i) \quad (2.26)$$

where $\nabla \mathbf{w}_i$ is being reconstructed from the neighboring fluid state values, e.g. by a simple average:

$$\nabla \mathbf{w}_i = \frac{1}{N} \sum_{j \in \kappa(i)} \frac{\mathbf{w}_j - \mathbf{w}_i}{\mathbf{x}_j - \mathbf{x}_i} \quad (2.27)$$

where $\kappa(i)$ is the set of all vertices connected to vertex i by an edge. Alternative methods like a least-square solver are also being used.

2.4.2 The Total Variation Diminishing (TVD) property

For further considerations the property of Total Variation Diminishing (TVD) shall be introduced here. In numerical methods, this is a property of a discretization used to solve hyperbolic PDE. The concept of TVD was introduced by Harten[11]. For a simple 1D case, the total variation of a solution is given as

$$TV = \int \left| \frac{\partial u}{\partial x} \right| dx \quad (2.28)$$

or in the discrete case

$$TV = \sum_i |u_{i+1} - u_i| \quad (2.29)$$

A numerical method is said to be TVD, if

$$TV(u^{n+1}) \leq TV(u^n) \quad (2.30)$$

Harten proved the that a monotone scheme is TVD and that a TVD scheme is monotonicity preserving. In CFD TVD schemes enable stable predictions of shocks on relatively coarse grids without spurious oscillations. Due to Godunov's theorem, this is crucial for second-order schemes.

Linear reconstruction, as introduced in equation (2.26), leads to schemes that are not TVD. Particularly, it has been shown that they tend to introduce spurious oscillations where shocks or discontinuities are present. This issue is being addressed in the following subsection.

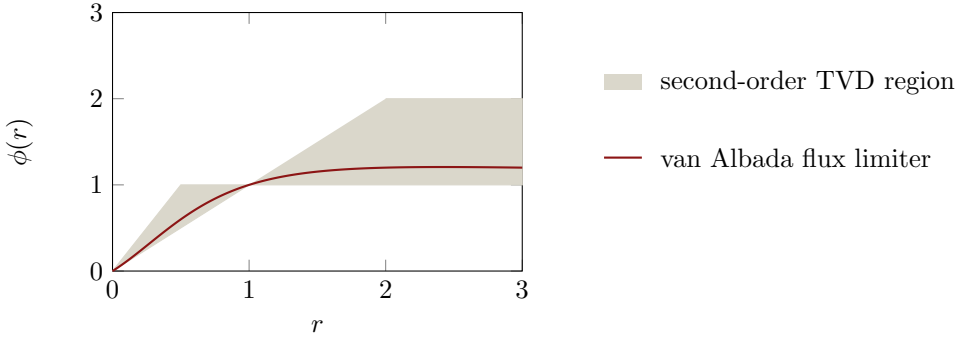


Figure 2.3: Van Albada flux limiter function. This flux limiter is second-order TVD for all values of r .

2.4.3 Monotonic Upwind scheme for Conservation Laws (MUSCL)

Monotonic Upwind scheme for Conservation Laws (MUSCL) schemes are based on the idea of using piecewise linear approximations on each cell. To counter the stability issues associated with this approach, they introduce so-called slope-limited left and right fluid states.

Instead of a pure constant or pure linear reconstruction, the following convex linear combination is considered:

$$\mathbf{w}_{i+\frac{1}{2}}^{n+} = \bar{\mathbf{w}}_i^n + \frac{1}{2}\phi_i^{n+}(\bar{\mathbf{w}}_i^n - \bar{\mathbf{w}}_{i-1}^n) \quad (2.31)$$

where the superscript $n+$ refers to time t^n and the leftward bias, and the parameter ϕ is called *slope limiter*. The slope limiter enforces a first-order accurate reconstruction near shocks ($\phi = 0$) and a second-order accurate reconstructions in the smooth regions of the flow ($\phi = 1.0$).

Many flux limiters have been proposed in the literature, and they continue to be an on-going field of research. Typically they operate on the ratio of successive gradients on the solution mesh, i.e.

$$r_i = \frac{\mathbf{w}_i - \mathbf{w}_{i-1}}{\mathbf{w}_{i+1} - \mathbf{w}_i} \quad (2.32)$$

In this thesis, we restrict ourselves to the flux limiter of Van Albada[27] expressed as

$$\phi(r) = \frac{r^2 - 2}{r^2 + 1}; \quad \lim_{r \rightarrow \infty} \phi(r) = 0 \quad (2.33)$$

It has been shown that this limiter makes a second-order, linear reconstruction scheme TVD. The van Albada flux limiter function is depicted in Figure 2.3.

2.4.4 The Immersed Boundary Method (IBM)

Traditionally internal fluid boundaries, like physical walls imposed by a structure, are represented by meshing the fluid such that it coincides with the structure surface. This approach, that shall be denoted by "explicit boundary method" here, is

intuitive and the imposition of boundary conditions comes naturally. However, in the case of fluid structure interaction, where we expect the structure to move and deform, an explicit boundary treatment, as described above, prohibits the use of an Eulerian formulation, as described in chapter 1.1. Instead every move or shape-change of the structure requires an appropriate update of the fluid mesh. Therefore, Fluid Structure Interaction (**FSI**) problems with explicit boundaries are typically solved via an **ALE** formulation. Details can be found in chapter 1.1.

However, using an **ALE**-formulation has some severe disadvantages. First and most importantly for the context of shape-optimization, only minor changes to the topology are admissible. The mesh-motion or mesh-update algorithm is only capable of moving the fluid nodes in a spatial manner, the main connectivity of the mesh does not change, however. Therefor, the method can neither cover large distortions, nor is it capable of large structure motions, e.g. removing material in a non-critical region of the structure.

Additionally, creating body-fitted meshes can be cumbersome and time consuming, especially for complex structure geometries.

An elegant solution to this problem is the so-called Immersed Boundary Method (**IBM**), first described in the context of flow-computations in the human heart in [20]. In an immersed boundary method, the structure surface does not coincide with fluid faces. Therefore, no mesh-movement algorithm is required, and the fluid mesh no longer needs to be specifically designed with a certain structure in mind. In fact, combining this approach with an adaptive mesh refinement completely eliminates the cost in fluid mesh generation.

The two different approaches are visualized in Figure 2.4. Due to the attractiveness of the immersed boundary method in the context of shape optimization, special emphasis has been put on the immersed boundary method in this thesis.

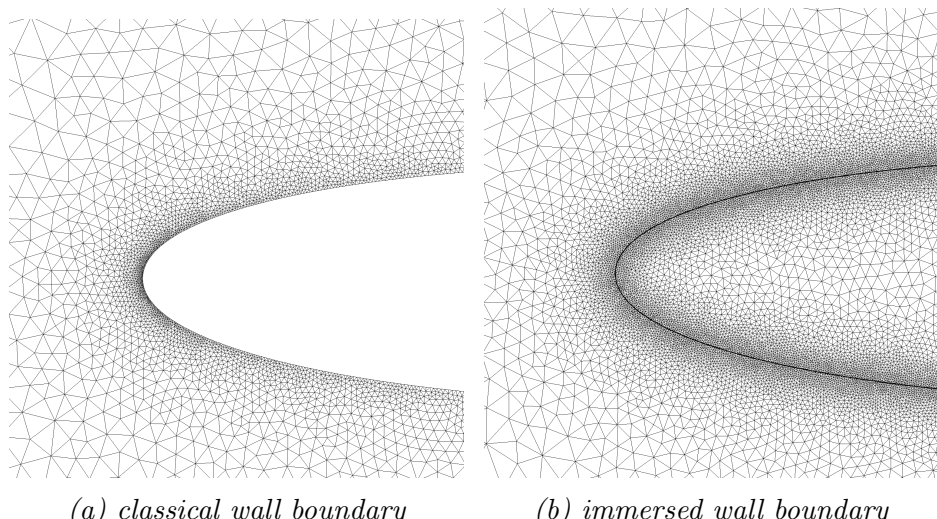


Figure 2.4: NACA0012 profile meshed with a classical wall boundary on the left versus an immersed boundary on the right. This geometry is relatively simple, for more complex examples, however, not requiring a conforming fluid grid on the interface can be a huge advantage.

Chapter 3

Fluid structure interaction

Contents

3.1 Motivation	23
3.2 Coupled three-field formulation	23
3.2.1 Staggered algorithm	26

3.1 Motivation

Fluid Structure Interaction (**FSI**) describes the aeroelastic response of a mechanical system under fluid load, as well as the interaction between fluid and structure itself. Synonymously the term "Aeroelasticity" is often used.

The ultimate goal of the Sensitivity Analysis (**SA**) derived in this thesis is shape-optimization. For many challenging applications, the interaction of the flow with the structure can not be neglected for the sensitivity computation. Thus, this chapter shall provide a quick overview on the fluid-structure sensitivity analysis.

For this thesis, we first will focus on an **ALE** formulation, a closer look into this topic in the context of en Embedded formulation will follow.

3.2 Coupled three-field formulation

In an aeroelastic ALE problem, three solution fields have to be considered. Firstly, the usual fluid problem has to be solved. Over the **FSI** interface, the fluid now interacts with the structure, imposing a Neumann problem on it. Finally, since we are considering **ALE** here, a governing equation for the fluid mesh motion has to be introduced, which closes the system.

Generally speaking, there exist two main approaches for solving this problem. Firstly, one can solve all three problems in one joint system, leading to a so-called monolithic algorithm. The advantage is, that the formulation is consistent and compared to the subsequently introduced staggered algorithm it does not introduce errors in

the coupling. However, the solution of the monolithic system is cumbersome, since completely different physics are involved.

In practice, using a so-called "staggered algorithm" has shown to be a more robust choice. In a staggered algorithm, fluid- and structure problems are updated from time step n to $n + 1$ one after the other. Therefore, consistency is lost, and (if no correction is applied) accuracy drops to first order. On the other hand each problem by itself can be treated by well established, optimized, existing solvers so the solution procedure is more robust.

This thesis utilizes the staggered approach. We have coupled a three-dimensional second order finite volume code [9] with a second order accurate finite element code[10] according to the popular three-field formulation of [5].

The three-field formulation of **ALE** aeroelasticity can be written as:

$$\text{governing equation of structure:} \quad \mathcal{S}_{gov}(\mathbf{s}, \mathbf{u}, \dot{\mathbf{x}}, \mathbf{w}) = \mathbf{0} \quad (3.1)$$

$$\text{governing equation of meshmotion:} \quad \mathcal{D}_{gov}(\mathbf{s}, \mathbf{u}, \dot{\mathbf{x}}) = \mathbf{0} \quad (3.2)$$

$$\text{governing equation of the fluid:} \quad \mathcal{F}_{gov}(\mathbf{s}, \dot{\mathbf{x}}, \mathbf{w}) = \mathbf{0} \quad (3.3)$$

Governing equation of the structure: For a simple linear case, that is assumed in this thesis, the structure state equation can be written as

$$\mathcal{S}_{gov} = \mathbf{K}\mathbf{u} - \mathbf{P}(\dot{\mathbf{x}}, \mathbf{w}) \quad (3.4)$$

where \mathbf{K} represents the finite element stiffness matrix and \mathbf{P} denotes the external load vector that combines aerodynamic loads \mathbf{P}_F that are inflicted onto the structure by the fluid, and gravity loads \mathbf{P}_0

$$\mathbf{P} = \mathbf{P}_0 + \mathbf{P}_F \quad (3.5)$$

Governing equation of the mesh motion: In an Arbitrary Lagrangian Eulerian formulation, the fluid mesh deforms with the structure. A governing equation is thus required to describe that deformation. Typically a simple linear pseudo finite element approach or a spring analogy method [3] is used to do so. A Dirichlet problem is solved to move the mesh.

$$\mathcal{D}_{gov} = \bar{\mathbf{K}}\dot{\mathbf{x}} \quad \text{with} \quad \dot{\mathbf{x}} = \mathbf{u} \text{ on } \Gamma_{F|S} \quad (3.6)$$

Governing equation of the fluid: The state equation of the fluid depends on the flow model used, as well as on whether a Eulerian or Lagrangian approach is used. A quick overview is provided in Section 1.2.

Please note, that the frame of reference(Eulerian, Lagrangian, Arbitrary Lagrangian Eulerian) has nothing to do with the fluid equation type.

3.2. COUPLED THREE-FIELD FORMULATION

The state equation of the fluid (3.3) can be expressed as

$$\mathcal{F}_{gov} = \begin{array}{|c|c|c|} \hline & \text{Eulerian} & \frac{\partial \mathbf{w}}{\partial t} + \nabla \mathcal{F}(\mathbf{x}, \mathbf{w}) \\ \hline & \text{NSE} & \frac{\partial \mathbf{w}}{\partial t} + \nabla \mathcal{F}(\mathbf{x}, \mathbf{w}) + \nabla \mathcal{G}(\mathbf{x}, \mathbf{w}) \\ \hline & \text{RANS} & \frac{\partial \mathbf{w}}{\partial t} + \nabla \mathcal{F}(\mathbf{x}, \mathbf{w}) + \nabla \mathcal{G}(\mathbf{x}, \mathbf{w}) - \mathcal{S}(\mathbf{x}, \mathbf{w}, \chi) \\ \hline & \text{ALE} & \frac{\partial \mathbf{Jw}}{\partial t} + \mathbf{J} \nabla_{\xi} \mathcal{F}^c(\mathbf{x}, \dot{\mathbf{x}}, \mathbf{w}) \\ \hline & \text{NSE} & \frac{\partial \mathbf{Jw}}{\partial t} + \mathbf{J} \nabla_{\xi} \mathcal{F}^c(\mathbf{x}, \dot{\mathbf{x}}, \mathbf{w}) + \mathbf{J} \nabla_{\xi} \mathcal{G}^c(\mathbf{x}, \dot{\mathbf{x}}, \mathbf{w}) \\ \hline & \text{RANS} & \frac{\partial \mathbf{Jw}}{\partial t} + \mathbf{J} \nabla_{\xi} \mathcal{F}^c(\mathbf{x}, \dot{\mathbf{x}}, \mathbf{w}) + \mathbf{J} \nabla_{\xi} \mathcal{G}^c(\mathbf{x}, \dot{\mathbf{x}}, \mathbf{w}) - \mathcal{S}^c(\mathbf{x}, \dot{\mathbf{x}}, \mathbf{w}, \chi) \\ \hline \end{array} = \mathbf{0} \quad (3.7)$$

where

$$\mathcal{F}^c(\mathbf{w}) = \mathcal{F}(\mathbf{w}) - \dot{\xi} \mathbf{w} \quad (3.8)$$

After **FV** discretization of the convective part, and **FE** discretization of the diffusive part, as explained in chapter 2.2, the discrete system can be written as

$$\mathcal{F}_{gov} = \begin{array}{|c|c|c|} \hline & \text{Eulerian} & \frac{\partial \mathbf{w}}{\partial t} + \mathbf{R}^c(\mathbf{x}, \mathbf{w}) \\ \hline & \text{NSE} & \frac{\partial \mathbf{w}}{\partial t} + \mathbf{R}^c(\mathbf{x}, \mathbf{w}) + \mathbf{G}(\mathbf{x}, \mathbf{w}) \\ \hline & \text{RANS} & \frac{\partial \mathbf{w}}{\partial t} + \mathbf{R}^c(\mathbf{x}, \mathbf{w}) + \mathbf{G}(\mathbf{x}, \mathbf{w}) - \mathbf{S}(\mathbf{x}, \mathbf{w}, \chi) \\ \hline & \text{ALE} & \frac{\partial \mathbf{A(x)w}}{\partial t} + \mathbf{R}^c(\mathbf{x}, \dot{\mathbf{x}}, \mathbf{w}) \\ \hline & \text{NSE} & \frac{\partial \mathbf{A(x)w}}{\partial t} + \mathbf{R}^c(\mathbf{x}, \dot{\mathbf{x}}, \mathbf{w}) + \mathbf{G}(\mathbf{x}, \dot{\mathbf{x}}, \mathbf{w}) \\ \hline & \text{RANS} & \frac{\partial \mathbf{A(x)w}}{\partial t} + \mathbf{R}^c(\mathbf{x}, \dot{\mathbf{x}}, \mathbf{w}) + \mathbf{G}(\mathbf{x}, \dot{\mathbf{x}}, \mathbf{w}) - \mathbf{S}(\mathbf{x}, \dot{\mathbf{x}}, \mathbf{w}, \chi) \\ \hline \end{array} = \mathbf{0} \quad (3.9)$$

Where we remind the reader that, as explained in chapter 2.2, for a **FV** discretization, the fluid state \mathbf{w} has to be interpreted as average value over the cell. We often take the cell average to be equal to the value at the cell center, an approximation that is second order accurate.

In the above equations \mathbf{R}^c denotes the vector of Roe fluxes resulting from a second-order finite volume discretization of the convective part of the **NSE**, see chapter 2.2. Likewise, \mathbf{G} denotes an approximation of the diffusive part. As explained in chapter 2.3 we chose a **FE** approximation over a **FV** one for this term.

\mathbf{A} denotes the matrix of cell volumes and \mathbf{S} denotes the matrix resulting from the additional turbulence closures in the **RANS** equations (see Section 1.2.7).

The above table also gives a very nice overview over the different equation types and the used simplifications. The Euler equations are obviously obtained by neglecting the diffusive part of the **NSE**. One can also see that the **RANS** equations are more difficult than the **NSE** themselves. However, as explained in 1.2.7, the advantage is that **RANS** can operate on much coarser meshes that do not have to resolve the small scale turbulence phenomena, which makes them more numerically efficient overall in many applications.

3.2.1 Staggered algorithm

The three-field coupled system of equations (3.1)-(3.3), can be solved very efficiently with an iterative staggered procedure, such as the one proposed by [5]. This work utilizes the second-order staggered algorithm described in Figure 3.1.

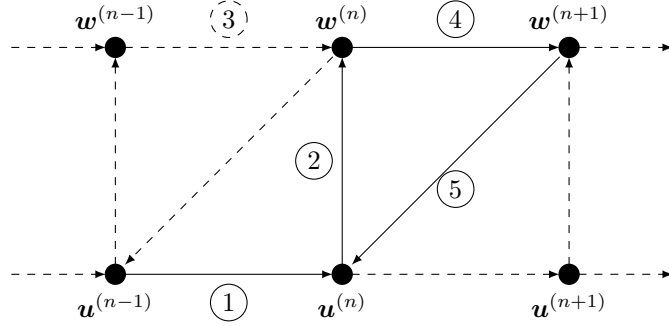


Figure 3.1: Scheme for the staggered algorithm. The picture depicts the sequential structure(\mathbf{u}) and fluid(\mathbf{w}) solves. First, the structure is updated to a new time step. With this information, a corresponding fluid solution is obtained. After the fluid is progressed in time, the structure solutions is being corrected with that information. A detailed description of all steps follows below.

① Determining structural response For a given external load $\mathbf{P}^{(n)}$, the structural response $\mathbf{u}^{(n)}$ is determined by solving the state equation of the structure (3.1). To increase stability, and under-relaxation is typically performed:

$$\mathbf{u}^{(n)} = (1 - \theta)\mathbf{u}^{(n-1)} + \theta\tilde{\mathbf{u}} \quad (3.10)$$

$$\tilde{\mathbf{u}} = \mathbf{K}^{-1}\mathbf{P}^{(n)} \quad (3.11)$$

Typically, the relaxation factor is chosen as $0.5 \leq \theta \leq 0.9$

② Motion transfer to wet surface The motion of the wet surface of the structure has to be transformed to the fluid.

$$\mathbf{u}_T^{(n)} = \mathbf{T}_u \mathbf{u}^{(n)} \quad (3.12)$$

where \mathbf{T}_u is a transfer matrix that also accounts for potentially non-matching meshes [18].

③ Fluid mesh motion update The fluid mesh motion is then updated by solving an auxiliary pseudo-Dirichlet problem on the fluid mesh. This step is at the very heart of the ALE algorithm.

$$\bar{\mathbf{K}}\dot{\mathbf{x}}^{(n)} = 0 \quad \dot{\mathbf{x}}^{(n)} = \mathbf{u}_T^{(n)} \text{ on } \Gamma_{F|S} \quad (3.13)$$

3.2. COUPLED THREE-FIELD FORMULATION

where the Dirichlet conditions are introduced into the system via a decomposition:

$$\bar{\mathbf{K}} = \begin{bmatrix} \bar{\mathbf{K}}_{\Omega\Omega} & \bar{\mathbf{K}}_{\Omega\Gamma} \\ \bar{\mathbf{K}}_{\Gamma\Omega} & \bar{\mathbf{K}}_{\Gamma\Gamma} \end{bmatrix}, \quad \dot{\mathbf{x}} = \begin{bmatrix} \dot{\mathbf{x}}_\Omega \\ \dot{\mathbf{x}}_\Gamma \end{bmatrix} \quad (3.14)$$

Here, the subscript Γ denotes the fluid grid points at the FSI interface and the subscript Ω denotes the remainder. Hence, the fluid mesh is updated in two steps, by first transferring the structure motion to the fluid interface, and then solving the auxiliary pseudo Dirichlet problem:

$$\dot{\mathbf{x}}_\Gamma^{(n)} = \mathbf{T}_u \mathbf{u}^{(n)} \quad (3.15)$$

$$\bar{\mathbf{K}}_{\Omega\Omega} \dot{\mathbf{x}}_\Omega^{(n)} = -\bar{\mathbf{K}}_{\Omega\Gamma} \dot{\mathbf{x}}_\Gamma^{(n)} \quad (3.16)$$

It shall be noted that an exact solution of the preceding equation is not required. In fact it is an arbitrarily chosen auxiliary pseudo-problem anyway. Therefor, a valid update of the mesh motion, that does not produce crossovers is enough. Such an update can be obtained at low cost by applying a few Preconditioned Conjugate Gradient (**PCG**) iterations to Equation (3.16).

④ Update fluid state vector After the mesh has been deformed, the fluid state \mathbf{w} vector can be updated by applying a singe Newton Rapsodon iteration to equation (3.9), which leads to.

Eulerian	Euler	$\mathbf{R}^c(\mathbf{x}^{(n+1)}, \mathbf{w}^{(n)}) + \frac{\partial \mathbf{R}^c}{\partial \mathbf{w}}(\mathbf{x}^{(n+1)}, \mathbf{w}^{(n+1)} - \mathbf{w}^{(n)})$	$= 0$
	NSE	$< \text{term above} > + \frac{\partial \mathbf{G}}{\partial \mathbf{w}}(\mathbf{x}^{(n+1)}, \mathbf{w}^{(n+1)} - \mathbf{w}^{(n)})$	
	RANS	$< \text{term above} > - \frac{\partial \mathbf{S}}{\partial \mathbf{w}}(\mathbf{x}^{(n+1)}, \mathbf{w}^{(n+1)} - \mathbf{w}^{(n)}, \boldsymbol{\chi})$	
ALE	Euler	$\mathbf{R}^c(\mathbf{x}^{(n+1)}, \dot{\mathbf{x}}^{(n+1)}, \mathbf{w}^{(n)}) + \frac{\partial \mathbf{R}^c}{\partial \mathbf{w}}(\mathbf{x}^{(n+1)}, \dot{\mathbf{x}}^{(n+1)}, \mathbf{w}^{(n+1)} - \mathbf{w}^{(n)})$	$= 0$
	NSE	$< \text{term above} > + \frac{\partial \mathbf{G}}{\partial \mathbf{w}}(\mathbf{x}^{(n+1)}, \dot{\mathbf{x}}^{(n+1)}, \mathbf{w}^{(n+1)} - \mathbf{w}^{(n)})$	
	RANS	$< \text{term above} > - \frac{\partial \mathbf{S}}{\partial \mathbf{w}}(\mathbf{x}^{(n+1)}, \dot{\mathbf{x}}^{(n+1)}, \mathbf{w}^{(n+1)} - \mathbf{w}^{(n)}, \boldsymbol{\chi})$	

(3.17)

⑤ Determining structural responses Once the new fluid-state vector has been determined, the pressure $p^{(n+1)}$ can be recovered. The pressure on the fluid interface side, than might need to be transferred to the structure via a transfer matrix \mathbf{T}_u to account for potentially non-matching fluid-structure interfaces.

CHAPTER 3. FLUID STRUCTURE INTERACTION

Chapter 4

Optimization

Contents

4.1	Optimization Model	31
4.2	Design Model	33
4.3	Analysis Model	34

As mentioned in the introduction, the overall motivation for this thesis is optimization. A typical optimization process, not restricted to fluid problems, is depicted in Figure 4.1.

A generic, aeroelastic optimization problem can be written as

$$q(\mathbf{s}, \mathbf{u}, \mathbf{w}) \left\{ \begin{array}{l} \min_{\mathbf{s}} z(\mathbf{s}) \\ \mathbf{h}(\mathbf{s}) = \mathbf{0}, \quad \mathbf{h} \in \mathbb{R}^{n_h} \\ \mathbf{g}(\mathbf{s}) > \mathbf{0}, \quad \mathbf{g} \in \mathbb{R}^{n_g} \end{array} \right. \quad (4.1)$$

$$\mathbf{s} = \{\mathbf{s} \in \mathbb{R}^{n_s} | \mathbf{s}_L \leq \mathbf{s} \leq \mathbf{s}_U\} \quad (4.2)$$

Here, z is an arbitrary cost function that should be minimized. Note that a maximization problem can easily be obtained by multiplying the cost function by a factor of -1 . In aerodynamics, a typical example for a cost function would be the LDR of an airfoil. The cost-function is described in terms of so-called *abstract variables*. These can have some physical interpretation, but don't necessarily have to (see section 4.2). Since typically, these optimization problems have no finite solution on an unbounded domain, some restrictions/conditions are introduced. In the airfoil example, we would probably specify a minimum lift that is required to support the configuration. Also a maximum stress for the structure will likely have to be specified. These are classical examples of non-equality constraints, denoted by $\mathbf{g}(\mathbf{s})$ in the above formulation. Constraints can also be formulated in an equality sense, for instance geometrical restrictions due to the turbine suspensions.

Furthermore, the abstract optimization variables \mathbf{s} themselves are typically restricted by lower(\mathbf{s}_L) and upper(\mathbf{s}_U) bounds.

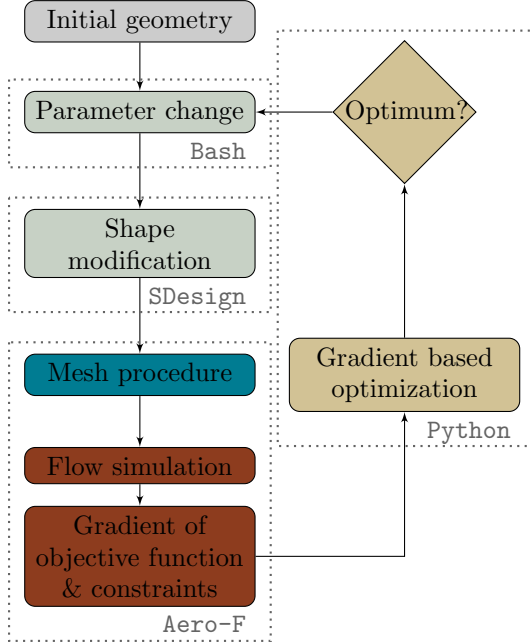


Figure 4.1: Flow chart of an optimization process in the context of flow simulations. If one regards the flow-computation as a black-box to compute gradients of an objective function and the shape-modification block more general as parameter modification, this optimization routine is applicable to all kinds of problems. In our case, we begin with an initial geometry created by a standard mesh-generation software. We also parametrize the initial mesh in terms of design elements in this first step. This is done via SDesign[7] in this thesis. All further modifications to the geometry are obtained via the design element concept. The mesh-movement, steady-state simulations and Sensitivity Analysis (SA) are then performed in AERO-F[9]. For the optimizer itself, python has been chosen in this thesis, more specifically the `pyOpt` module. The codes communicate via result-files. These files are used to monitor and investigate the optimization process.

The combinations of objective function z and constraints \mathbf{h} and \mathbf{g} is typically denoted as optimization criteria q .

$$\begin{aligned} q &= q(\mathbf{s}, \mathbf{u}, \mathbf{w}) \\ \mathbf{u} &= \mathbf{u}(\mathbf{s}), \quad \mathbf{w} = \mathbf{w}(\mathbf{s}) \end{aligned} \tag{4.3}$$

This thesis follows the *nested analysis and design approach*, meaning that we assume that \mathbf{u} and \mathbf{w} always satisfy the aeroelastic state equations. This means that the state equations are not included in the set of constraints, but the structural displacements \mathbf{u} and the fluid state variables \mathbf{w} are determined in each iteration. As [18] write, the aeroelastic optimization problem can typically be solved by combining three different numerical approaches:

- Optimization Model
- Design Model

- Analysis Model

The optimization model describes the solution of the generic optimization problem(4.1)-(4.2). For this thesis, a Sequential Quadratic Programming (**SQP**) has been chosen [1].

The design model links abstract optimization variables \mathbf{s} to actual shapes, structures, geometries or aerodynamics design parameters. For this purpose SDESIGN, a program specifically written for **SA** purpose in the Farhat Research Group (**FRG**), has been used during this thesis. Its basic concepts and ideas are described in [19]. Finally, the analysis model provides concepts of evaluation the optimization criteria. Typically, the optimization criteria depend on \mathbf{u} and \mathbf{w} which is why a coupled system of equations has to be solved in every design optimization step. The Sensitivity Analysis (**SA**) is also part of this model. Aeroelastic analysis and Sensitivity analysis are discussed in Section 7.

4.1 Optimization Model

Optimization problems are typically solved by gradient-based methods. The methods are divided into

- Primal
- Dual
- Penalty-barrier and
- Lagrange approaches

This thesis focuses on Lagrange approaches. For a thorough analysis and comparison of the different approaches, the interested reader is referred to [23].

The Lagrangian approach formulates the optimization problem(4.1)(4.2) as an extreme value problem of the Lagrangian:

$$L(\mathbf{s}, \boldsymbol{\eta}, \boldsymbol{\gamma}) = z(\mathbf{s}) = \boldsymbol{\eta}^T \mathbf{h}(\mathbf{s}) + \boldsymbol{\gamma}^T \mathbf{g}(\mathbf{s}) \quad (4.4)$$

Here, $\boldsymbol{\eta}$ denote the Lagrange multipliers for the equality constraints and $\boldsymbol{\gamma}$ the Lagrange multipliers for the non-equality constraints. In fact, one can easily see that the original optimization problem can be obtained as saddle point of the Lagrangian:

$$\begin{aligned} \frac{\partial L}{\partial \mathbf{s}} &= \frac{\partial z}{\partial \mathbf{s}} = \boldsymbol{\eta}^T \frac{\partial \mathbf{h}}{\partial \mathbf{s}} + \boldsymbol{\gamma}^T \frac{\partial \mathbf{g}}{\partial \mathbf{s}} \\ \frac{\partial L}{\partial \boldsymbol{\eta}} &= \mathbf{h} = \mathbf{0} \\ \frac{\partial L}{\partial \boldsymbol{\gamma}} &= \boldsymbol{\gamma}^T \mathbf{g} = \mathbf{0} \end{aligned} \quad (4.5)$$

The **SQP** method, mention before uses a Newton-Rhaphson algorithm to solve the above system.

$$\begin{bmatrix} \frac{\partial^2 L}{\partial s^2} & \frac{\partial \mathbf{g}}{\partial s}^{(k)} & \frac{\partial \mathbf{h}}{\partial s}^{(k)} \\ \gamma^{(k)} \frac{\partial \mathbf{g}}{\partial s}^{(k)} & \mathbf{h}^{(k)} & \mathbf{0} \\ \frac{\partial \mathbf{h}}{\partial s}^{(k)} & \mathbf{0} & \mathbf{0} \end{bmatrix} \begin{bmatrix} \Delta \mathbf{s} \\ \Delta \boldsymbol{\gamma} \\ \Delta \boldsymbol{\eta} \end{bmatrix} = - \begin{bmatrix} \frac{\partial L}{\partial \mathbf{s}}^{(k)} \\ \gamma^{(k)T} \mathbf{g}^{(k)} \\ \mathbf{h}^{(k)} \end{bmatrix} \quad (4.6)$$

Here $(\cdot)^{(k)}$ denotes the iteration index of the optimization loop.

The linear Equations (4.6) can also be formulated as an equivalent quadratic minimization problem:

$$\begin{aligned} \min_{\mathbf{s}} \quad & \left(\frac{1}{2} \Delta \mathbf{s}^T \frac{\partial^2 L}{\partial \mathbf{s}^2}^{(k)} \Delta \mathbf{s} + \frac{\partial z}{\partial \mathbf{s}}^{(k)} \right) \\ \text{subject to} \quad & \frac{\partial \mathbf{g}}{\partial s}^{(k)} \Delta \mathbf{s} + \mathbf{g}^{(k)} \geq \mathbf{0} \\ & \frac{\partial \mathbf{h}}{\partial s}^{(k)} \Delta \mathbf{s} + \mathbf{h}^{(k)} = \mathbf{0} \end{aligned} \quad (4.7)$$

In the above formulation, the evaluation of the second derivative of the Lagrangian (Hessian of L) is the numerically most expensive part. Usually it is preferred to approximate it by a first-order information, for example by the Davidon-Fletcher-Powell formula (**DFP**) or by the Broyden-Fletcher-Goldfarb-Shanno algorithm (**BFGS**) method. However, this simplification introduces an error that one should be aware of. Some correction methods have been proposed trying to minimize the error. In this thesis we adapt the one proposed by [18]:

$$\begin{bmatrix} \mathbf{s}^{(k+1)} \\ \boldsymbol{\eta}^{(k+1)} \\ \gamma^{(k+1)} \end{bmatrix} = \begin{bmatrix} \mathbf{s}^{(k)} \\ \boldsymbol{\eta}^{(k)} \\ \gamma^{(k)} \end{bmatrix} + \alpha^{(k)} \begin{bmatrix} \Delta \mathbf{s}^{(k)} \\ \Delta \boldsymbol{\eta}^{(k)} \\ \Delta \boldsymbol{\gamma}^{(k)} \end{bmatrix} \quad (4.8)$$

The appropriate step size $\alpha^{(k)}$ is determined by a line search. As [18] write, due to this insufficiencies, the Lagrangian can not be used to measure an improvement. Instead, a merit function is introduced that is minimized by the line-search. A local minimum is reached by following a sequence of decreasing merit function values. Convergence of the process can be measured via the \mathcal{L}_2 -norm of the residual of the Kuhn-Tucker conditions (4.5).

By construction, the constraints are satisfied only when the optimum point is reached.

4.2 Design Model

The design model represent the essential link between the described optimization model and the analysis model. Generally speaking, it relates physical design parameters to abstract ones.

$$\mathbf{d} = \mathbf{d}(\mathbf{s}), \quad \mathbf{d} \in \mathbb{R}^{n_d} \quad (4.9)$$

Here, n_d denotes the number of physical design parameters. To define a relation between the abstract optimization variables and the motion of the nodes, the following design model is introduced:

$$\dot{\mathbf{x}} = \dot{\mathbf{x}}(\mathbf{s}) \quad (4.10)$$

As [18] explain, it is unpractical to identify an abstract variable directly with an increment of the coordinate of a grid point. Instead, two approaches, namely geometrical and mechanical can be adopted for constructing the generic design model.

Mechanical approach In the mechanical approach, the shape variation is identified with a superposition of fictitious structural deformations $\bar{\mathbf{u}}_j$ due to fictitious loads $\mu_j \bar{\mathbf{P}}_j$ and fictions support conditions

$$\dot{\mathbf{x}} = \sum_j \bar{\mathbf{u}}_j = \sum_j \bar{\mathbf{K}}_j^{-1} \mu_j \bar{\mathbf{P}}_j \quad (4.11)$$

where $\bar{\mathbf{K}}_j$ is a fictitious pseudo structure stiffness matrix representing the fluid domain compatible to the current fictions support conditions.

Geometrical approach The geometrical approach describes the geometry of the structure or the fluid boundary the design element concept. Here, the shape of a body \mathbf{X} is approximated by so-called design elements as follows:

$$\mathbf{X} = \sum_j \phi_j(\xi) \hat{\mathbf{X}}_j \quad (4.12)$$

Here, $\phi_j(\xi)$ is a shape function, $\hat{\mathbf{X}}_j$ is the vector of control nodes and ξ represents the reference coordinate. In the design element concept, the variation of the control nodes of the design element is used to vary the shape of the body. The variation of the control nodes position denoted as "mesh-motion" is given as $\mathbf{x} = \Delta \hat{\mathbf{X}}$

$$\dot{\mathbf{x}} = \sum_j \phi_j(\xi) \dot{\hat{\mathbf{x}}}_j \quad (4.13)$$

Just as in Finite Elements (**FE**), where the shape-functions can not only be used to describe the solution field, but also the body's geometry and material parameters, the design element concept can be applied to prescribe parameter distributions and their variations in the optimization process. A simple sketch of the concept is provided in Figure 4.2

Both approaches have pros and cons, that are quickly discussed in [19], this thesis utilizes the geometrical approach solemnly.

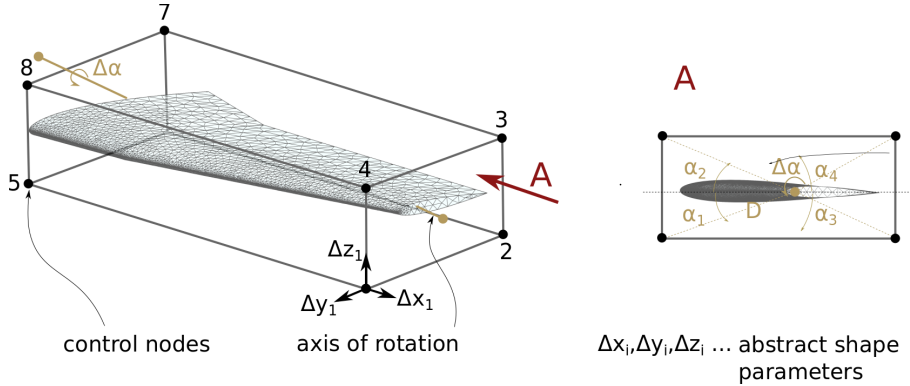


Figure 4.2: Geometrical approach for the design model as explained in Section 4.2. A NACA type airfoil is considered here as an example. The airfoil is embedded in a bounding box defined by eight so-called control nodes. The position of these control nodes can be varied, which alternates the shape of the airfoil according to some interpolation functions defined on the nodes. The 24 displacement unknowns are denoted as "abstract shape parameters". Abstract shape variables can be arbitrarily defined. As an example, a rotation axis is defined through the wing.

4.3 Analysis Model

In the analysis model, the optimization criteria q are determined for a given set of optimization variables s . Since the optimization algorithm chosen in this thesis is based on gradients, the gradients of the optimization criteria with respect to the abstract variables are determined in this step.

4.3. ANALYSIS MODEL

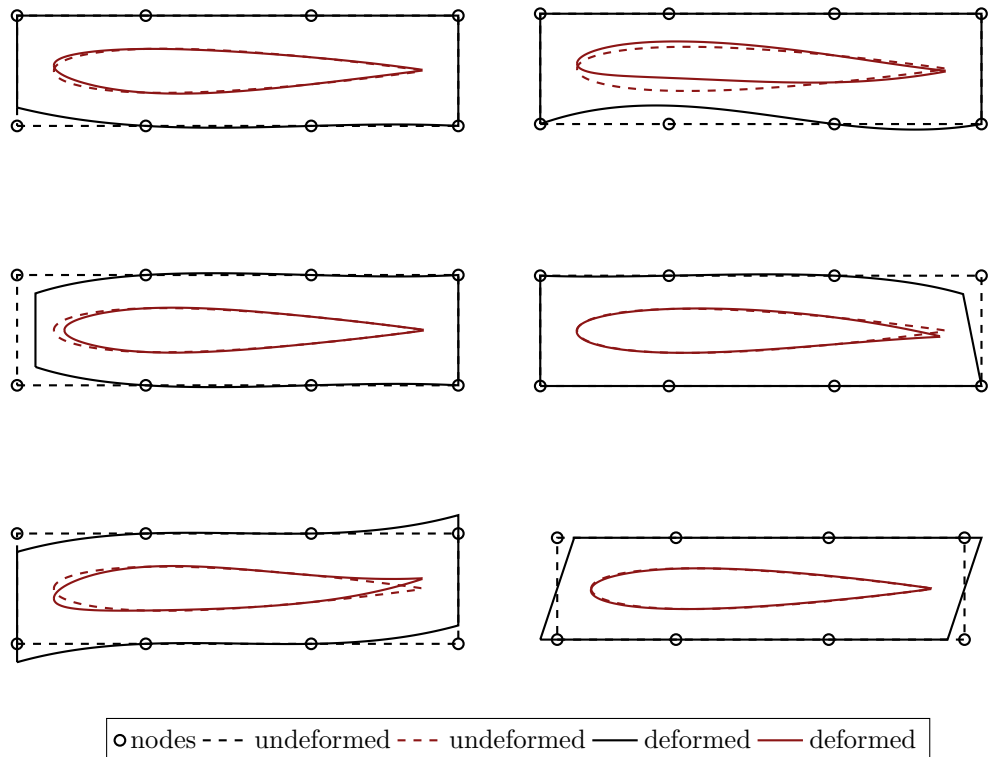


Figure 4.3: Visualization of the design element concept, exemplarily shown on a NACA0012 airfoil. For simplicity, a single design element(cubic in the horizontal direction and linear in the vertical direction) is used. Both the initial configuration(dashed lines) and the deformed configuration(full lines) are plotted. Although only eight design element nodes are provided, the function space of the design element allows for a great variation of the airfoil shape. Also, the size of the parameter space is now independent of the airfoil mesh size. From this perspective, the design element concept can be regarded as a model reduction for the shape variation. We will use exactly this parametrization of a NACA0012 airfoil here to verify the implemented shape-sensitivities in chapter 9

CHAPTER 4. OPTIMIZATION

Chapter 5

Fluid Sensitivity Analysis (SA)

Contents

5.1	General concepts	37
5.2	Sensitivity derivation	38
5.2.1	Calculation of $\frac{\partial q_j}{\partial s_i} \Big _{w_0}$	39
5.2.2	Calculation of $\frac{\partial q_j}{\partial w} \Big _{w_0}$	39
5.2.3	Calculation of $\frac{dw}{ds_i} \Big _{w_0}$	40
5.3	Full sensitivity equation	42

As explained in chapter 4, optimization is based on the calculations of gradients, also denoted as sensitivities. The derivation and implementation of these gradients constituted the lion-share of this thesis. We will therefore denote this chapter to the general derivation of fluid-sensitivity equations, before a detailed look into the most important terms within these equations is provided in chapter 6.

5.1 General concepts

When it comes to calculating the gradients of a solution of a PDE, there are two fundamentally different approaches one could take.

Firstly, one could think of first deriving the continuous equations and then applying the discretization scheme on them. On the other hand its equally legitimate to first apply the discretization and compute the gradients of this approximated solution. This thesis focuses on the latter for very particular reasons, see figure 5.1. If one would take the first approach, getting a steady state solution for the subsequent Sensitivity Analysis (SA) would entail the solution of the derived system of equations. This can not be done with standard CFD software. In addition to the SA routines, one would therefor have to implement an additional steady equation solver. This

is not only uneconomical, it increases the risk of creating implementation bugs and also defeats the purpose of decades of research in stable and efficient **NSE** solvers.

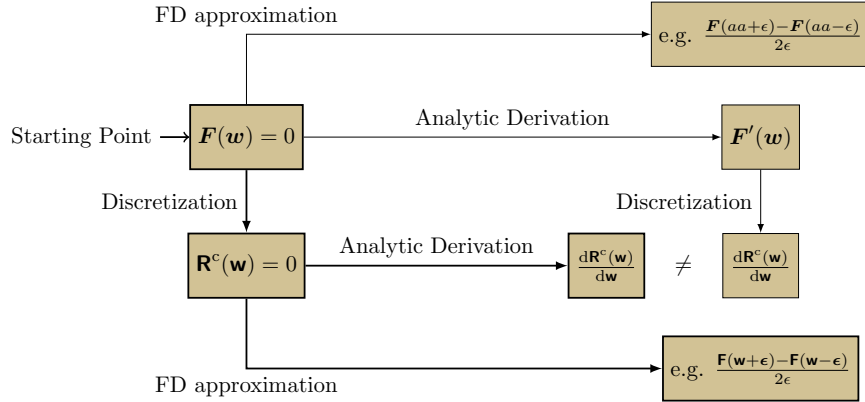


Figure 5.1: Two different approaches of SA. The question here is whether to discretize the system of equations first and then compute the derivatives of the approximate solution, or whether the continuous system of equation is first derived and discretized afterwards. Both approaches are valid, the final result however will generally not be the same. We have solemnly focused on the case of derivation after discretization in this thesis(thick lines). There are several reason to this. Firstly, if one chose to first derive and then compute a discretized solution, one would solve a completely different equation. If on the other hand the discretization(e.g. Finite Volumes) is done first, standard solvers can be utilized. What is more, approximating the derivative by a Finite difference becomes much easier, since the finite difference evaluation involves only a evaluation of \mathbf{F} , which a standard fluid solver is perfectly capable of, whereas the FD approximation in the other case would involve evaluations of the continuous function and the discretization of the obtained expression which would be much more cumbersome.

5.2 Sensitivity derivation

When it comes to **SA** within the context of **CFD**, one also has to distinguish between **SA** of the non-coupled fluid problem and the **SA** in the fully coupled aeroelastic case. The latter case is much more involved, since it requires additional terms from the Structure and mesh motion equations as well as for the coupling itself. In the following we will therefore begin with the **SA** of a regular fluid problem. A generalization to a coupled FSI problem will follow.

As mentioned in Section 4, we typically deal with an optimization criteria q_j , that is in this case dependent on the fluid state variables \mathbf{w} that themselves may depend on abstract variables s_i

$$q_j = q_j(\mathbf{w}(s_i)) \quad (5.1)$$

$$\frac{dq_j}{ds_i} \Big|_{\mathbf{w}_0} = \underbrace{\frac{\partial q_j}{\partial s_i} \Big|_{\mathbf{w}_0}}_{\text{directly derived from the definition of } q} + \underbrace{\frac{\partial q_j}{\partial \mathbf{w}} \Big|_{\mathbf{w}_0}}_{\text{derived analytically or by FD}} \underbrace{\frac{d\mathbf{w}}{ds_i} \Big|_{\mathbf{w}_0}}_{\text{derived from dynamic fluid equilibrium}} \quad (5.2)$$

5.2.1 Calculation of $\frac{\partial q_j}{\partial s_i} \Big|_{\mathbf{w}_0}$

For the optimization criterion, we restrict ourselves to Lift(L), Drag(D) and combinations of these quantities (e.g. Lift-Drag ration $\frac{L}{D}$). As abstract variables we only consider the free stream Mach-number M_∞ , the free-stream angle of attack α_∞ and an airfoil shape parameter as explained in chapter 4.2. The formula for the lift over an airfoil can be written as

If Γ_{FS} denotes the fluid structure interface, which in the ALE context coincides with the airfoil surface, one can formulate the lift and drag of an airfoil in a steady state as:

$$L = \int_{\Gamma_{FS}} p(\mathbf{w}, \mathbf{x}) \mathbf{n}(\mathbf{x}) \cdot \mathbf{e}_L dS$$

$$D = \int_{\Gamma_{FS}} p(\mathbf{w}, \mathbf{x}) \mathbf{n}(\mathbf{x}) \cdot \mathbf{e}_D dS \quad (5.3)$$

$$(5.4)$$

where \mathbf{e}_D is the unit vector pointing in the direction of the free stream, and \mathbf{e}_L is the unit vector perpendicular to that. We therefore note, that $\frac{\partial L}{\partial s_i}$ and $\frac{\partial D}{\partial s_i}$ are zero for $s_i = M_\infty$ and $s_i = \alpha_\infty$ and non-zero if s_i is a shape parameter.

Also, having determined the derivatives $\frac{\partial L}{\partial s_i}$ and $\frac{\partial D}{\partial s_i}$, the derivative of the Lift-Drag ratio follows simply as

$$-\frac{\partial(\frac{L}{D})}{\partial s_i} \Big|_{\mathbf{w}_0} = -\frac{D|_{\mathbf{w}_0} \frac{\partial L}{\partial s_i}|_{\mathbf{w}_0} - L|_{\mathbf{w}_0} \frac{\partial D}{\partial s_i}|_{\mathbf{w}_0}}{D|_{\mathbf{w}_0}|^2} \quad (5.5)$$

5.2.2 Calculation of $\frac{\partial q_j}{\partial \mathbf{w}} \Big|_{\mathbf{w}_0}$

The derivative of the optimization criteria with respect to the fluid state vector can again be splitted into Lift and Drag part. For an aeroelastic simulation, the biggest difficulty here is the dependence of the fluid state by the fluid-structure interface itself. We are therefore faced with a derivative of an integral quantity, where the integration area itself is dependent on the quantity of interest.

For this purpose, we recall the Leibniz rule from calculus:

$$\frac{d}{dx} \left(\int_{a(x)}^{b(x)} f(x, t) dt \right) = f(x, b(x)) \cdot \frac{d}{dx} b(x) - f(x, a(x)) \cdot \frac{d}{dx} a(x) + \int_{a(x)}^{b(x)} \frac{d}{dx} f(x, t) dt \quad (5.6)$$

Alternatively, we can directly switch to the discrete form, where the calculation of Lift and drag as outlined in Equation (5.3) can be performed as

$$L = \sum_{e \in \sum_{\Gamma_{FS}}} \sum_{i=1}^{n_g} g_i p(\mathbf{w}_i, \mathbf{x}_i) \mathbf{n}_e \cdot e_L D = \sum_{e \in \sum_{\Gamma_{FS}}} \sum_{i=1}^{n_g} g_i p(\mathbf{w}_i, \mathbf{x}_i) \mathbf{n}_e \cdot e_D \quad (5.7)$$

where $\sum_{\Gamma_{FS}}$ is the set of surface elements on the fluid-structure interface, n_g is the number of gauss-points and g_i are the gauss weights. The dependency of the surface shape, on the fluid state vector is now reflected in non-zero derivatives of the gauss point locations.

Finally, the derivative of the lift-to-drag ratio can be obtained analogously to equation (5.5) as

$$\frac{\partial(\frac{L}{D})}{\partial \mathbf{w}}|_{\mathbf{w}_0} = \frac{D|_{\mathbf{w}_0} \frac{\partial L}{\partial \mathbf{w}}|_{\mathbf{w}_0} - L|_{\mathbf{w}_0} \frac{\partial D}{\partial \mathbf{w}}|_{\mathbf{w}_0}}{D|_{\mathbf{w}_0}^2} \quad (5.8)$$

5.2.3 Calculation of $\frac{d\mathbf{w}}{ds_i}\Big|_{\mathbf{w}_0}$

Also, we keep in mind, that the state equation of the fluid can be expressed as

$$\mathcal{F}_{gov}(\mathbf{w}(s_i), \mathbf{x}(s_i), s_i) = \frac{\partial \mathbf{w}(s_i)}{\partial t} + \nabla \cdot \mathcal{F}(\mathbf{w}(s_i)) + \nabla \cdot \mathcal{G}(\mathbf{w}(s_i)) + S = \mathbf{0} \quad (5.9)$$

After discretization, we have derived our discrete governing equation as

$$\frac{\partial \bar{\mathbf{w}}_i}{\partial t} + \sum_{j \in \kappa(i)} \phi_{ij}(\mathbf{w}_{ij}, \mathbf{w}_{ji}, \boldsymbol{\nu}_{ij}) - \sum_{T_i \in \lambda(i)} \int_{T_j} \mathbb{K} \nabla \mathbf{w} \nabla \phi_j dx = \mathbf{0} \quad (5.10)$$

For the purpose of Sensitivity analysis around a given steady state, the fluid-state vector does not change in time, and can thus be omitted, also we summarize the convective and the diffusive part as \mathbf{R}

$$\cancel{\frac{\partial \bar{\mathbf{w}}_i}{\partial t}}^0 + \underbrace{\sum_{j \in \kappa(i)} \phi_{ij}(\mathbf{w}_{ij}, \mathbf{w}_{ji}, \boldsymbol{\nu}_{ij})}_{\mathbf{R}^i} - \underbrace{\sum_{T_i \in \lambda(i)} \int_{T_j} \mathbb{K} \nabla \mathbf{w} \nabla \phi_j dx}_{\mathbf{R}^v} = \mathbf{0} \quad (5.11)$$

where \mathbf{R}^i denotes the inviscid residual and \mathbf{R}^v the viscous contribution. We now can express the steady state equation in very compact form as:

$$\mathbf{R} = \mathbf{0} \quad (5.12)$$

In general, this residual depends on the fluid state solution \mathbf{w} as well as on a potential mesh movement \mathbf{x} , both of which can be dependent on the abstract design variable. Additionally, a direct dependence on s might be encountered too.

$$\mathbf{R}(\mathbf{w}(s), \mathbf{x}(s), s) = \mathbf{0} \quad (5.13)$$

5.2. SENSITIVITY DERIVATION

The total derivative of the residual with respect to the design variable can thus be expanded via the chain rule to

$$\frac{d\mathbf{R}}{ds_i} = \mathbf{0} = \frac{\partial \mathbf{R}}{\partial s_i} + \frac{\partial \mathbf{R}}{\partial \mathbf{w}} \frac{d\mathbf{w}}{ds_i} + \frac{\partial \mathbf{R}}{\partial \mathbf{x}} \frac{d\mathbf{x}}{ds_i} \quad (5.14)$$

Therefore the total derivative of the fluid state with respect to the shape variable, needed in equation (5.2), can be obtained by solving

$$\frac{\partial \mathbf{R}}{\partial \mathbf{w}} \underline{\frac{d\mathbf{w}}{ds_i}} = -\frac{d\mathbf{R}}{ds_i} - \frac{\partial \mathbf{R}}{\partial \mathbf{x}} \frac{d\mathbf{x}}{ds_i} \quad (5.15)$$

In this equation, $\frac{\partial \mathbf{R}}{\partial s_i}$ can be computed analytically or by FD. This part is the most cumbersome part of the whole sensitivity analysis, which is why we denoted a full chapter(6) to it.

The derivative of the mesh motion with respect to the abstract variables is often denoted as "shape gradient". It can be divided into two components:

- The interface component $\frac{d\dot{\mathbf{x}}_\Gamma}{ds_i}$, which is associated with the grid points lying on the fluid boundary
- The interior component $\frac{d\dot{\mathbf{x}}_\Omega}{ds_i}$, which is associated with the grid points located in the interior Ω of the computational domain.

The interface component is determined by the structure. Having obtained this one, the interior component can be computed by solving an auxiliary, fictitious Dirichlet problem:

$$\frac{d\dot{\mathbf{x}}_\Omega}{ds_i} = - \left[\bar{\mathbf{K}}_{\Omega\Omega}^{-1} \bar{\mathbf{K}}_{\Omega\Gamma} \right] \frac{d\mathbf{x}_\Gamma}{ds_i} \quad (5.16)$$

where $\bar{\mathbf{K}}$ is a pseudo stiffness matrix that can be obtained by a simple spring analogy or similar approaches. In general, the mesh-motion algorithm should be chosen consistently with the one used in the calculation of the steady state solution. For the later introduced Embedded framework, $\frac{d\dot{\mathbf{x}}_\Gamma}{ds_i}$ is the sensitivity of the embedded discrete surface.

5.3 Full sensitivity equation

After inserting (5.5), (5.8) and (5.15) into (5.2), one can derive the final sensitivity equations for the special case of a rigid or non-existing structure as

$$\frac{dq_j}{ds_i} \Big|_{\mathbf{w}_0} = -\frac{dq_j}{d\mathbf{w}} \Big|_{\mathbf{w}_0} \left[\frac{\partial \mathbf{R}}{\partial \mathbf{w}} \Big|_{w_0} \right]^{-1} \left(\frac{\partial \mathbf{R}}{\partial s_i} \Big|_{w_0} + \left[\alpha \frac{\partial \mathbf{R}}{\partial \dot{\mathbf{x}}_\Omega} \Big|_{\mathbf{w}_0} \quad \frac{\partial \mathbf{R}}{\partial \dot{\mathbf{x}}_\Gamma} \Big|_{\mathbf{w}_0} \right] \begin{bmatrix} \alpha \bar{\mathbf{K}}_{\Omega\Omega}^{-1} \bar{\mathbf{K}}_{\Omega\Gamma} \\ \mathbf{I} \end{bmatrix} \frac{d\dot{\mathbf{x}}_\Gamma}{ds_i} \right)$$

$$\alpha = \begin{cases} 1 & \text{in ALE framework} \\ 0 & \text{in Embedded framework} \end{cases} \quad (5.17)$$

Chapter 6

Derivatives of the fluid residual

Contents

6.1	Fluid Jacobian $\frac{\partial \mathbf{R}}{\partial \mathbf{w}}$	43
6.1.1	Derivative of the convective Jacobian $\frac{\partial \mathbf{R}^c}{\partial \mathbf{w}}$	44
6.1.2	Derivative of the viscous Jacobian $\frac{\partial \mathbf{R}^v}{\partial \mathbf{w}}$	45
6.2	Analytic Jacobian of the Roe flux $\frac{\partial \phi}{\partial \mathbf{w}}$	46
6.3	Derivative with respect to the abstract variable $\frac{\partial \mathbf{R}}{\partial s}$	53
6.3.1	Convective contribution to $\frac{\partial \mathbf{R}}{\partial s}$	54
6.3.2	Viscous contribution to $\frac{\partial \mathbf{R}}{\partial s}$	55

This chapter is devoted to a thorough derivation of the partial derivatives $\frac{\partial \mathbf{R}}{\partial \mathbf{w}}$ and $\frac{\partial \mathbf{R}}{\partial s}$ of the fluid residual equation. These are the main quantities needed in order to compute the sensitivity of the state vector $\frac{d\mathbf{w}}{ds}$ as shown in equation (5.17). We need this derivative in order to solve for $\frac{dq_j}{ds_i}$.

6.1 Fluid Jacobian $\frac{\partial \mathbf{R}}{\partial \mathbf{w}}$

As described in equation (5.11), the total residual is comprised of a convective(inviscid) part and a diffusive(viscous) contribution. Thanks to the distributive property of the derivative operator, we can thus compute the derivative of the total residual as the sum of the derivatives of the components. This is particularly important for us, since we used two different discretization routines for the viscous and the inviscid part(see chapter 2.3).

6.1.1 Derivative of the convective Jacobian $\frac{\partial \mathbf{R}^c}{\partial \mathbf{w}}$

Also, we will only discuss the special case of intersected elements in the following, since the case of an non-intersected cell follows trivially from that.

For more details on the evaluation of the inviscid residual the reader is referred to chapter 2, specifically chapter 2.3 and chapter 8 for the incorporation of the immersed boundary conditions.

For the convective part of the Jacobian \mathbf{R}^c we can be therefor write

$$\mathbf{R}_{ij}^{c,i} = \phi_{ij}^i(\tilde{\mathbf{w}}_{ij}, \tilde{\mathbf{w}}_{ij}^*, \mathbf{n}_{ij}) \quad (6.1)$$

Since the fluid normal is dependent on the mesh position this can also be written as

$$\mathbf{R}_{ij}^{c,i} = \phi_{ij}^i(\tilde{\mathbf{w}}_{ij}, \tilde{\mathbf{w}}_{ij}^*, \mathbf{x}) \quad (6.2)$$

If the edge $i - j$ is intersected however, the half-Riemann problem approach as discussed in chapters 8.2 and 8.3 is applied. Also, the quantity \mathbf{w}_{ij} on the interface can be reconstructed in several ways. In this thesis we applied a MUSCL technique. Of course, the reconstruction and limitation has to be taken into account as well.

Putting all this together, one can write

$$\frac{\partial \mathbf{R}_{ij}^{c,i}}{\partial \mathbf{w}_k} = \frac{\partial \mathbf{R}_{ij}^{c,i}}{\partial \tilde{\mathbf{w}}_{ij}^*} \frac{\partial \tilde{\mathbf{w}}_{ij}^*}{\partial \mathbf{w}_k} \frac{\partial \tilde{\mathbf{w}}_k}{\partial \mathbf{w}_k} + \frac{\partial \mathbf{R}_{ij}^{c,i}}{\partial \tilde{\mathbf{w}}_{ij}} \frac{\partial \tilde{\mathbf{w}}_{ij}}{\partial \mathbf{w}_k} \frac{\partial \tilde{\mathbf{w}}_k}{\partial \mathbf{w}_k} + \underbrace{\frac{\partial \mathbf{R}_{ij}^{c,i}}{\partial \mathbf{x}} \frac{\partial \mathbf{x}}{\partial \mathbf{n}_{ij}}}_{=0 \text{ for embedded}} \quad (6.3)$$

- Analytical Jacobian of the (Roe's) centering flux
- Analytical derivative of the solution of the 1D half-Riemann problem
- Analytical derivative of the MUSCL reconstruction and limitation

where, $(\tilde{\sim})$ denotes primitive quantitative, $\frac{\partial \tilde{\mathbf{w}}_k}{\partial \mathbf{w}_k}$ accounts for the conversion between primitive and conservative state vector, $\frac{\partial \mathbf{R}_{ij}^{c,i}}{\partial \tilde{\mathbf{w}}_{ij}^*}$ is the analytical derivative of the MUSCL reconstruction and limitation and a is the analytical Jacobian of the Roe flux. Finally, $\frac{\partial \tilde{\mathbf{w}}_{ij}^*}{\partial \mathbf{w}_k}$ accounts for the analytical derivative of the solution of the 1D half-Riemann problem. This also accounts for the only really new derivative to be considered in comparison to the cells far from the immersed boundaries.

The analytic Jacobian of the Roe flux is provided in chapter 6.2, the derivative of the solution of the 1D half-Riemann problem is discussed in chapter 8.2.1, the derivative of the MUSCL reconstruction in section 2.4.1 and finally, the derivative of the conversion to primitive variables is discussed in section 1.2.4.

6.1.2 Derivative of the viscous Jacobian $\frac{\partial \mathbf{R}^c}{\partial \mathbf{w}}$

For the discussion of the viscous Jacobian, we first remind the reader that an **FE** approach is used to evaluate this term, in contrast to the **FV** approach used for the inviscid contribution. For a detailed discussion the reader is referred to chapter 2.3 and the following chapters.

As far as the residual evaluation itself goes, we recall that, once the ghost points have been populated(see chapter 8.3.1), the viscous residual is evaluated as though the cell had never been intersected in the first place. We can therefore write the viscous residual of an intersected cell as

$$\mathbf{R}^c(\tilde{\mathbf{w}}^a, \tilde{\mathbf{w}}^g(\tilde{\mathbf{w}}^a)) = \mathbf{0} \quad (6.4)$$

where $\tilde{\mathbf{w}}^a$ represents the fluid states of the active node, and $\tilde{\mathbf{w}}^g$ are the fluid states of the ghost nodes, which can themselves be expressed in terms of the active nodes. Thus the derivative becomes:

$$\frac{\partial \mathbf{R}^v(\tilde{\mathbf{w}}^a, \tilde{\mathbf{w}}^g(\tilde{\mathbf{w}}^a))}{\partial \tilde{\mathbf{w}}} = \underbrace{\frac{\partial \mathbf{R}^v}{\partial \tilde{\mathbf{w}}^a}}_{\substack{\text{can be re-used from ALE} \\ \text{after the ghost-point population}}} + \frac{\partial \mathbf{R}^v}{\partial \tilde{\mathbf{w}}^g} \cdot \widehat{\frac{\partial \tilde{\mathbf{w}}^g}{\partial \tilde{\mathbf{w}}^a}} \quad (6.5)$$

obtained during the population process

For the analytic viscous Jacobian contribution we don't have to make a difference between $\frac{\partial \mathbf{R}^c}{\partial \tilde{\mathbf{w}}^a}$ and $\frac{\partial \mathbf{R}^v}{\partial \tilde{\mathbf{w}}^a}$.

We recall the definition of the viscous residual as

$$\mathbf{R}_i^v = - \sum_{T_i \in \lambda(i)} \int_{T_j} \mathbb{K} \nabla \mathbf{w} \nabla \phi_j dx \quad (6.6)$$

again, we switch to primitive variables for easier evaluation

$$\mathbf{R}_i^v = - \sum_{T_i \in \lambda(i)} \int_{T_j} \tilde{\mathbb{K}} \nabla \tilde{\mathbf{w}} \nabla \phi_j dx \quad (6.7)$$

Applying a numerical integration such as gauss rule, this becomes

$$\mathbf{R}_i^v = - \sum_{T_i \in \lambda(i)} \sum_{i=1}^{n_g} w_i \tilde{\mathbb{K}} \nabla \tilde{\mathbf{w}}(\mathbf{x}_i) \nabla \phi_j(\mathbf{x}_i) dx \quad (6.8)$$

Thus, due the constant nature of the diffusive tensor \mathbb{K} the derivative can be written straightforwardly as

$$\frac{\partial \mathbf{R}_i^v}{\partial \tilde{\mathbf{w}}} = - \sum_{T_i \in \lambda(i)} \sum_{i=1}^{n_g} w_i \tilde{\mathbb{K}} \nabla \tilde{\mathbf{w}}(\mathbf{x}_i) \nabla \phi_j(\mathbf{x}_i) dx \quad (6.9)$$

6.2 Analytic Jacobian of the Roe flux $\frac{\partial \phi}{\partial \mathbf{w}}$

This chapter provides a detailed step by step derivation of the analytic convective Jacobian. This chapter is lengthy and not necessarily required for understanding the rest of the thesis. For this reason it has been moved at the end of this chapter. Nonetheless, in the authors opinion, it provides some crucial insight into the basics of **SA**, and it is certainly of great help and serves as a reference for anyone who wants to implement those derivatives himself.

We start by expanding the derivative to

$$\frac{\partial \mathbf{R}_i^c}{\partial \mathbf{w}} = \sum_{j \in \kappa(i)} \underbrace{\frac{\partial \text{meas}((C_{ij}))}{\partial \mathbf{w}} \phi_{ij}(\mathbf{w}_{ij}, \mathbf{w}_{ji}, \boldsymbol{\nu}_{ij})}_{=0 \text{ for embedded}} + \text{meas}(C_{ij}) \frac{\partial \phi_{ij}(\mathbf{w}_{ij}, \mathbf{w}_{ji}, \boldsymbol{\nu}_{ij})}{\partial \mathbf{w}} \quad (6.10)$$

where the first term is always zero for embedded simulations.

Next, we recall the definition of the numerical flux as

$$\phi(\mathbf{w}_i, \mathbf{w}_j, \mathbf{n}_{ij}) = \frac{1}{2} [\mathcal{F}(\mathbf{w}_i) \cdot \mathbf{n}_{ij} + \mathcal{F}(\mathbf{w}_j) \cdot \mathbf{n}_{ij}] - \frac{1}{2} |\mathbf{A}_{\text{Roe}}(\mathbf{w}_i, \mathbf{w}_j, \mathbf{n}_{ij})| (\mathbf{w}_j - \mathbf{w}_i) \quad (6.11)$$

Similar to the **MUSCL** procedure we transform the fluid state vector to primitive form

$$\mathbf{w} = \begin{pmatrix} \rho \\ \rho \mathbf{v} \\ E \end{pmatrix} \xrightarrow{\text{U}} \tilde{\mathbf{w}} = \begin{pmatrix} \rho \\ \mathbf{v} \\ p \end{pmatrix} \quad (6.12)$$

Of course, this transformation involves the **EOS** of the fluid. We will use $(\tilde{\cdot})$ from now on to mark any quantity as based on/formulated in primitive variables. The primitive state vector is also much more appealing when it comes to the implementation of boundary conditions, since the solution variables are separated there. Next we recall the conservative form of the Euler equations, which was presented in chapter 1.2.4 as

$$\frac{\partial \mathbf{w}}{\partial t} + \nabla \cdot \mathcal{F}(\mathbf{w}) = \mathbf{0} \quad (6.13)$$

Where the convective flux matrix \mathcal{F} is provided in equation (1.15), and can be written as

$$\mathcal{F}(\mathbf{w}) = \begin{pmatrix} \mathcal{F}_x(\mathbf{w}) & \mathcal{F}_x(\mathbf{w}) & \mathcal{F}_x(\mathbf{w}) \end{pmatrix} \quad (6.14)$$

Therefore, applying the Nabla operator in equation (6.13) gives

$$\frac{\partial \mathbf{w}}{\partial t} + \underbrace{\frac{\partial \mathcal{F}_x(\mathbf{w})}{\partial \mathbf{w}}}_{\mathbf{A}} \frac{\partial \mathbf{w}}{\partial x} + \underbrace{\frac{\partial \mathcal{F}_y(\mathbf{w})}{\partial \mathbf{w}}}_{\mathbf{B}} \frac{\partial \mathbf{w}}{\partial y} + \underbrace{\frac{\partial \mathcal{F}_z(\mathbf{w})}{\partial \mathbf{w}}}_{\mathbf{C}} \frac{\partial \mathbf{w}}{\partial z} = \mathbf{0} \quad (6.15)$$

where the matrices \mathbf{A}, \mathbf{B} and \mathbf{C} are called the *flux Jacobians*.

In Section 5, we have derived that for any sensitivity calculation, the derivative of the flux matrix with respect to the fluid state vector $\frac{\partial \mathbf{R}^c}{\partial \mathbf{w}}$ is required.

We have derived in Section 2.3 that at an interior vertex point of the fluid mesh, we have

$$[\mathbf{R}^c(\mathbf{w}, \mathbf{x}, \dot{\mathbf{x}})]_i = \sum_{j \in \kappa(i)} \text{meas}(\partial C_{ij}) \boldsymbol{\phi}(\mathbf{w}_i, \mathbf{w}_j, \mathbf{n}_{ij}) \quad (6.16)$$

Since an equilibrium point is considered, $\dot{\mathbf{x}} = \mathbf{0}$ and is neglected in the following derivations.

In equation (2.9) we have introduced $\boldsymbol{\phi}$ as the numerical flux function. In this thesis, we consider the popular Roe flux, which is defined as given in equation (6.11).

Let us remind, that \mathbf{R}_i^c is the convective residual at vertex i , $\kappa(i)$ is the set of vertices connected to vertex i by an edge, C_i is the control volume of the dual cell centered at vertex i and ∂C_{ij} is the segment of the boundary that intersects edge $(i - j)$ and \mathbf{n}_{ij} is the outward-facing weighted normal to ∂C_{ij} . See figure 2.1 for a visualization of the setup.

From Equation (6.16) it is obvious that, when looking for the derivative $\frac{\partial \mathbf{R}^c}{\partial \mathbf{w}}$, the derivative of the numerical flux with respect to the fluid state vector $\frac{\partial \boldsymbol{\phi}}{\partial \mathbf{w}}$ is required. To make things easier we will in the following derive the primitive version of that quantity: $\frac{\partial \tilde{\boldsymbol{\phi}}}{\partial \mathbf{w}}$

As [13] demonstrates, primitive version of the numerical Roe flux can be expressed as

$$\tilde{\boldsymbol{\phi}}(\tilde{\mathbf{w}}_i, \tilde{\mathbf{w}}_j, \mathbf{n}_{ij}) = \frac{1}{2} \left(\tilde{\mathcal{F}}(\tilde{\mathbf{w}}_i) \cdot \mathbf{n}_{ij} + \tilde{\mathcal{F}}(\tilde{\mathbf{w}}_j) \cdot \mathbf{n}_{ij} \right) - \frac{1}{2} \mathbf{P}^{-1}(\sim) |\boldsymbol{\Lambda}(\sim)| \mathbf{P}(\sim) (\tilde{\mathbf{w}}_j - \tilde{\mathbf{w}}_i) \quad (6.17)$$

where, for ease of notation we omit the function arguments by simply writing (\sim) as follows

$$\begin{aligned} \mathbf{P}^{-1}(\sim) &= \mathbf{P}^{-1}(\mathbf{M}(\sim), \mathbf{n}_{ij}) \\ \mathbf{M}(\sim) &= \mathbf{M}(\tilde{\mathbf{w}}_i, \tilde{\mathbf{w}}_j) \\ \boldsymbol{\Lambda}(\sim) &= \boldsymbol{\Lambda}(\mathbf{M}(\sim), \mathbf{n}_{ij}) \\ \mathbf{P}(\sim) &= \mathbf{P}(\mathbf{M}(\sim), \mathbf{n}_{ij}) \end{aligned} \quad (6.18)$$

Here, $\mathbf{M}(\tilde{\mathbf{w}}_i, \tilde{\mathbf{w}}_j)$ is the averaging function associated with the roe flux. It can be written as

$$\mathbf{M}(\tilde{\mathbf{w}}_i, \tilde{\mathbf{w}}_j) = \frac{1}{\sqrt{\rho_i} + \sqrt{\rho_j}} \begin{pmatrix} \rho_i \\ \mathbf{v}_i \\ \mathbf{H}_i \end{pmatrix} + \frac{1}{\sqrt{\rho_j} + \sqrt{\rho_i}} \begin{pmatrix} \rho_j \\ \mathbf{v}_j \\ \mathbf{H}_j \end{pmatrix} \quad (6.19)$$

and \mathbf{P} is the matrix whose columns are the right eigenvectors of the Jacobian matrix \mathcal{A} of \mathcal{F} . The Jacobi matrix in primitive form can be written as

$$\begin{aligned} \tilde{\mathcal{A}} &= \frac{\partial(\tilde{\mathcal{F}} \cdot \mathbf{n})}{\partial \tilde{\mathbf{w}}} \\ &= \begin{bmatrix} \mathbf{v} \cdot \mathbf{n} & \rho n_x & \rho n_y & \rho n_z & 0 \\ v_1(\mathbf{v} \cdot \mathbf{n}) & \rho(v \cdot \mathbf{n}) + \rho v_1 n_1 & \rho v_1 n_2 & \rho v_1 n_3 & n_1 \\ v_2(\mathbf{v} \cdot \mathbf{n}) & \rho v_2 n_1 & \rho(v \cdot \mathbf{n}) + \rho v_2 n_2 & \rho v_2 n_3 & n_2 \\ v_3(\mathbf{v} \cdot \mathbf{n}) & \rho v_3 n_1 & \rho v_3 n_2 & \rho(v \cdot \mathbf{n}) + \rho v_3 n_3 & n_2 \\ A_{51} & A_{52} & A_{53} & A_{54} & A_{55} \end{bmatrix} \\ \mathcal{A}_{51} &= H(\mathbf{v} \cdot \mathbf{n}) - \rho \mathbf{v} \cdot \mathbf{n} \frac{\gamma p}{\rho(\gamma)} \\ \mathcal{A}_{52} &= \rho \mathbf{v} \cdot \mathbf{n} v_1 + \rho H n_1 \\ \mathcal{A}_{53} &= \rho \mathbf{v} \cdot \mathbf{n} v_2 + \rho H n_2 \\ \mathcal{A}_{54} &= \rho \mathbf{v} \cdot \mathbf{n} v_3 + \rho H n_3 \\ \mathcal{A}_{55} &= \rho \mathbf{v} \cdot \mathbf{n} \frac{\gamma}{\rho(\gamma - 1)} \end{aligned} \quad (6.20)$$

For this Jacobian, one can now symbolically derive an eigenvalue decomposition, such that

$$\mathcal{A} = \mathbf{P}^{-1} \Lambda \mathbf{P} \quad (6.21)$$

The total specific enthalpy for a perfect gas is given as

$$\mathbf{H} = \frac{\gamma p}{\rho(\gamma - 1)} + \frac{1}{2} \mathbf{v}^T \mathbf{v} \quad (6.22)$$

where we note the following derivatives

$$\frac{\partial \mathbf{H}}{\partial \rho} = -\frac{\gamma p}{\rho^2(\gamma-1)} \quad \frac{\partial \mathbf{H}}{\partial v_i} = v_i \quad \frac{\partial \mathbf{H}}{\partial p} = \frac{\gamma}{\rho(\gamma-1)} \quad (6.23)$$

Therefore, the derivative of the averaging function with respect to the primitive fluid state vector can be calculated as

$$\begin{aligned} \frac{\partial \mathbf{M}(\sim)}{\partial \rho_i} &= \frac{1}{2\sqrt{\rho_i}(\sqrt{\rho_i} + \sqrt{\rho_j})} \left(-\mathbf{M}(\sim) + \begin{bmatrix} 3\rho_i & 2\sqrt{\rho_i}\mathbf{v}_i & 2\mathbf{H}_i - 2\rho_i \frac{\gamma p}{\rho^2(\gamma-1)} \end{bmatrix}^T \right) \\ \frac{\partial \mathbf{M}(\sim)}{\partial v_i} &= \frac{1}{(\sqrt{\rho_i} + \sqrt{\rho_j})} \sqrt{\rho_i} \begin{bmatrix} 0 & \mathbf{e}_i^T & v_i \end{bmatrix}^T \\ \frac{\partial \mathbf{M}(\sim)}{\partial p_i} &= \frac{1}{(\sqrt{\rho_i} + \sqrt{\rho_j})} \sqrt{\rho_i} \begin{bmatrix} 0 & \mathbf{0}^T & \frac{\gamma}{\rho(\gamma-1)} \end{bmatrix}^T \\ \frac{\partial \mathbf{M}(\sim)}{\partial \tilde{\mathbf{w}}_i} &= \begin{bmatrix} 3\rho_i - \frac{\sqrt{\rho_i}\rho_i + \sqrt{\rho_j}\rho_j}{\sqrt{\rho_i} + \sqrt{\rho_j}} & 0 & 0 & 0 & 0 \\ v_{1i} - \frac{\sqrt{\rho_i}v_{1i} + \sqrt{\rho_j}v_{1j}}{\sqrt{\rho_i} + \sqrt{\rho_j}} & 2\rho_i & 0 & 0 & 0 \\ v_{2i} - \frac{\sqrt{\rho_i}v_{2i} + \sqrt{\rho_j}v_{2j}}{\sqrt{\rho_i} + \sqrt{\rho_j}} & 0 & 2\rho_i & 0 & 0 \\ v_{3i} - \frac{\sqrt{\rho_i}v_{3i} + \sqrt{\rho_j}v_{3j}}{\sqrt{\rho_i} + \sqrt{\rho_j}} & 0 & 0 & 2\rho_i & 0 \\ \frac{\mathbf{v}^T \mathbf{v}}{2} - \frac{\gamma p}{\rho(\gamma-1)} - \frac{\sqrt{\rho_i}\mathbf{H}_i + \sqrt{\rho_j}\mathbf{H}_j}{\sqrt{\rho_i} + \sqrt{\rho_j}} & 2\rho_i v_{1i} & 2\rho_i v_{1i} & 2\rho_i v_{1i} & \frac{2\gamma}{\gamma-1} \end{bmatrix} \end{aligned} \quad (6.24)$$

The matrix \mathbf{P} can be written as

$$\mathbf{P} = \begin{bmatrix} \left(\mathbf{n} - \frac{(\gamma-1)\mathbf{v}^T \mathbf{v}}{2c^2} \mathbf{n} + \mathbf{n} \times \mathbf{v} \right) \cdot \mathbf{e}_1 & n_1(\gamma-1) \frac{v_1}{c^2} & n_1(\gamma-1) \frac{v_2}{c^2} + n_3 & n_1(\gamma-1) \frac{v_3}{c^2} - n_2 & -n_1 \frac{\gamma-1}{c^2} \\ \left(\mathbf{n} - \frac{(\gamma-1)\mathbf{v}^T \mathbf{v}}{2c^2} \mathbf{n} + \mathbf{n} \times \mathbf{v} \right) \cdot \mathbf{e}_2 & n_2(\gamma-1) \frac{v_1}{c^2} - n_3 & n_2(\gamma-1) \frac{v_2}{c^2} & n_2(\gamma-1) \frac{v_3}{c^2} + n_1 & -n_2 \frac{\gamma-1}{c^2} \\ \left(\mathbf{n} - \frac{(\gamma-1)\mathbf{v}^T \mathbf{v}}{2c^2} \mathbf{n} + \mathbf{n} \times \mathbf{v} \right) \cdot \mathbf{e}_3 & n_3(\gamma-1) \frac{v_1}{c^2} + n_2 & n_3(\gamma-1) \frac{v_2}{c^2} - n_1 & n_3(\gamma-1) \frac{v_3}{c^2} & -n_2 \frac{\gamma-1}{c^2} \\ (\gamma-1) \frac{\mathbf{v}^T \mathbf{v}}{c^2} - c \mathbf{v} \cdot \mathbf{n} & -(\gamma-1)v_1 + cn_1 & -(\gamma-1)v_2 + cn_2 & -(\gamma-1)v_3 + cn_3 & \gamma-1 \\ (\gamma-1) \frac{\mathbf{v}^T \mathbf{v}}{c^2} - c \mathbf{v} \cdot \mathbf{n} & -(\gamma-1)v_1 - cn_1 & -(\gamma-1)v_2 - cn_2 & -(\gamma-1)v_3 - cn_3 & \gamma-1 \end{bmatrix} \quad (6.25)$$

where c is the speed of sound given by $c = \sqrt{\frac{\gamma p}{\rho}}$

The matrix Λ derives to

$$\Lambda = \text{diag}([\mathbf{v} \cdot \mathbf{n}, \mathbf{v} \cdot \mathbf{n}, \mathbf{v} \cdot \mathbf{n}, \mathbf{v} \cdot \mathbf{n} + c, \mathbf{v} \cdot \mathbf{n} - c]) \quad (6.26)$$

$$\frac{\partial \mathbf{P}^{-1}}{\partial \tilde{\mathbf{w}}}(\tilde{\mathbf{w}}, \mathbf{n}) \cdot b = \begin{bmatrix} \frac{\partial r_1}{\partial \tilde{\mathbf{w}}}(\tilde{\mathbf{w}}, \mathbf{n}) \cdot b & \cdots & \frac{\partial r_5}{\partial \tilde{\mathbf{w}}}(\tilde{\mathbf{w}}, \mathbf{n}) \cdot b \end{bmatrix} \quad (6.27)$$

$$\frac{\partial r_1}{\partial \tilde{\mathbf{w}}}(\tilde{\mathbf{w}}, \mathbf{n}) = \begin{bmatrix} 0 & 0 & 0 & 0 & 0 \\ 0 & \mathbf{n}_x & 0 & 0 & 0 \\ 0 & 0 & \mathbf{n}_x & 0 & 0 \\ 0 & 0 & 0 & \mathbf{n}_x & 0 \\ 0 & v_1 n_1 & v_2 n_1 + n_3 & v_3 n_1 - n_2 & 0 \end{bmatrix} \quad (6.28)$$

$$\frac{\partial r_2}{\partial \tilde{\mathbf{w}}}(\tilde{\mathbf{w}}, \mathbf{n}) = \begin{bmatrix} 0 & 0 & 0 & 0 & 0 \\ 0 & \mathbf{n}_y & 0 & 0 & 0 \\ 0 & 0 & \mathbf{n}_y & 0 & 0 \\ 0 & 0 & 0 & \mathbf{n}_y & 0 \\ 0 & v_1 n_2 - n_3 & v_2 n_2 & v_3 n_2 - n_1 & 0 \end{bmatrix} \quad (6.29)$$

$$\frac{\partial r_3}{\partial \tilde{\mathbf{w}}}(\tilde{\mathbf{w}}, \mathbf{n}) = \begin{bmatrix} 0 & 0 & 0 & 0 & 0 \\ 0 & \mathbf{n}_z & 0 & 0 & 0 \\ 0 & 0 & \mathbf{n}_z & 0 & 0 \\ 0 & 0 & 0 & \mathbf{n}_z & 0 \\ 0 & v_1 n_3 + n_2 & v_2 n_3 - n_1 & v_3 n_3 & 0 \end{bmatrix} \quad (6.30)$$

$$\frac{\partial r_4}{\partial \tilde{\mathbf{w}}}(\tilde{\mathbf{w}}, \mathbf{n}) = \begin{bmatrix} \frac{1}{2\gamma p} & 0 & 0 & 0 & -\frac{\rho}{2\gamma p^2} \\ \frac{v_1}{2\rho c^2} + \frac{n_1}{4\rho c} & \frac{1}{2c^2} & 0 & 0 & -\frac{v_1}{2pc^2} - \frac{n_1}{4pc} \\ \frac{v_2}{2\rho c^2} + \frac{n_2}{4\rho c} & 0 & \frac{1}{2c^2} & 0 & -\frac{v_2}{2pc^2} - \frac{n_2}{4pc} \\ \frac{v_3}{2\rho c^2} + \frac{n_3}{4\rho c} & 0 & 0 & \frac{1}{2c^2} & -\frac{v_3}{2pc^2} - \frac{n_3}{4pc} \\ \frac{1}{2\gamma} + \frac{\mathbf{v} \cdot \mathbf{n}}{4\rho c} & \frac{n_1}{2c} & \frac{n_2}{2c} & \frac{n_3}{2c} & -\frac{\mathbf{v} \cdot \mathbf{n}}{4pc} \end{bmatrix} \quad (6.31)$$

$$\frac{\partial r_5}{\partial \tilde{\mathbf{w}}}(\tilde{\mathbf{w}}, \mathbf{n}) = \begin{bmatrix} \frac{1}{2\gamma p} & 0 & 0 & 0 & -\frac{\rho}{2\gamma p^2} \\ \frac{v_1}{2\rho c^2} - \frac{n_1}{4\rho c} & \frac{1}{2c^2} & 0 & 0 & -\frac{v_1}{2pc^2} + \frac{n_1}{4pc} \\ \frac{v_2}{2\rho c^2} - \frac{n_2}{4\rho c} & 0 & \frac{1}{2c^2} & 0 & -\frac{v_2}{2pc^2} + \frac{n_2}{4pc} \\ \frac{v_3}{2\rho c^2} - \frac{n_3}{4\rho c} & 0 & 0 & \frac{1}{2c^2} & -\frac{v_3}{2pc^2} + \frac{n_3}{4pc} \\ \frac{1}{2\gamma} - \frac{\mathbf{v} \cdot \mathbf{n}}{4\rho c} & -\frac{n_1}{2c} & -\frac{n_2}{2c} & -\frac{n_3}{2c} & \frac{\mathbf{v} \cdot \mathbf{n}}{4pc} \end{bmatrix} \quad (6.32)$$

Due to its shape, the derivation of $\mathbf{\Lambda}$ can be simplified to a differentiation of the eigenvalues λ_i .

$$\begin{aligned} \frac{\partial \lambda_1}{\partial \tilde{\mathbf{w}}}(\tilde{\mathbf{w}}, \mathbf{n}) &= \frac{\partial \lambda_2}{\partial \tilde{\mathbf{w}}}(\tilde{\mathbf{w}}, \mathbf{n}) = \frac{\partial \lambda_3}{\partial \tilde{\mathbf{w}}}(\tilde{\mathbf{w}}, \mathbf{n}) = \begin{bmatrix} 0 & \mathbf{n}^T & 0 \end{bmatrix}^T \\ \frac{\partial \lambda_4}{\partial \tilde{\mathbf{w}}}(\tilde{\mathbf{w}}, \mathbf{n}) &= \begin{bmatrix} -\frac{c}{2\rho} & \mathbf{n}^T & \frac{c}{2p} \end{bmatrix}^T \\ \frac{\partial \lambda_5}{\partial \tilde{\mathbf{w}}}(\tilde{\mathbf{w}}, \mathbf{n}) &= \begin{bmatrix} \frac{c}{2\rho} & \mathbf{n}^T & -\frac{c}{2p} \end{bmatrix}^T \end{aligned} \quad (6.33)$$

$$\frac{\partial \mathbf{P}}{\partial \tilde{\mathbf{w}}}(\tilde{\mathbf{w}}, \mathbf{n}) \cdot b = \begin{bmatrix} \frac{\partial l_1^T}{\partial \tilde{\mathbf{w}}}(\tilde{\mathbf{w}}, \mathbf{n}) \cdot b \\ \frac{\partial l_2^T}{\partial \tilde{\mathbf{w}}}(\tilde{\mathbf{w}}, \mathbf{n}) \cdot b \\ \frac{\partial l_3^T}{\partial \tilde{\mathbf{w}}}(\tilde{\mathbf{w}}, \mathbf{n}) \cdot b \\ \frac{\partial l_4^T}{\partial \tilde{\mathbf{w}}}(\tilde{\mathbf{w}}, \mathbf{n}) \cdot b \\ \frac{\partial l_5^T}{\partial \tilde{\mathbf{w}}}(\tilde{\mathbf{w}}, \mathbf{n}) \cdot b \end{bmatrix} \quad (6.34)$$

$$\frac{\partial l_1}{\partial \tilde{\mathbf{w}}}(\tilde{\mathbf{w}}, \mathbf{n}) = \begin{bmatrix} -\frac{n_1(\gamma-1)\|\mathbf{v}\|^2}{2\rho c^2} & -\frac{n_1(\gamma-1)v_1}{c^2} & -\frac{n_1(\gamma-1)v_2}{c^2} & -n_3 & -\frac{n_1(\gamma-1)v_3}{c^2} + n_2 & \frac{n_1(\gamma-1)\|\mathbf{v}\|^2}{2\rho c^2} \\ \frac{n_1(\gamma-1)v_1}{\gamma p} & \frac{n_1\rho(\gamma-1)}{\gamma p} & 0 & 0 & 0 & -\frac{n_1v_1\rho(\gamma-1)}{\gamma p^2} \\ \frac{n_1(\gamma-1)v_2}{\gamma p} & 0 & \frac{n_1\rho(\gamma-1)}{\gamma p} & 0 & 0 & -\frac{n_1v_2\rho(\gamma-1)}{\gamma p^2} \\ \frac{n_1(\gamma-1)v_3}{\gamma p} & 0 & 0 & \frac{n_1\rho(\gamma-1)}{\gamma p} & 0 & -\frac{n_1v_3\rho(\gamma-1)}{\gamma p^2} \\ -\frac{n_1\gamma-1}{\rho c^2} & 0 & 0 & 0 & 0 & \frac{n_1\gamma-1}{pc^2} \end{bmatrix} \quad (6.35)$$

$$\frac{\partial l_2}{\partial \tilde{\mathbf{w}}}(\tilde{\mathbf{w}}, \mathbf{n}) = \begin{bmatrix} -\frac{n_2(\gamma-1)\|\mathbf{v}\|^2}{2\rho c^2} & -\frac{n_2(\gamma-1)v_1}{c^2} + n_3 & -\frac{n_2(\gamma-1)v_2}{c^2} & -\frac{n_2(\gamma-1)v_3}{c^2} - n_1 & \frac{n_2(\gamma-1)\|\mathbf{v}\|^2}{2\rho c^2} \\ \frac{n_2(\gamma-1)v_1}{\gamma p} & \frac{n_2\rho(\gamma-1)}{\gamma p} & 0 & 0 & -\frac{n_2v_1\rho(\gamma-1)}{\gamma p^2} \\ \frac{n_2(\gamma-1)v_2}{\gamma p} & 0 & \frac{n_2\rho(\gamma-1)}{\gamma p} & 0 & -\frac{n_2v_2\rho(\gamma-1)}{\gamma p^2} \\ \frac{n_2(\gamma-1)v_3}{\gamma p} & 0 & 0 & \frac{n_2\rho(\gamma-1)}{\gamma p} & -\frac{n_2v_3\rho(\gamma-1)}{\gamma p^2} \\ -\frac{n_2\gamma-1}{\rho c^2} & 0 & 0 & 0 & \frac{n_2\gamma-1}{pc^2} \end{bmatrix} \quad (6.36)$$

$$\frac{\partial l_3}{\partial \tilde{\mathbf{w}}}(\tilde{\mathbf{w}}, \mathbf{n}) = \begin{bmatrix} -\frac{n_3(\gamma-1)\|\mathbf{v}\|^2}{2\rho c^2} & -\frac{n_3(\gamma-1)v_1}{c^2} - n_2 & -\frac{n_3(\gamma-1)v_2}{c^2} + n_1 & -\frac{n_3(\gamma-1)v_3}{c^2} & \frac{n_3(\gamma-1)\|\mathbf{v}\|^2}{2\rho c^2} \\ \frac{n_3(\gamma-1)v_1}{\gamma p} & \frac{n_3\rho(\gamma-1)}{\gamma p} & 0 & 0 & -\frac{n_3v_1\rho(\gamma-1)}{\gamma p^2} \\ \frac{n_3(\gamma-1)v_2}{\gamma p} & 0 & \frac{n_3\rho(\gamma-1)}{\gamma p} & 0 & -\frac{n_3v_2\rho(\gamma-1)}{\gamma p^2} \\ \frac{n_3(\gamma-1)v_3}{\gamma p} & 0 & 0 & \frac{n_3\rho(\gamma-1)}{\gamma p} & -\frac{n_3v_3\rho(\gamma-1)}{\gamma p^2} \\ -\frac{n_3\gamma-1}{\rho c^2} & 0 & 0 & 0 & \frac{n_3\gamma-1}{pc^2} \end{bmatrix} \quad (6.37)$$

$$\frac{\partial l_4}{\partial \tilde{\mathbf{w}}}(\tilde{\mathbf{w}}, \mathbf{n}) = \begin{bmatrix} \frac{c}{2\rho} \mathbf{v} \cdot \mathbf{n} & (\gamma-1)v_1 - cn_1 & (\gamma-1)v_2 - cn_2 & (\gamma-1)v_3 - cn_3 & -\frac{c}{2p} \mathbf{v} \cdot \mathbf{n} \\ -\frac{cn_1}{2\rho} & -(\gamma-1) & 0 & 0 & \frac{cn_1}{2p} \\ -\frac{cn_2}{2\rho} & 0 & -(\gamma-1) & 0 & \frac{cn_2}{2p} \\ -\frac{cn_3}{2\rho} & 0 & 0 & -(\gamma-1) & \frac{cn_3}{2p} \\ 0 & 0 & 0 & 0 & 0 \end{bmatrix} \quad (6.38)$$

$$\frac{\partial l_5}{\partial \tilde{\mathbf{w}}}(\tilde{\mathbf{w}}, \mathbf{n}) = \begin{bmatrix} \frac{c}{2\rho} \mathbf{v} \cdot \mathbf{n} & (\gamma - 1)v_1 - cn_1 & (\gamma - 1)v_2 - cn_2 & (\gamma - 1)v_3 - cn_3 & -\frac{c}{2p} \mathbf{v} \cdot \mathbf{n} \\ \frac{cn_1}{2\rho} & -(\gamma - 1) & 0 & 0 & -\frac{cn_1}{2p} \\ \frac{cn_2}{2\rho} & 0 & -(\gamma - 1) & 0 & -\frac{cn_2}{2p} \\ \frac{cn_3}{2\rho} & 0 & 0 & -(\gamma - 1) & -\frac{cn_3}{2p} \\ 0 & 0 & 0 & 0 & 0 \end{bmatrix} \quad (6.39)$$

Therefor, the numerical roe flux (6.17) can therefore be derived by the primitive state vector as:

$$\begin{aligned} \frac{\partial \tilde{\phi}}{\partial \tilde{\mathbf{w}}_i} &= \frac{1}{2} \mathcal{A}(\tilde{\mathbf{w}}_i, \tilde{\mathbf{w}}_j) \\ &\quad - \frac{1}{2} \left[\left(\frac{\partial \mathbf{P}^{-1}}{\partial \tilde{\mathbf{w}}}(\sim) \frac{\partial \mathbf{M}}{\partial \tilde{\mathbf{w}}}(\sim) \right) |\Lambda(\sim)| \mathbf{P}(\sim) (\tilde{\mathbf{w}}_j - \tilde{\mathbf{w}}_i) \right. \\ &\quad + \mathbf{P}^{-1}(\sim) \left(\frac{\partial |\Lambda|}{\partial \tilde{\mathbf{w}}}(\sim) \frac{\partial \mathbf{M}}{\partial \tilde{\mathbf{w}}}(\sim) \right) \mathbf{P}(\sim) (\tilde{\mathbf{w}}_j - \tilde{\mathbf{w}}_i) \\ &\quad + \mathbf{P}^{-1}(\sim) |\Lambda(\sim)| \left(\frac{\partial \mathbf{P}}{\partial \tilde{\mathbf{w}}}(\sim) \frac{\partial \mathbf{M}}{\partial \tilde{\mathbf{w}}}(\sim) \right) (\tilde{\mathbf{w}}_j - \tilde{\mathbf{w}}_i) \\ &\quad \left. - \mathbf{P}^{-1}(\sim) |\Lambda(\sim)| \mathbf{P}(\sim) \right] \end{aligned} \quad (6.40)$$

where the full analytic expression can be obtained by backward substitution of equations (6.18) to (6.39).

This derivative, along with the derivative of the viscous term, which will be derived in chapters 6.1.2 and 6.3.2, will be a key component in the Sensitivity calculations as shown in Section 5 and 7. This is due to the fact that will follow the procedere of discretization before derivation as justified in Section 5.2.

6.3 Derivative with respect to the abstract variable $\frac{\partial \mathbf{R}}{\partial s}$

Since the fluid Jacobian is also required in every standard fluid solve, the important term, unique to SA is the partial derivative of the residual with respect to the design variable s .

Similar to the previously discussed fluid Jacobian, the computation of $\frac{\partial \mathbf{R}}{\partial s}$ can be splitted into convective and viscous part. We again focus on the special case of an

intersected cell in the following two sections, since the standard case of a standard cell far from the interface follows trivially from that.

It shall also be noted that in most cases, the derivative $\frac{\partial \mathbf{R}}{\partial s}$ is non-zero only at a few fluid nodes. For shape-sensitivity, for example, only the nodes at the interface have a non-zero contribution. Looking at equation (5.17) one can therefore interpret the solution of the linear system, or the multiplication with the inverse Jacobian, as a propagation operation.

6.3.1 Convective contribution to $\frac{\partial \mathbf{R}}{\partial s}$

Generally, one can write the convective fluid residual as

$$\mathbf{R}_{ij}^{c,i} = \phi_{ij}^i(\tilde{\mathbf{w}}_{ij}, \tilde{\mathbf{w}}_{ij}^*(s), \mathbf{n}_{ij}) \quad (6.41)$$

The most important factor here is of course the dependency of the half Riemann solution on the abstract variable. This dependency becomes obvious in the case of shape sensitivity, since the intersection point used for the Riemann solution depends upon the interface shape.

The derivative can be obtained straightforwardly as

$$\frac{\partial \mathbf{R}_{ij}^{c,i}}{\partial s} = \frac{\partial \mathbf{R}_{ij}^{c,i}}{\partial \mathbf{w}_{ij}^*} \frac{\partial \mathbf{w}_{ij}^*}{\partial s} \quad (6.42)$$

here, the analytical derivative of the first term can be taken from chapter 6.1. The second derivative is more cumbersome. The issue is visualized in Figure 6.1.

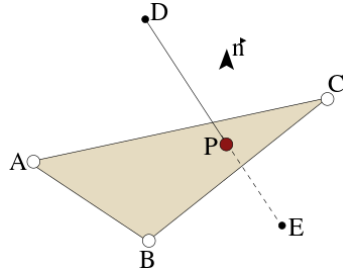


Figure 6.1: Visualization of the intersection of a fluid mesh edge (D – E) with an element of the embedded surface (A – B – C). For a shape-sensitivity analysis, SDesign returns the derivatives of the embedded surface nodes A, B, C position with respect to the shape parameter. This is done by first computing the intersection point P. Together with the element normal \mathbf{n} , the intersection point is used to reconstruct the shape derivatives at nodes D and E.

Based on the consideration above, we find the following dependency

$$\frac{\partial \mathbf{w}_{ij}^*}{\partial s} = \frac{\partial \mathbf{w}_{ij}^*}{\partial s} \left(\frac{\partial \mathbf{w}_i}{\partial s} \Big|_{i=A,B,C}, \xi, \mathbf{n} \right) \quad (6.43)$$

The derivatives of the geometrical quantities with respect to s are found as

$$\begin{aligned}\frac{\partial \xi}{\partial s} &= \frac{\partial \xi}{\partial \mathbf{x}} \frac{\partial \mathbf{x}}{\partial s} \\ \frac{\partial \mathbf{n}_{wall}}{\partial s} &= \frac{\partial \mathbf{n}_{wall}}{\partial \mathbf{x}} \frac{\partial \mathbf{x}}{\partial s}\end{aligned}\quad (6.44)$$

6.3.2 Viscous contribution to $\frac{\partial \mathbf{R}}{\partial s}$

The derivative of the viscous contribution is derived very similarly to the viscous Jacobian. Looking at equation (6.5) one can derive

$$\begin{aligned}\frac{\partial \mathbf{R}^v(s, \tilde{\mathbf{w}}^a(s), \tilde{\mathbf{w}}^g(\tilde{\mathbf{w}}^a(s)), \mathbf{x}(s))}{\partial s} &= \underbrace{\frac{\partial \mathbf{R}^v}{\partial \tilde{\mathbf{w}}^a} \frac{\partial \tilde{\mathbf{w}}^a}{\partial s}}_{\substack{\text{can be re-used from ALE} \\ \text{after the ghost-point population}}} + \frac{\partial \mathbf{R}^v}{\partial \tilde{\mathbf{w}}^g} \cdot \underbrace{\frac{\partial \tilde{\mathbf{w}}^g}{\partial \tilde{\mathbf{w}}^a}}_{\substack{\text{obtained during the} \\ \text{population process}}} \frac{\partial \tilde{\mathbf{w}}^a}{\partial s} \\ &+ \underbrace{\frac{\partial \mathbf{R}}{\partial \mathbf{x}} \frac{\partial \mathbf{x}}{\partial s}}_{=0 \text{ for embedded}}\end{aligned}\quad (6.45)$$

Chapter 7

Aero-elastic Sensitivity Analysis

Contents

7.1	Direct and adjoint approach	58
7.1.1	Direct Sensitivity Analysis for the Euler equations	60
7.1.2	Adjoint Sensitivity Analysis for the Euler equations	62

The previous chapter dealt with the **SA** of a pure fluid problem. Boundary, or respectively mesh-movement in general, was only introduced due to shape variation via design variables itself. However, one can easily conceive a system, where the fluid interacts with an elastic structure. This introduces an additional dependency of the structure shape, and thus fluid-structure interface, on the fluid solution. Also, a fully coupled system shows a direct connection between the stress resultants in the structure with the fluid solution. This chapter therefore investigates the **SA** of such a coupled system of equations. Considerations are built upon the derivations in chapter 5 and the coupled three-field **FSI** formulation described in chapter 3.2.

The **SA** approach applied in this thesis is based on the work of [25], for deriving the Global Sensitivity Equations (**GSE**) of coupled systems. As introduced by the authors of [18], we utilize the three-field formulation of [5].

The derivative of the optimization criterion q_j , as introduced in Equation (4.3), with respect to the optimization variable s_i gives:

$$\frac{dq_j}{ds_i} = \frac{\partial q_j}{\partial s_i} + \frac{\partial q_j}{\partial \mathbf{u}} \frac{d\mathbf{u}}{ds_i} + \frac{\partial q_j}{\partial \dot{\mathbf{x}}} \frac{d\dot{\mathbf{x}}}{ds_i} + \frac{\partial q_j}{\partial \mathbf{w}} \frac{d\mathbf{w}}{ds_i} \quad (7.1)$$

$$= \frac{\partial q_j}{\partial s_i} + \begin{bmatrix} \frac{\partial q_j}{\partial \mathbf{u}} \\ \frac{\partial q_j}{\partial \dot{\mathbf{x}}} \\ \frac{\partial q_j}{\partial \mathbf{w}} \end{bmatrix}^T \cdot \begin{bmatrix} \frac{d\mathbf{u}}{ds_i} \\ \frac{d\dot{\mathbf{x}}}{ds_i} \\ \frac{d\mathbf{w}}{ds_i} \end{bmatrix} \quad (7.2)$$

where the partial derivatives, $\frac{\partial q_j}{\partial \mathbf{u}}$, $\frac{\partial q_j}{\partial \dot{\mathbf{x}}}$ and $\frac{\partial q_j}{\partial \mathbf{w}}$ can be directly evaluated within the discretized structure and fluid model through the relation between structural, aero-dynamic design and abstract optimization parameters defied in the design model 4.2. The cumbersome part are the derivatives $\frac{d\mathbf{u}}{ds_i}$, $\frac{d\dot{\mathbf{x}}}{ds_i}$ and $\frac{d\mathbf{w}}{ds_i}$. To obtain them, the governing equations (3.1)(3.2)(3.3) have to be derived:

$$\begin{bmatrix} \frac{\partial \mathcal{S}_{gov}}{\partial s_i} \\ \frac{\partial \mathcal{D}_{gov}}{\partial s_i} \\ \frac{\partial \mathcal{F}_{gov}}{\partial s_i} \end{bmatrix} + \underbrace{\begin{bmatrix} \frac{\partial \mathcal{S}_{gov}}{\partial \mathbf{u}} & \frac{\partial \mathcal{S}_{gov}}{\partial \dot{\mathbf{x}}} & \frac{\partial \mathcal{S}_{gov}}{\partial \mathbf{w}} \\ \frac{\partial \mathcal{D}_{gov}}{\partial \mathbf{u}} & \frac{\partial \mathcal{D}_{gov}}{\partial \dot{\mathbf{x}}} & \mathbf{0} \\ \mathbf{0} & \frac{\partial \mathcal{F}_{gov}}{\partial \dot{\mathbf{x}}} & \frac{\partial \mathcal{F}_{gov}}{\partial \mathbf{w}} \end{bmatrix}}_{\mathbf{A}} \begin{bmatrix} \frac{\partial \mathbf{u}}{\partial s_i} \\ \frac{\partial \dot{\mathbf{x}}}{\partial s_i} \\ \frac{\partial \mathbf{w}}{\partial s_i} \end{bmatrix} = \mathbf{0} \quad (7.3)$$

In this equations $\frac{\partial \mathcal{S}_{gov}}{\partial s_i}$ and $\frac{\partial \mathcal{F}_{gov}}{\partial s_i}$ can be again directly evaluated using the relation specified in the design model. The matrix of first derivatives \mathbf{A} is from now on denoted as the *Jacobian of the optimization problem*.

Combining the previous two equations, it follows that the total derivative of the optimization criterion with respect to the abstract variables can be expressed as:

$$\frac{dq_j}{ds_i} = \frac{\partial q_j}{\partial s_i} - \underbrace{\begin{bmatrix} \frac{\partial q_j}{\partial \mathbf{u}} \\ \frac{\partial q_j}{\partial \dot{\mathbf{x}}} \\ \frac{\partial q_j}{\partial \mathbf{w}} \end{bmatrix}}_{n_q \times n_{eq}}^T \underbrace{\mathbf{A}^{-1}}_{n_{eq} \times n_{eq}} \begin{bmatrix} \frac{\partial \mathcal{S}_{gov}}{\partial s_i} \\ \frac{\partial \mathcal{D}_{gov}}{\partial s_i} \\ \frac{\partial \mathcal{F}_{gov}}{\partial s_i} \end{bmatrix} \quad (7.4)$$

Where n_{eq} is the total number of equations(e.g. five fluid state equations for the compressible NSE in 3D, three equations of the mesh motions and another three equations for the structure motion), n_q is the number of optimization criteria and n_s is the number of abstract variables.

7.1 Direct and adjoint approach

Looking at the above equation 7.4 one can identify a matrix-matrix-matrix product. Matrix-matrix products are not commutative, one can, however, perform the

following transformation

$$\begin{aligned}
 \mathbf{ABC} &= \mathbf{A}(\mathbf{BC}) \\
 [\mathbf{A}(\mathbf{BC})]^T &= (\mathbf{BC})^T \mathbf{A}^T = \mathbf{C}^T \mathbf{B}^T \mathbf{A}^T = \mathbf{C}^T (\mathbf{AB})^T \\
 \rightarrow \mathbf{ABC} &= \left[\mathbf{C}^T (\mathbf{AB}) \right]^T
 \end{aligned} \tag{7.5}$$

Depending on the sizes of the involved matrices one or the other form might be advantageous. Specifically, the straight forward way of computing the triple product is known as the *direct approach* and the transposed matrix way is called the *adjoint approach*.

Direct approach In the direct approach, one first computes the derivatives of the aeroelastic response for each abstract variable and then performs the matrix product with \mathbf{A} in equation (7.4):

$$\begin{bmatrix} \frac{d\mathbf{u}}{ds_i} \\ \frac{d\dot{\mathbf{x}}}{ds_i} \\ \frac{d\mathbf{w}}{ds_i} \end{bmatrix} = -\mathbf{A}^{-1} \begin{bmatrix} \frac{\partial \mathcal{S}_{gov}}{\partial s_i} \\ \frac{\partial \mathcal{D}_{gov}}{\partial s_i} \\ \frac{\partial \mathcal{F}_{gov}}{\partial s_i} \end{bmatrix} \quad \text{and then} \tag{7.6}$$

$$\frac{dq_j}{ds_i} = \frac{\partial q_j}{\partial s_i} - \begin{bmatrix} \frac{\partial q_j}{\partial \mathbf{u}} \\ \frac{\partial q_j}{\partial \dot{\mathbf{x}}} \\ \frac{\partial q_j}{\partial \mathbf{w}} \end{bmatrix}^T \begin{bmatrix} \frac{d\mathbf{u}}{ds_i} \\ \frac{d\dot{\mathbf{x}}}{ds_i} \\ \frac{d\mathbf{w}}{ds_i} \end{bmatrix} \tag{7.7}$$

By standard algebra theory, the total complexity of this computation can be approximated as $\mathcal{O}(n_{eq}^2 n_s + n_q n_{eq} n_s)$

Adjoint approach In the adjoint approach one first computes the derivatives of the optimization criteria and then multiplies with the Jacobian before substituting

this into Equation (7.4):

$$\begin{bmatrix} \mathbf{a}_u \\ \mathbf{a}_{\dot{x}} \\ \mathbf{a}_w \end{bmatrix} = \mathbf{A}^{-T} \begin{bmatrix} \frac{\partial q_j}{\partial u} \\ \frac{\partial q_j}{\partial \dot{x}} \\ \frac{\partial q_j}{\partial w} \end{bmatrix} \quad (7.8)$$

$$\frac{dq_j}{ds_i} = \frac{\partial q_j}{\partial s_i} - \begin{bmatrix} \mathbf{a}_u \\ \mathbf{a}_{\dot{x}} \\ \mathbf{a}_w \end{bmatrix}^T \begin{bmatrix} \frac{\partial \mathcal{S}_{gov}}{\partial s_i} \\ \frac{\partial \mathcal{D}_{gov}}{\partial s_i} \\ \frac{\partial \mathcal{F}_{gov}}{\partial s_i} \end{bmatrix} \quad (7.9)$$

Here the total complexity can be approximated as $\mathcal{O}(n_{eq}^2 n_q + n_q n_{eq} n_s)$

If one or the other approach is to be preferred depends on the optimization setup, particularly the number of optimization criteria and the number of optimization variables. Looking at the orders above, one can conclude that if the number of abstract parameters n_s is smaller than the number of optimization criteria, the direct approach is more efficient, otherwise the adjoint approach is to be preferred. Additionally one can argue, that the relevant term in the orders above is the one with n_{eq}^2 since it dominates the sum. Therefore, depending on whether n_s or n_q is bigger, the direct or the adjoint method is to be preferred.

7.1.1 Direct Sensitivity Analysis for the Euler equations

The \mathbf{A} matrix for the direct approach in ALE formulation can be written as

$$\mathbf{A} = \begin{bmatrix} \frac{\partial \mathcal{S}_{gov}}{\partial u} & \frac{\partial \mathcal{S}_{gov}}{\partial \dot{x}} & \frac{\partial \mathcal{S}_{gov}}{\partial w} \\ \frac{\partial \mathcal{D}_{gov}}{\partial u} & \frac{\partial \mathcal{D}_{gov}}{\partial \dot{x}} & \mathbf{0} \\ \mathbf{0} & \frac{\partial \mathcal{F}_{gov}}{\partial \dot{x}} & \frac{\partial \mathcal{F}_{gov}}{\partial w} \end{bmatrix} = \begin{bmatrix} \boldsymbol{\kappa} & \frac{\partial \mathbf{P}_T}{\partial \dot{x}} & \frac{\partial \mathbf{P}_T}{\partial w} \\ \begin{bmatrix} \boldsymbol{\kappa}_{\Omega\Gamma} \mathbf{T}_u \\ \mathbf{T}_u \end{bmatrix} & \begin{bmatrix} \boldsymbol{\kappa}_{\Omega\Omega} & \mathbf{0} \\ \mathbf{0} & \mathbf{I} \end{bmatrix} & \mathbf{0} \\ \mathbf{0} & \frac{\partial \mathbf{F}_2}{\partial \dot{x}_\Omega} & \mathbf{H}_2 \end{bmatrix} \quad (7.10)$$

Where, \mathbf{H}_2 is the Jacobian of the second order row flux. It shall be noted that constructing this Jacobian is not a trivial issue and takes up a lot of computational

resources, especially for **FV**, as described in [5]. Investigation into whether this term can be approximated at first order were carried out in [18] and [19].

Furthermore, [21] considered replacing the two mesh motion related matrices $\frac{\partial \mathbf{P}_T}{\partial \dot{\mathbf{x}}}$ and $\frac{\partial \mathbf{F}_2}{\partial \dot{\mathbf{x}}_\Omega}$ by a transpirational boundary condition. The consequences of this approach are also investigated in [18] and [19].

This thesis, however, does not use any of this simplifications.

The derivation of the sensitivities, can be achieved in a staggered scheme, very similar to the one, described in 3.2. It consists of five steps.

1) Update the structural displacement sensitivity to a new time step By differentiating equations (3.1) and (3.4) and applying an under relaxation, we can obtain

$$\frac{d\mathbf{u}^{(n)}}{ds_i} = (1 - \theta) \frac{d\mathbf{u}^{(n)}}{ds_i} + \theta \frac{d\bar{\mathbf{u}}}{ds_i} \quad (7.11)$$

where $\bar{\mathbf{u}}$ is obtained from:

$$\mathbf{K} \frac{d\bar{\mathbf{u}}}{ds_i} = \frac{\partial \mathbf{P}_T}{\partial s_i} + \frac{\partial \mathbf{T}_u^{(n)}}{\partial s_i} - \frac{\partial \mathbf{K}}{\partial s_i} \mathbf{u} \quad (7.12)$$

2) Transfer sensitivity of structure motion to the interface

$$\frac{d\mathbf{u}_T^{(n)}}{ds_i} = \mathbf{T}_u \frac{d\mathbf{u}^{(n)}}{ds_i} \quad (7.13)$$

3) Compute derivative of the fluid mesh motion The fluid mesh motion is computed by solving the pseudo Dirichlet problem as described in [5]. By design, the fictitious stiffness matrix \mathbf{K} does not depend on the abstract optimization variables \mathbf{s}

$$\bar{\mathbf{K}}_{\Omega\Omega} \frac{d\dot{\mathbf{x}}_\Omega^{(n)}}{ds_i} = -\bar{\mathbf{K}}_{\Omega\Gamma} \frac{d\dot{\mathbf{x}}_\Gamma^{(n)}}{ds_i} \quad (7.14)$$

with

$$\frac{d\dot{\mathbf{x}}_\Gamma^{(n)}}{ds_i} = \frac{d\dot{\mathbf{x}}_\Gamma^{(n)}}{ds_i} \quad (7.15)$$

4) Compute the sensitivity of the fluid state variables The derivatives of the fluid state variables are computed by

$$\mathbf{H}_2 \frac{dw^{(n+1)}}{ds_i} = \frac{\partial \mathbf{F}_2}{\partial s_i} - \frac{\partial \mathbf{F}_2}{\partial \dot{\mathbf{x}}} \frac{d\dot{\mathbf{x}}}{ds_i} \quad (7.16)$$

5) Compute the sensitivity of the structure load vector The derivative of the fluid load with respect to the abstract variables can be computed by the third of Equations (7.6) with the definition of \mathbf{A} as specified in (7.10).

$$\frac{\partial \mathbf{P}_F^{(n+1)}}{\partial s_i} = \frac{\partial \mathbf{P}_F^{(n+1)}}{\partial \dot{\mathbf{x}}} \frac{d\dot{\mathbf{x}}^{(n)}}{ds_i} + \frac{\partial \mathbf{P}_F^{(n+1)}}{\partial \mathbf{w}} \frac{d\mathbf{w}^{(n)}}{ds_i} \quad (7.17)$$

and compute project it onto the structure via

$$\frac{\partial \mathbf{P}_T^{(n+1)}}{\partial s_i} = \mathbf{T}_p \frac{\partial \mathbf{P}_F^{(n+1)}}{\partial s_i} \quad (7.18)$$

Finally, the convergence of the staggered algorithm can be monitored via

$$\begin{aligned} & \left\| \mathbf{K} \frac{d\bar{\mathbf{u}}^{(n+1)}}{ds_i} - \frac{\partial \mathbf{P}_T}{\partial s_i} - \frac{\partial \mathbf{P}_T^{(n+1)}}{\partial s_i} + \frac{\partial \mathbf{K}}{\partial s_i} \right\|_2 \leq \\ & \epsilon^{SA} \left\| \mathbf{K} \frac{d\bar{\mathbf{u}}^{(0)}}{ds_i} - \frac{\partial \mathbf{P}_T}{\partial s_i} - \frac{\partial \mathbf{P}_T^{(0)}}{\partial s_i} + \frac{\partial \mathbf{K}}{\partial s_i} \right\|_2 \\ & \left\| \mathbf{H}_2 \frac{d\mathbf{w}^{(n+1)}}{ds_i} + \frac{\partial \mathbf{F}_2}{\partial s_i} + \frac{\partial \mathbf{F}_2}{\partial \dot{\mathbf{x}}} \frac{d\dot{\mathbf{x}}^{(n+1)}}{ds_i} \right\|_2 \leq \\ & \epsilon^{SA} \left\| \mathbf{H}_2 \frac{d\mathbf{w}^{(0)}}{ds_i} + \frac{\partial \mathbf{F}_2}{\partial s_i} + \frac{\partial \mathbf{F}_2}{\partial \dot{\mathbf{x}}} \frac{d\dot{\mathbf{x}}^{(0)}}{ds_i} \right\|_2 \end{aligned} \quad (7.19)$$

7.1.2 Adjoint Sensitivity Analysis for the Euler equations

The adjoint SA follows the same scheme as the direct one
Equation (7.8) can be written as:

$$\begin{bmatrix} \mathbf{K} & \begin{bmatrix} \frac{\partial \mathbf{P}_T}{\partial \dot{\mathbf{x}}_\Omega} & \frac{\partial \mathbf{P}_T}{\partial \dot{\mathbf{x}}_\Gamma} \end{bmatrix}^T & \frac{\partial \mathbf{P}_T}{\partial \mathbf{w}} \\ \begin{bmatrix} \mathbf{K}_{\Omega\Gamma} \mathbf{T}_u \\ \mathbf{T}_u \end{bmatrix} & \begin{bmatrix} \mathbf{K}_{\Omega\Omega} & \mathbf{0} \\ \mathbf{0} & \mathbf{I} \end{bmatrix} & \mathbf{0} \\ \mathbf{0} & \begin{bmatrix} \frac{\partial \mathbf{F}_2}{\partial \dot{\mathbf{x}}_\Omega} & \frac{\partial \mathbf{F}_2}{\partial \dot{\mathbf{x}}_\Gamma} \end{bmatrix} & \mathbf{H}_2 \end{bmatrix} \begin{bmatrix} \mathbf{a}_u \\ \mathbf{a}_{\dot{\mathbf{x}}_\Omega} \\ \mathbf{a}_{\dot{\mathbf{x}}_\Gamma} \\ \mathbf{a}_w \end{bmatrix} = \begin{bmatrix} \frac{\partial q_j}{\partial \mathbf{u}} \\ \frac{\partial \mathbf{q}}{\partial \dot{\mathbf{x}}_\Omega} \\ \frac{\partial \mathbf{q}}{\partial \dot{\mathbf{x}}_\Gamma} \\ \frac{\partial q_j}{\partial \mathbf{w}} \end{bmatrix} \quad (7.20)$$

A stated earlier, the matrices $\frac{\partial \mathbf{q}}{\partial \dot{\mathbf{x}}}$ and $\frac{\partial \mathbf{q}}{\partial \mathbf{w}}$ can be computed analytically. As for \mathbf{H}_2 , we follow the methodology outlined in [13] for evaluating and storing it efficiently

as the product of flux operators. Again the staggered procedure for solving the adjoint state problem shares the same computational kernels with the partitioned aeroelastic scheme described in [5]

1) Update the adjoint structure displacement to the new time step

$$\mathbf{a}_u^{(n+1)} = (1 - \theta)\mathbf{a}_u^{(n)} + \theta\bar{\mathbf{a}}_u^{(n+1)} \quad (7.21)$$

where $\bar{\mathbf{a}}_u^{(n+1)}$ is obtained from

$$\mathbf{K}\bar{\mathbf{a}}_u^{(n+1)} = \frac{\partial \mathbf{q}}{\partial \mathbf{u}} - \mathbf{K}_{\Omega\Gamma} \mathbf{T}_u \mathbf{a}_{x\Omega}^{(n)} + \mathbf{T}_u \mathbf{a}_{x\Gamma}^{(n)} \quad (7.22)$$

2) Compute the adjoint fluid state by solving

$$\mathbf{H}_2^T \mathbf{a}_w^{(n+1)} = \frac{\partial \dot{\mathbf{x}}}{\partial \mathbf{w}} + \frac{\partial \mathbf{P}_T}{\partial \mathbf{w}^T} \mathbf{a}_u^{(n+1)} \quad (7.23)$$

Again, $\frac{\partial \mathbf{q}}{\partial \mathbf{w}}$ is computed analytically from the relations defined in the design and aeroelastic model.

3) Compute adjoint mesh motion in domain and on the interface

$$\bar{\mathbf{K}}_{\Omega\Omega} \mathbf{a}_{x\Omega}^{(n+1)} = \frac{\partial \mathbf{q}}{\partial \dot{\mathbf{x}}_\Omega} - \frac{\partial \mathbf{P}_T}{\partial \dot{\mathbf{x}}_\Omega} \mathbf{a}_u^{(n+1)} - \frac{\partial \mathbf{F}_1^T}{\partial \dot{\mathbf{x}}_\Omega} \mathbf{a}_x^{(n+1)} \text{ in } \Omega \quad (7.24)$$

And the adjoint mesh motion on the interface is computed as $\mathbf{a}_{x\Gamma}^{(n+1)}$

$$\mathbf{a}_{x\Gamma}^{(n+1)} = \frac{\partial \mathbf{q}}{\partial \dot{\mathbf{x}}_\Gamma} + \frac{\partial \mathbf{P}_T}{\partial \dot{\mathbf{x}}_\Gamma} \mathbf{a}_u^{(n+1)} - \frac{\partial \mathbf{F}_2}{\partial \dot{\mathbf{x}}}^T \text{ on } \Gamma \quad (7.25)$$

where $\frac{\partial \mathbf{q}}{\partial \mathbf{w}}$ is computed analytically.

The convergence of the staggered adjoint optimization algorithm can be monitored via

$$\left\| \mathbf{R}_q - \mathbf{A}^T \mathbf{a}^{(n+1)} \right\| \leq \epsilon^{SA} \left\| \mathbf{R}_q \right\| \quad (7.26)$$

Chapter 8

The Embedded Boundary Method - FIVER

Contents

8.1	Setup	66
8.2	Evaluation of the inviscid term at the interface	66
8.2.1	First order FIVER	67
8.2.2	Second order FIVER	68
8.3	Evaluation of the viscous terms at the interface	69
8.3.1	Reconstruction of the fluid-state at ghost-nodes	70
8.4	Evaluation of forces	71
8.5	The level-set method	71

It was already outlined in Section 1, that using an Eulerian approach int the context of an aeroelastic simulation leads to a so-called embedded formulation, where the interface of the structure mesh no longer coincides with the fluid mesh. This was appealing, since it allowed for the usage of fixed meshes and an Eulerian formulation, on the other hand as explained in Section 8.1, an error of the order $\mathcal{O}(\frac{h}{2})$ is introduced. A possible solution to recover second order convergence rate is quickly described in chapter 8.2.2.

For the solution of multi-material flows with immersed boundaries, the Finite Volume Method with exact two-phase Riemann Integrals (**FIVER**) has been developed in the Farhat Research Group (**FRG**). The basic concepts of **FIVER** have first been described in [6] in the context of two-phase compressible flows and underwater implosions. It has then be extended to fluid-structure interaction in [29]. Finally, an approach to restore a second order global rate of convergence has been presented in [16].

Unlike most other **IBM**, **FIVER** operates on arbitrary unstructured grids.

FIVER was also extended to implicit time discretization in [17] and to viscous, multi-material flows in [4].

The **FIVER** framework is characterized by two simple ideas:

- Keeping the underlying semi-discretization as close as possible to a Godunov-type scheme in order to facilitate its implementation in a large body of existing flow solvers.
- Solving at each material interface local, one-dimensional Riemann problems in order to avoid traversing explicitly this interface during the semi-discretization process and therefore achieve robustness with respect to strong contact discontinuities.

8.1 Setup

In this thesis, we consider embedded structure interfaces only. Whether the structure is deformable or rigid does not really make a difference for the subsequent considerations.

The basic setup is depicted in Figure 8.1.

A distinctive feature of the original **FIVER** method is the usage of the surrogate interface. This is also depicted in the figure. Several issues have to be addressed in an embedded framework. Firstly, the interface may move during the simulation. In fact, large deformations of the structure have been one of the motivations aspects for the development of an embedded framework in the first place. The question thus becomes how to track the interface during the simulation. This is addressed in chapter 8.5.

Secondly, the evaluation of the inviscid (8.1) and viscous (8.11) term becomes cumbersome for cells that are being intersected. We address this issue separate for the inviscid and the viscous term in chapters 8.2 and 8.3.

Finally, in an **FSI** simulation we are typically interested in integral quantities over the structure surface, e.g. the lift and drag values of an airfoil. We now have several possibilities to define the structure surface to perform integration over an embedded boundary. This issue will be discussed in chapter 8.4.

8.2 Evaluation of the inviscid term at the interface

For this chapter as well as for chapter 8.3 we consider Figure 8.1.

A question, that arises when looking at equation (2.11) is how to evaluate those terms for node i , where some of the vertices in $\kappa(i)$ are inactive ghost nodes.

We will answer this question for the inviscid term in this sections and look at the viscous term in the subsequent one.

First, we notice that we can split the summation as follows

$$\sum_{j \in \kappa(i)} \phi_{ij}(\mathbf{w}_i, \mathbf{w}_j, \boldsymbol{\nu}_{ij}) = \sum_{j \in \kappa(i)^a} \phi_{ij}(\mathbf{w}_i, \mathbf{w}_j, \boldsymbol{\nu}_{ij}) + \sum_{j \in \kappa(i) \setminus \kappa(i)^a} \phi_{ij}(\mathbf{w}_i, \mathbf{w}^*, \boldsymbol{\nu}_{ij}) \quad (8.1)$$

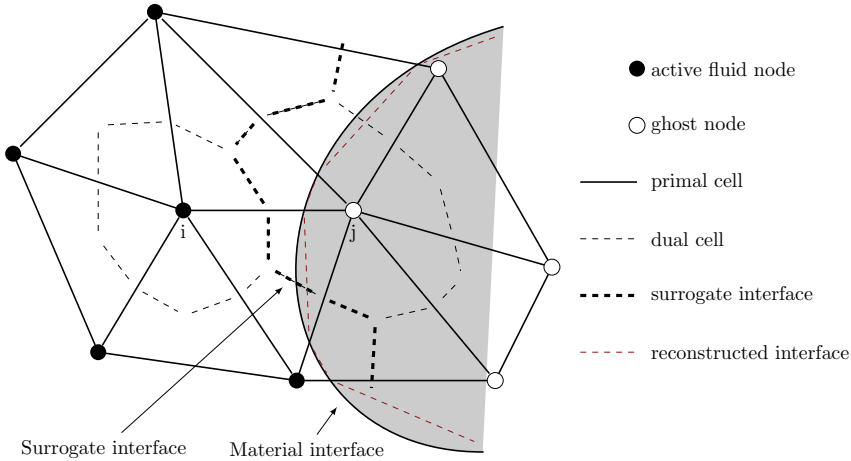


*Figure 8.1: Sketch of an embedded simulation setup. The primal grid is intersected by a material interface. In **FIVER**, the material interface is replaced by a surrogate interface that is created by connecting the dual-grid interfaces closest to the embedded surface. By connecting the intersection points of the embedded surface with the primal grid, we can also create a so-called, reconstructed surface that is particularly useful for the calculation of forces on the surface.*

where \mathbf{w}_* is the fluid state at the auxiliary intersection between edge ij and the auxiliary interface. To obtain \mathbf{w}_8 a one-sided Riemann problem is defined

$$\frac{\partial \tilde{\mathbf{w}}}{\partial t} = \frac{\partial \mathcal{F}}{\partial s}(\tilde{\mathbf{w}}) = \mathbf{0} \quad (8.2)$$

where s is the local abscissa along the direction ij , that has its origin in M_{ij} . The one sided Riemann problem can then be initialized with

$$\tilde{\mathbf{w}}_L = \begin{bmatrix} \rho_i & \mathbf{v}_i & p_i \end{bmatrix} \quad (8.3)$$

The exact solution of the one-sided, one-dimensional Riemann problem contains a constant (in time) state at the fluid-structure interface which is denoted here by

$$\mathbf{w}_* = \begin{bmatrix} \rho_* & \mathbf{v}_* & p_* \end{bmatrix} \quad (8.4)$$

which can then be used in equation (8.1)

8.2.1 First order **FIVER**

The original **FIVER** method was developed in [6]. As depicted in figure 8.1 it operates on the surrogate interface. As written in equation (8.5), a half Riemann problem is solved exactly in order to reconstruct a fluid state at the interface. This reconstructed fluid state is then used to formulate the numerical flux at the active vertex i (see equation (8.6)).

$$\begin{aligned}
 \frac{\partial \tilde{\mathbf{w}}^*}{\partial \tau} + \frac{\partial \tilde{f}(\tilde{\mathbf{w}}^*)}{\partial \xi} &= \mathbf{0} \\
 \tilde{f}^*(\xi, 0) &= \tilde{\mathbf{w}}_{ij} & \xi < 0 \\
 \mathbf{v}(0, \tau) \cdot \mathbf{n}_{wall} &= \mathbf{v}_{wall} \cdot \mathbf{n}_{wall} & 0 \leq t \leq \tau
 \end{aligned} \tag{8.5}$$

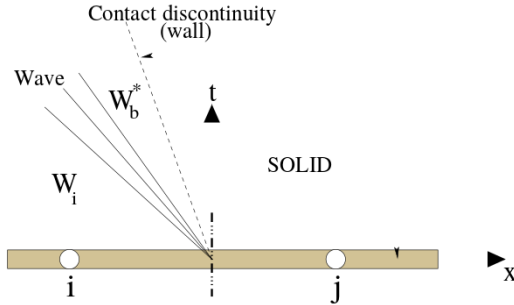


Figure 8.2: Solution of the 1D half Riemann problem around edge $i-j$ described in equation (8.2). The obtained fluid state at the interface is then used to evaluate the flux function, see equations (8.5) and (8.6)

$$\phi_{ij} = \phi_{ij}(\tilde{\mathbf{w}}_{ij}, \tilde{\mathbf{w}}_b^*, \mathbf{n}_{ij}) \tag{8.6}$$

8.2.2 Second order FIVER

The original version of **FIVER** has been outlined in chapter 8.2.1. This algorithm has been successfully applied to the solution of multi-phase flows, underwater implosion problems and fluid structure interaction. However, like most **IBM** it suffers one distinct disadvantage: global convergence drops to first order with an $\mathcal{O}(1)$ error at the interface. This observation motivated the generalization of FIVER to second order global accuracy performed in [16].

Here, we first extrapolate the fluid state at node i to the real intersection point with the interface (see Figure 8.1).

$$\mathbf{w}_\Gamma = \mathbf{w}_i + \nabla \mathbf{w}_i (\mathbf{x}_\Gamma - \mathbf{x}_i) \tag{8.7}$$

The one-dimensional half-Riemann problem is solved at the material interface Γ

$$\tilde{\mathbf{w}}_\Gamma^* = \tilde{\mathbf{w}}^*(\tilde{\mathbf{w}}_\Gamma, \mathbf{v}_{wall}, \mathbf{n}_{wall}) \tag{8.8}$$

Once this solution has been obtained inter-/extrapolate the fluid state back to the surrogate interface yielding $\tilde{\mathbf{w}}_{ij}^*$

$$\tilde{\mathbf{w}}_{ij}^* = \tilde{\mathbf{w}}_{ij}^*(\mathbf{w}_\Gamma^*, \mathbf{w}_i) \tag{8.9}$$

The numerical flux can then be evaluated the usual way using the obtained fluid state value:

$$\mathbf{R}_{ij}^c = \mathbf{R}_{ij}^c(\mathbf{w}_{ij}, \mathbf{w}_{ij}^*, \mathbf{n}_{ij}) \quad (8.10)$$

It has been proven in [16] that this approach recovers second order convergence in the vicinity of the interface and thus a second order global convergence can be achieved.

8.3 Evaluation of the viscous terms at the interface

Section 8.1 dealt with the general setup of an embedded simulation, chapter 8.2.1 introduced the first order version of **FIVER** for the inviscid term, which was then generalized to second order in chapter 8.2.2. So far, the interested reader might have noticed that the ghost nodes depicted in figure 8.1 have not yet been used. This is due to the **FV** treatment of the inviscid term and the formulation of half Riemann problems to the surrogate interface. The viscous terms, however, is treated differently.

We have shown and explained thoroughly the **FE** like evaluation of the viscous term (2.11) in chapter 2.3.

If one wants to keep the **FE**-like evaluation of the viscous term, (2.11) can be splitted as

$$\sum_{T_i \in \lambda(i)} \int_{T_i} \mathbb{K} \nabla \mathbf{w} \nabla \phi_i dx = \sum_{T_i \in (\lambda(i^a))} \int_{T_i} \mathbb{K} \nabla \mathbf{w} \nabla \phi_i dx + \sum_{T_i \in (\lambda(i) \setminus \lambda(i^a))} \int_{T_i} \mathbb{K} \nabla \mathbf{w}^R \nabla \phi_i dx = \quad (8.11)$$

where $\lambda(i^a)$ is the set of triangles that can be build from the active nodes around node i and $\lambda(i) \setminus \lambda(i^a)$ are all the triangles where at least one node is inactive(ghost).

The only difficulty now becomes the evaluation of the last term, meaning the integration over intersected elements, where at least one node is inactive, and thus does not have a fluid state solution.

We did not have that problem for the inviscid term of equation (2.11), since a **FV** approximation was chosen, and therefore we could construct a flux at the interface thanks to the half Riemann problem. No inactive node had to be considered.

For the viscous part, however, we want to keep the **FE** like formulations described in 2.3 to avoid re-writing large portions of the code. If a triangle is cut by the interface, one or two nodes will therefore be labeled inactive, and be denoted as ghost-nodes. Clearly, the fluid state vector at this ghost nodes is not defined. The question thus becomes how to evaluate this terms (last part in equation (8.11)).

The approach we take, that is also outlined in [4] is to reconstruct a pseudo fluid-state at the ghost points, such that the boundary conditions at the wall are fulfilled.

8.3.1 Reconstruction of the fluid-state at ghost-nodes

To explain the reconstruction at the ghost nodes, it again helps to consider Figure 8.1.

We also notice that the viscous flux, as defined in Equation 1.18, only depends on the fluid velocity and the temperature. Reconstruction of the velocity at the ghost node is straight forward. Assuming a linear interpolation inside the elements, the velocity at node i is reconstructed such, that the stick condition is fulfilled at the interface.

As far as the reconstruction of the temperature is concerned, two different cases have to be considered: adiabatic walls and isothermal walls.

For an adiabatic wall, the temperature gradient at the wall is zero, which can be achieved by setting the temperature of the ghost note equal to that of node i . An isothermal wall boundary condition enforces a certain, constant temperature at the wall. Similar to the velocity boundary condition, this can be achieved by finding an appropriate ghost point value such that the condition is enforced.

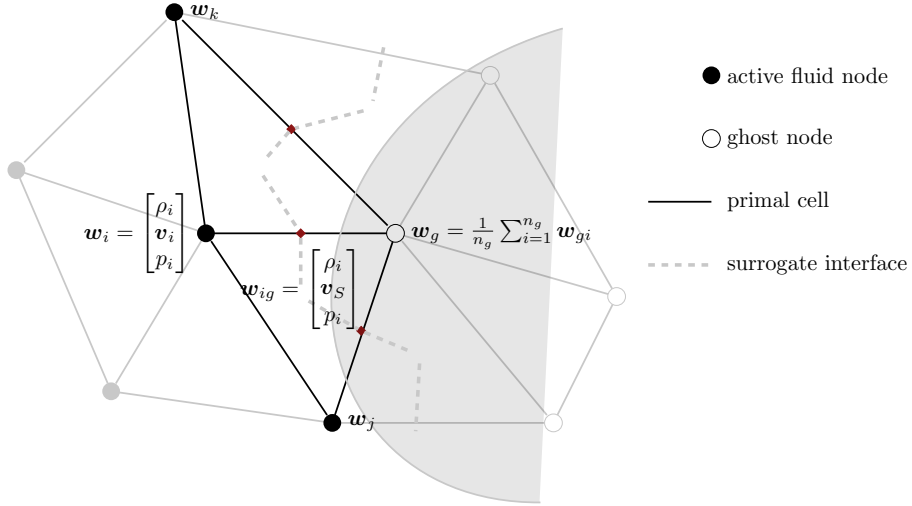


Figure 8.3: Illustration of the ghost point population process. States at nodes i, j, k are known from computation. States at mid-edges kg, ig and jg are the states we want to impose at the interface. The pressure and density are constantly extrapolated from the fluid states, whereas the velocity is set to the structure velocity at the interface. A linear extrapolation is then performed form the active states over the stated at the intersections points to obtain the interpolated ghost states. Since the interpolated ghost state values are typically ambiguous, due to multiple edges connecting to one ghost node, a least-square algorithm or a simple averaging can be performed to obtain a final value for the ghost state w_g .

The issue is depicted in detail in figure 8.3. The figure also reveals that there is no unique solution for the ghost point value. Multiple active node connect to the ghost node and the above described relations can be formulated for every one of them. **FIVER** therefore solves a least square system to chose an appropriate value.

The elegance of this approach is that once the ghost points states have been found, the evaluation of the viscous contribution can be done with the standard code routines. No adaption is required to make them work in the embedded framework.

8.4 Evaluation of forces

Another issue that arises for embedded simulations is the appropriate evaluation of the forces on an embedded interface. This is especially important if the embedded framework is used in an FSI setup to get an appropriate resultant on the structure. Sensitivity Analysis is another application, where appropriate evaluation of Lift and Drag integrals are crucial.

This problem has been analyzed in [31][30].

Most importantly, the question becomes whether to evaluate the pressure integral (5.3) over the auxiliary control volume interface (figure 8.1) or over the so called reconstructed interface, which can be obtained by creating auxiliary surfaces inside the intersected elements through the knowledge of intersection points at the edges. Detailed information about the intersection detection is provided in[29]

8.5 The level-set method

The issue of interface tracking is extensively discussed in [30] and [15].

Since the interface in an embedded stimulation typically moves, an appropriate interface tracking approach is required.

For **FIVER**, the popular level set method [24] was chosen.

The level set approach is characterized by the following equation:

$$\frac{\partial \phi}{\partial t} + \mathbf{v} \cdot \nabla \phi = 0 \Leftrightarrow \frac{\partial \phi}{\partial t} + \nabla \cdot (\mathbf{v}\phi) = -\phi \nabla \cdot \mathbf{v} \quad (8.12)$$

where ϕ is a function designed to track the material interface. Particularly, ϕ is initialized such that that the interface is characterized by $\phi = 0$. The interface can then be tracked via a simple discretization and time integration of equation (8.12). A periodic reinitialization of ϕ is sometimes necessary in order to maintain an optimal level of numerical accuracy.

Details of this approach, which was developed for computer visualization purposes, can be found in [24].

Chapter 9

Verification

Contents

9.1	Approach	73
9.2	Verification of $\frac{\partial \mathbf{w}}{\partial s}$	75
9.2.1	Mach-sensitivity	75
9.2.2	Shape-sensitivity	84
9.3	Verification of Lift and Drag results	93

After chapter 1 described the basic equations of fluid mechanics, discretization of this equations with FV and FE schemes in chapter 2, and an introduction to SA, the expressions for the actual derivatives have been derived in chapter 5. This has been done for both the body-fitted and the embedded 8 framework of AERO-F.

This chapter is denoted to a thorough validation of the obtained derivatives. As described in 5, AERO-F handles both sensitivities with respect to far-field variables(e.g. angle of attack) as well as shape sensitivities. Both types require to be handled fundamentally different. While the first type leads to derivatives mainly in the far field boundary conditions, the latter one interferes with the wall treatment. More importantly, as shown in chapters 6.1 and 6.3, in the embedded case, doing shape sensitivities leads to additional derivatives with regards to the intersector.

For all those reasons, the verification provided in this chapter deals with both M_∞ -sensitivity as well as shape-sensitivity. More over we will provide plots for both the body-fitted and the embedded case.

9.1 Approach

The question of how to verify the obtained sensitivities is anything but straightforward.

The first question is: What can be verified anyway?

If we have a look at equation (5.17), one can see, that there are two main derivatives:

$\frac{\partial \mathbf{R}}{\partial \mathbf{w}}$ and $\frac{\partial \mathbf{R}}{\partial s}$. The derivative with respect to the mesh position $\frac{\partial \mathbf{R}}{\partial \mathbf{x}}$ is not validated here, since it is obtained from SDESIGN and taken for granted.

The basic idea that we exploit for verification is to compute a reference solution for the sensitivities by a FD of two steady-state simulations. The advantage is, that the sensitivity-module does not have to be used at all to obtain those references, thus it is ensured that potential bugs are not carried over.

However, for both of the above quantities, computing a finite difference solution is cumbersome. For the Jacobian $\frac{\partial \mathbf{R}}{\partial \mathbf{w}}$ a simple forward difference would look as follows:

$$\left. \frac{\partial \mathbf{R}_i}{\partial \mathbf{w}_j} \right|_{\mathbf{w}_0} = \frac{\mathbf{R}_i(\mathbf{w}_0 + \epsilon \mathbf{e}_j) - \mathbf{R}_i(\mathbf{w}_0 - \epsilon \mathbf{e}_j)}{2\epsilon} \quad (9.1)$$

which would entail an $\mathcal{O}(N)$ number of residual evaluations.

As far as $\frac{\partial \mathbf{R}}{\partial s}$ goes, a FD verification would be feasible:

$$\begin{aligned} \frac{\partial \mathbf{R}_i}{\partial M_\infty} &= \frac{\mathbf{R}(\mathbf{w}_i^+) - \mathbf{R}(\mathbf{w}_i^-)}{2\epsilon} \\ \mathbf{w}_i^\pm &= \begin{cases} \mathbf{w}_i|_0 & \text{for internal nodes} \\ \mathbf{w}_i|_{\mathbf{w}_i(M_i=M_0+\epsilon)} & \text{for boundary nodes} \end{cases} \end{aligned} \quad (9.2)$$

which could be done cheaply, and is in fact done in AERO-F if the parameter `SensitivityAnalysis.SensitivityComputation` is set to `FiniteDifference`. However, it requires the fluid-state to be updated according to the Mach-number change at the fluid boundary and thus introduces a potential for bugs.

Instead, the first quantity to be validated in this thesis is the solution of the linear system described in equation (5.17): $\frac{\partial \mathbf{w}}{\partial s}$.

this can be done easily by performing a simple FD on the solution of two steady-state simulations;

$$\frac{d\mathbf{w}}{ds} = \frac{\mathbf{w}(s + \epsilon) - \mathbf{w}(s - \epsilon)}{2\epsilon} \quad (9.3)$$

which involves no extra coding and can be done with a standard steady state solver.

The validation of $\frac{d\mathbf{w}}{ds}$ is provided in figures [9.2,9.3,9.4] for the body fitted framework and figures [9.5,9.6,9.7] for the embedded.

Additionally, since the optimization will run on lift and drag, we also validate them with steady state results.

$$\frac{dq}{ds} = \frac{q(s + \epsilon) - q(s - \epsilon)}{2\epsilon} \quad (9.4)$$

The validation of integrated forces is provided in figures [9.18,9.19,9.20] for body-fitted computations and in figures [9.21,9.22,9.23] for embedded.

9.2. VERIFICATION OF $\frac{\partial \mathbf{w}}{\partial S}$

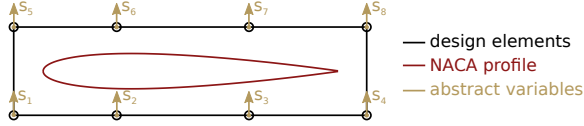


Figure 9.1: Setup used for the sensitivity verification. A simple NACA0012 profile is considered. The design element concept, as described in section 4.2 is applied. The profile is deformed using a cubic polynomial in x -direction and a linear polynomial in y -direction.

9.2 Verification of $\frac{\partial \mathbf{w}}{\partial s}$

9.2.1 Mach-sensitivity

For the body-fitted case, the verification of $\frac{d\mathbf{w}}{dM_\infty}$ is provided in figure 9.2 for Euler equations, figure 9.3 for full NSE and in figure 9.4 for NSE with an additional Spallart-Almores turbulence model. Additionally, a side by side comparison of the analytic results between all three equation types is also provided in figure 9.8 in order to ensure, that the additional viscous and turbulent terms actually account for a visible difference.

For the embedded case, we provide the verification of $\frac{d\mathbf{w}}{dM_\infty}$ in figure 9.5 for Euler equation, figure 9.6 for full NSE and in figure 9.7 for NSE equations with an additional Spallart-Almores turbulence model. Again, a side by side comparison of the analytic results between all three equation types is also provided in figure 9.9 in order to ensure that the additional viscous and turbulent terms actually account for a visible difference.

Verification $\frac{d\mathbf{w}}{dM_\infty}$ for Euler equations and a body-fitted framework

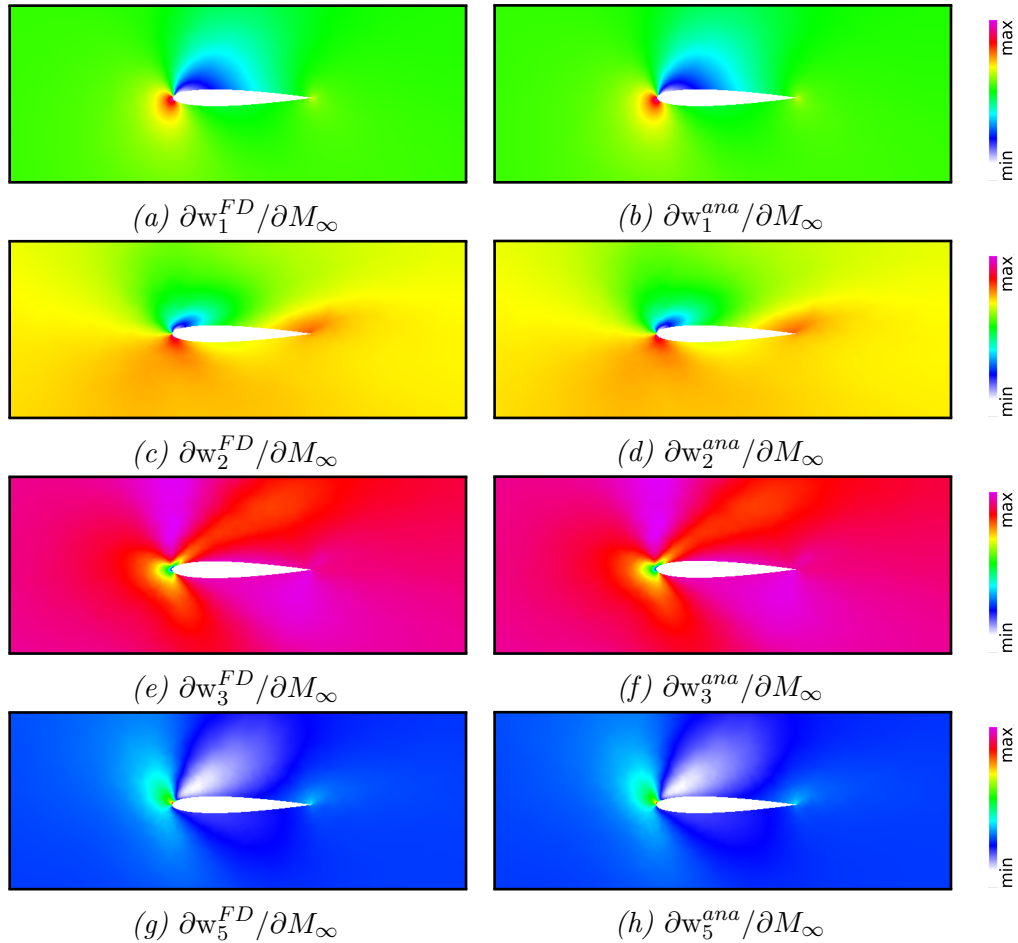


Figure 9.2: Verification of $\frac{d\mathbf{w}}{dM_\infty}$ for Euler equations in the body-fitted framework. The **FD** reference solution as described in chapter 9.1 is provided in the left column, the newly implemented analytic derivatives are visualized in the right column. **FD** and analytic solution are plotted using the same color-scheme.

Verification $\frac{d\mathbf{w}}{dM_\infty}$ for Laminar equations and a body-fitted framework

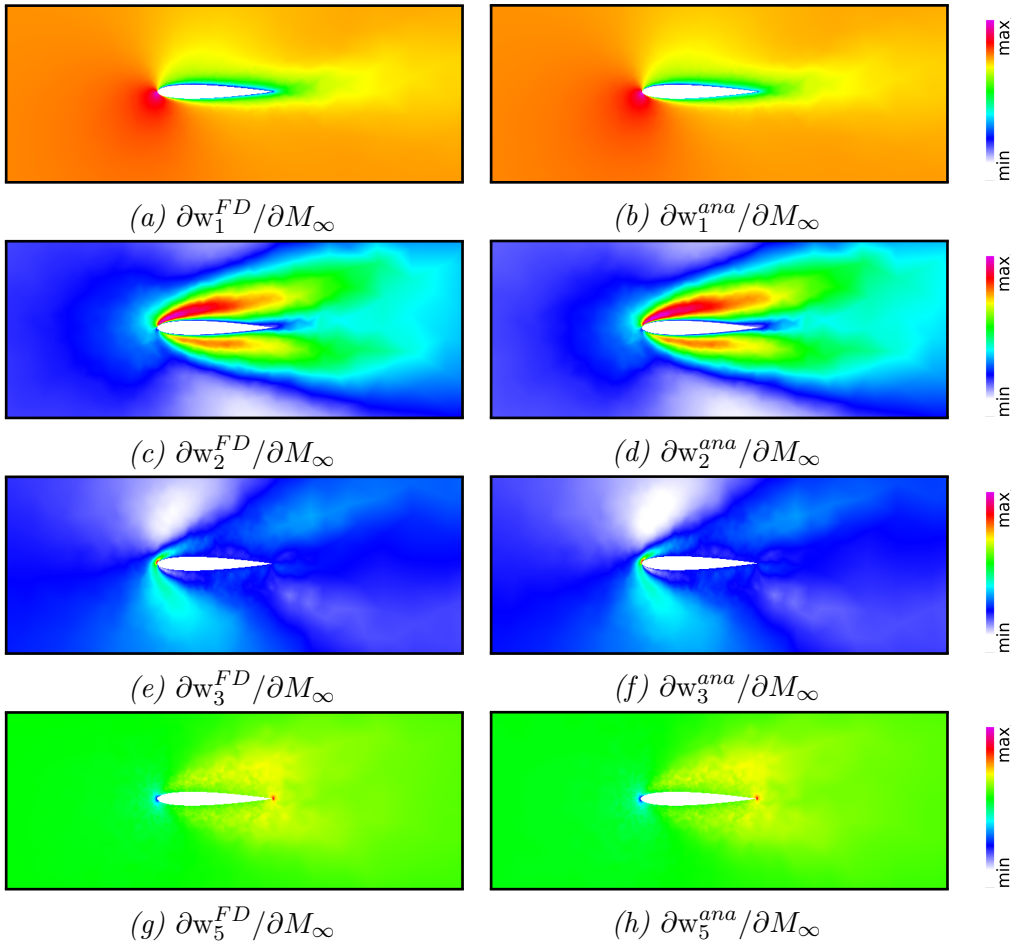


Figure 9.3: Verification of $\frac{d\mathbf{w}}{dM_\infty}$ for Laminar equations in the body-fitted framework. The **FD** reference solution as described in chapter 9.1 is provided in the left column, the newly implemented analytic derivatives are visualized in the right column. **FD** and analytic solution are plotted using the same color-scheme.

Verification $\frac{d\mathbf{w}}{dM_\infty}$ for RANS equations and a body-fitted framework

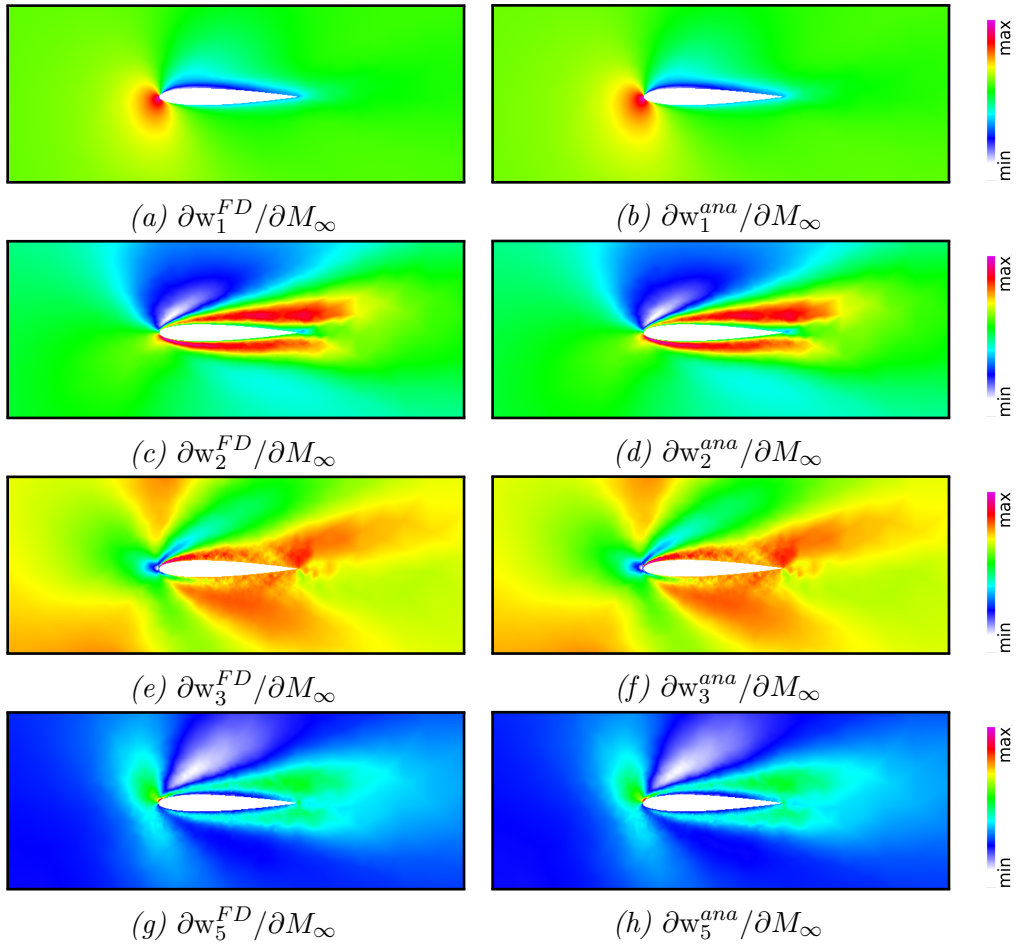


Figure 9.4: Verification of $\frac{d\mathbf{w}}{dM_\infty}$ for RANS equations in the body-fitted framework. The **FD** reference solution as described in chapter 9.1 is provided in the left column, the newly implemented analytic derivatives are visualized in the right column. **FD** and analytic solution are plotted using the same color-scheme.

Verification of $\frac{d\mathbf{w}}{dM_\infty}$ for Euler equations and a embedded framework

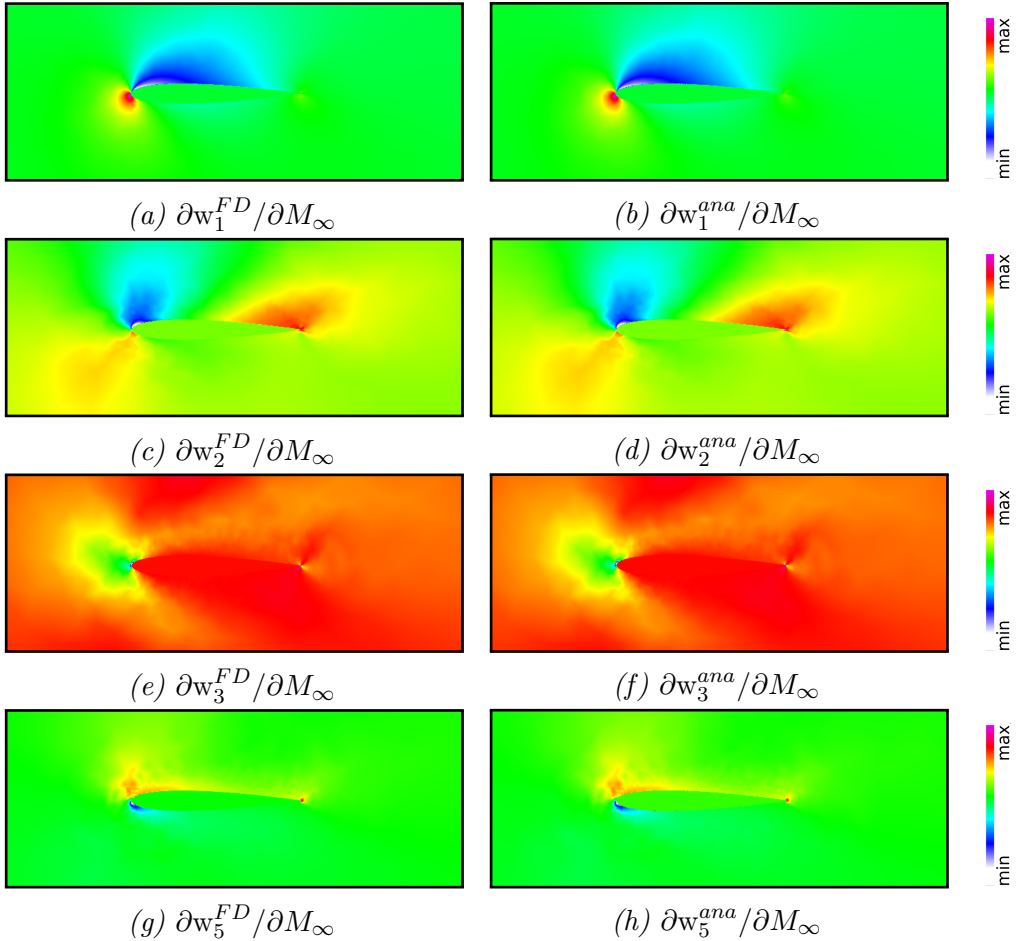


Figure 9.5: Verification of $\frac{d\mathbf{w}}{dM_\infty}$ for Euler equations in the embedded framework. The **FD** reference solution as described in chapter 9.1 is provided in the left column, the newly implemented analytic derivatives are visualized in the right column. **FD** and analytic solution are plotted using the same color-scheme.

Verification of $\frac{d\mathbf{w}}{dM_\infty}$ for Laminar equations and a embedded framework

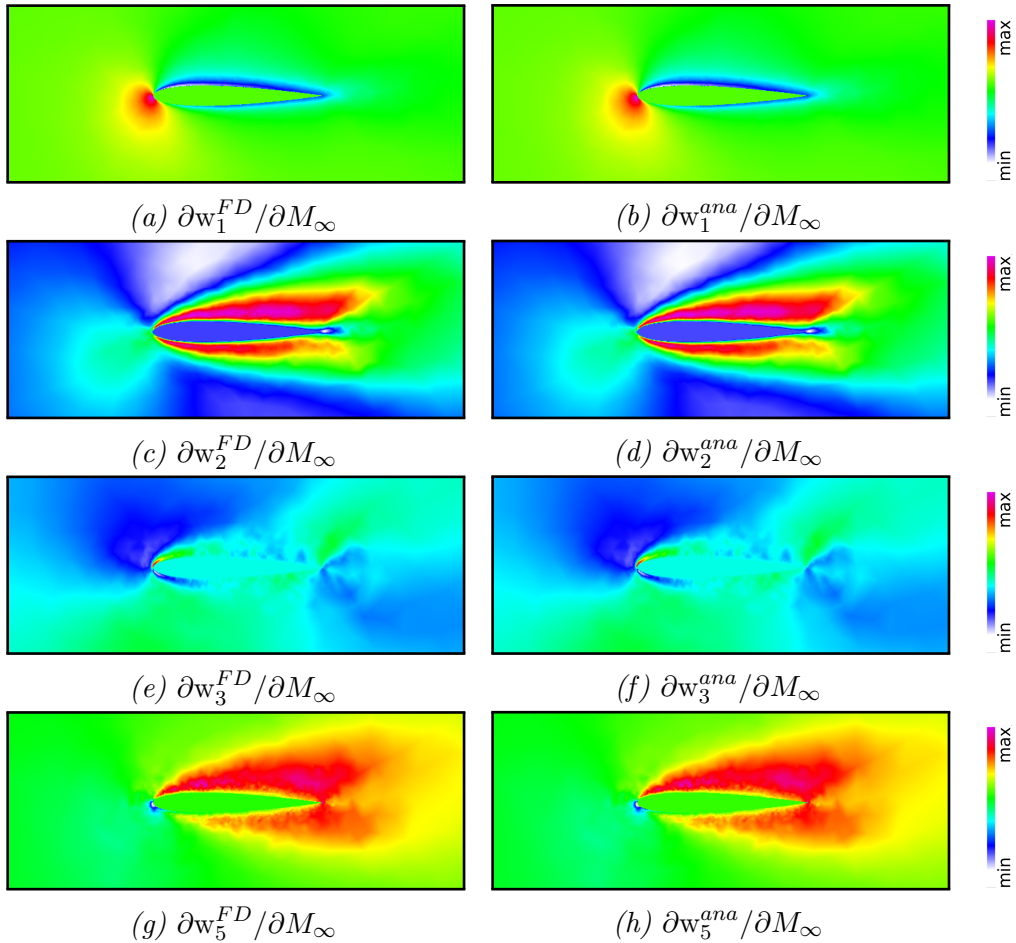


Figure 9.6: Verification of $\frac{d\mathbf{w}}{dM_\infty}$ for Laminar equations in the embedded framework. The **FD** reference solution as described in chapter 9.1 is provided in the left column, the newly implemented analytic derivatives are visualized in the right column. **FD** and analytic solution are plotted using the same color-scheme.

Verification of $\frac{d\mathbf{w}}{dM_\infty}$ for RANS equations and a embedded framework

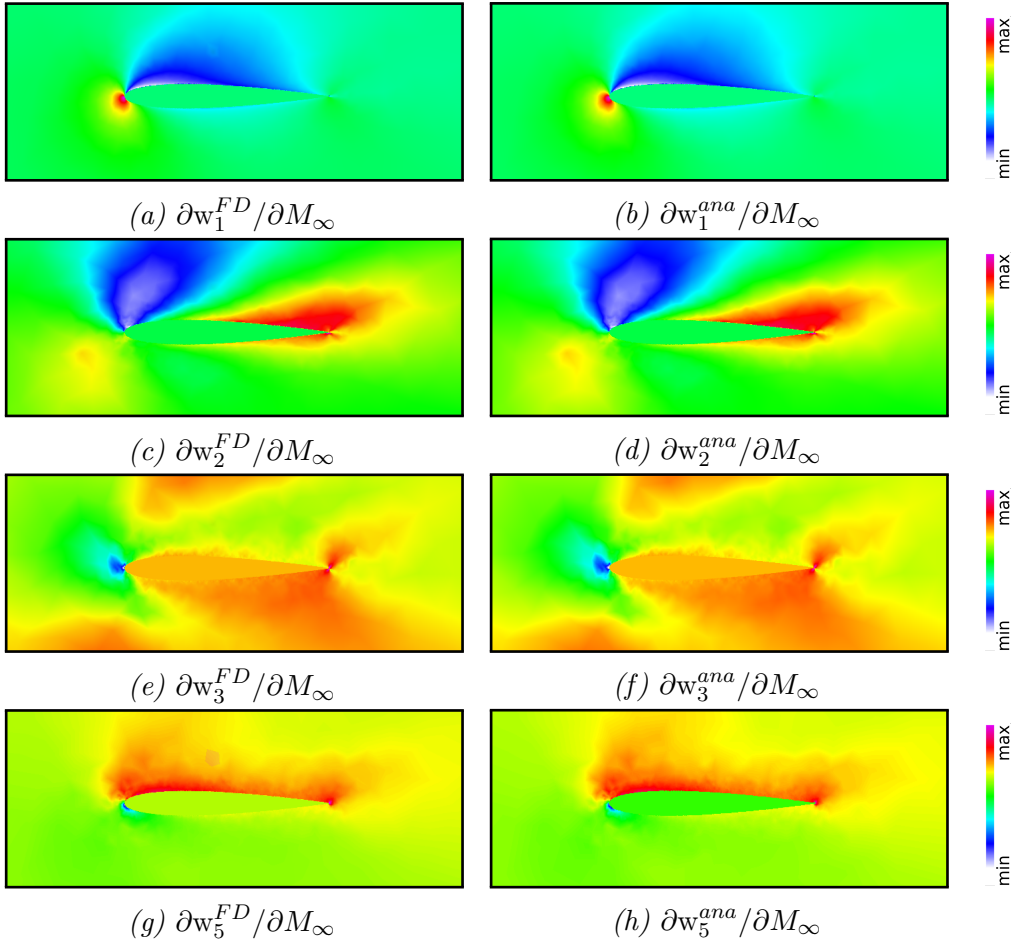


Figure 9.7: Verification of $\frac{d\mathbf{w}}{dM_\infty}$ for RANS equations in the embedded framework. The **FD** reference solution as described in chapter 9.1 is provided in the left column, the newly implemented analytic derivatives are visualized in the right column. **FD** and analytic solution are plotted using the same color-scheme.

Comparison of $\frac{d\mathbf{w}}{dM_\infty}$ in the body-fitted framework for all 3 equation types

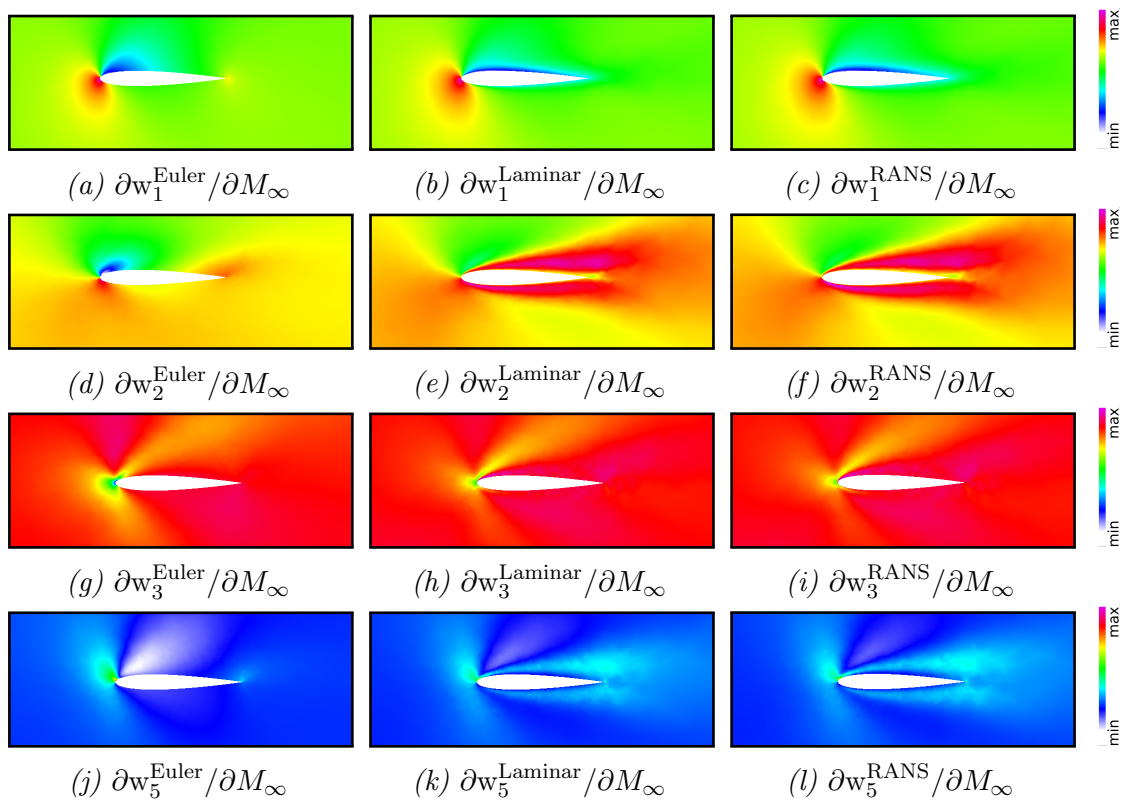


Figure 9.8: Comparison of analytic $\frac{d\mathbf{w}}{dM_\infty}$ for Euler equations(left column), laminar **NSE** equations (center column) and **NSE** equations with turbulence models (right column) in the body-fitted framework.

Comparison of $\frac{d\mathbf{w}}{dM_\infty}$ in the embedded framework for all 3 equation types

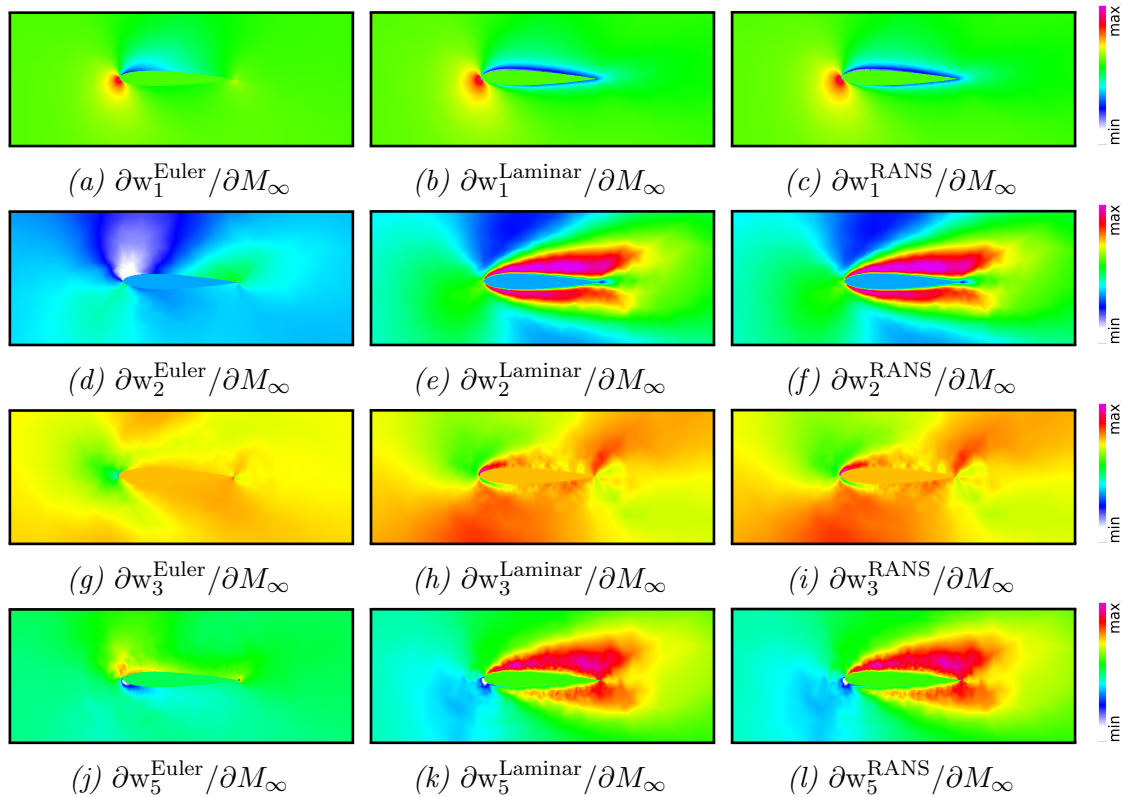
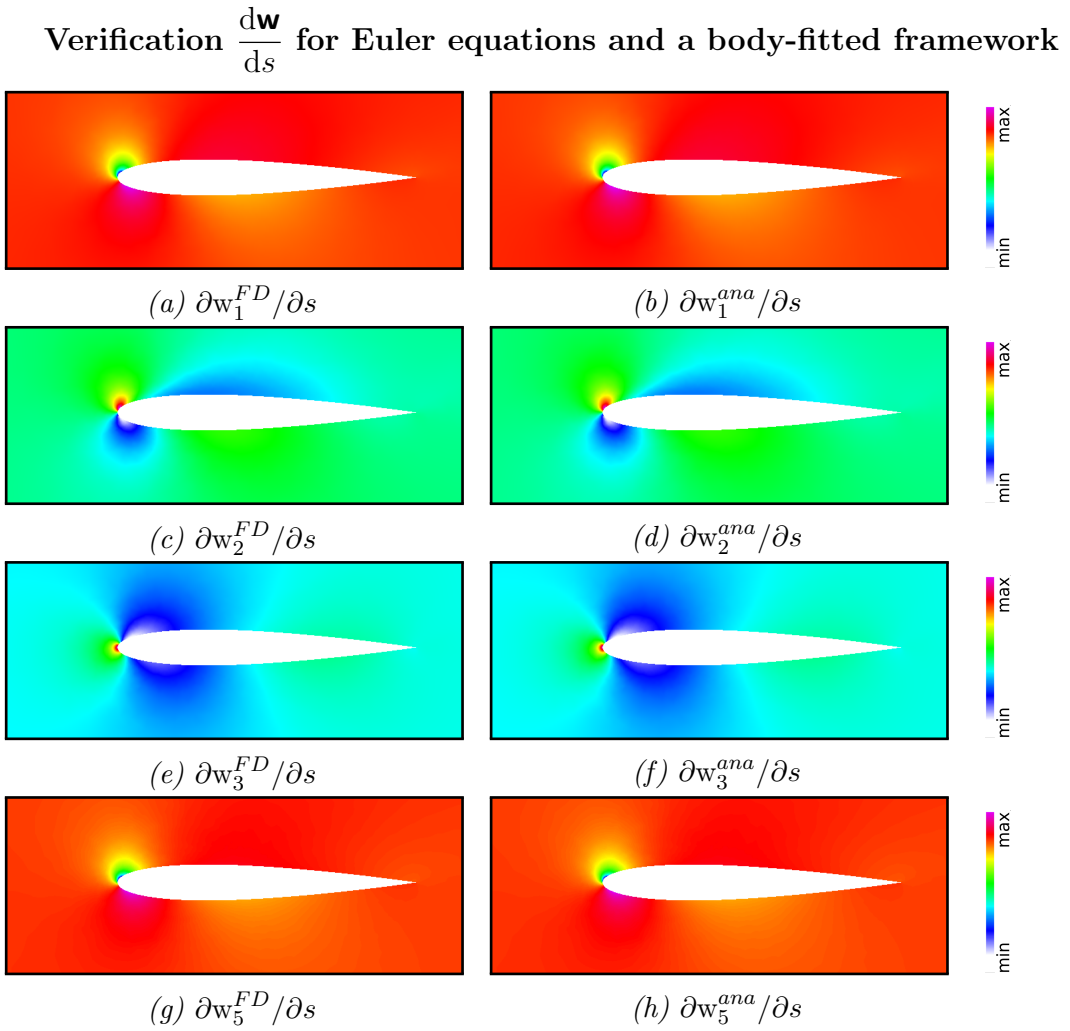


Figure 9.9: Comparison of analytic $\frac{d\mathbf{w}}{dM_\infty}$ for Euler equations(left column), laminar NSE equations (center column) and NSE equations with turbulence models (right column) in the embedded framework.

9.2.2 Shape-sensitivity

The verification of $\frac{d\mathbf{w}}{ds}$ for body-fitted simulations is provided in figure 9.10 for Euler equation, figure 9.11 for full NSE and in figure 9.12 for NSE with an additional Spallart-Almaraes turbulence model. Additionally, a side by side comparison of the analytic results between all three equation types is also provided in figure 9.16 in order to ensure that the additional viscous and turbulent terms actually account for a visible difference.

For the embedded case, we provide the verification of $\frac{d\mathbf{w}}{ds}$ in figure 9.13 for Euler equation, figure 9.14 for full NSE and in figure 9.15 for NSE with an additional Spallart-Almaraes turbulence model. Again, a side by side comparison of the analytic results between all three equation types is also provided in figure 9.17 in order to ensure that the additional viscous and turbulent terms actually account for a visible difference.



*Figure 9.10: Verification of $\frac{d\mathbf{w}}{ds}$ for Euler equations in the body-fitted framework. The **FD** reference solution as described in chapter 9.1 is provided in the left column, the newly implemented analytic derivatives are visualized in the right column. **FD** and analytic solution are plotted using the same color-scheme.*

Verification $\frac{d\mathbf{w}}{ds}$ for Laminar equations and a body-fitted framework

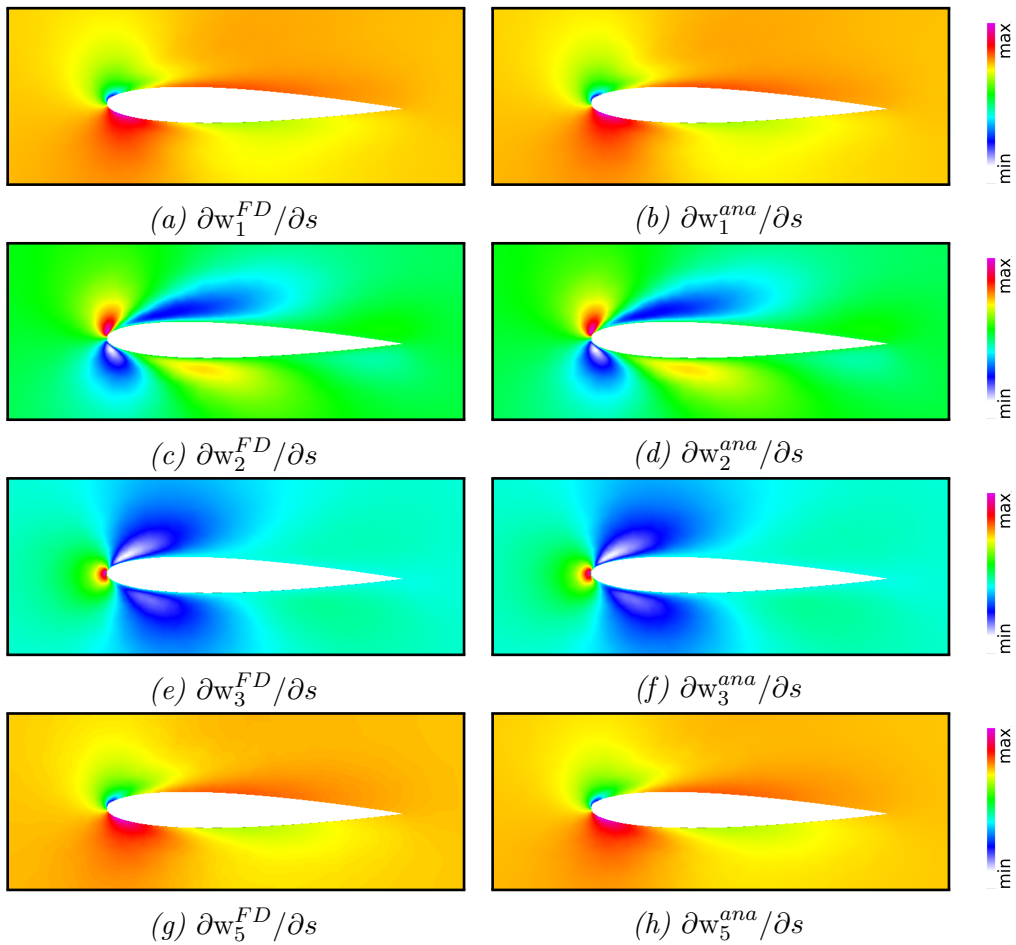


Figure 9.11: Verification of $\frac{d\mathbf{w}}{ds}$ for Laminar equations in the body-fitted framework. The **FD** reference solution as described in chapter 9.1 is provided in the left column, the newly implemented analytic derivatives are visualized in the right column. **FD** and analytic solution are plotted using the same color-scheme.

Verification $\frac{d\mathbf{w}}{ds}$ for RANS equations and a body-fitted framework

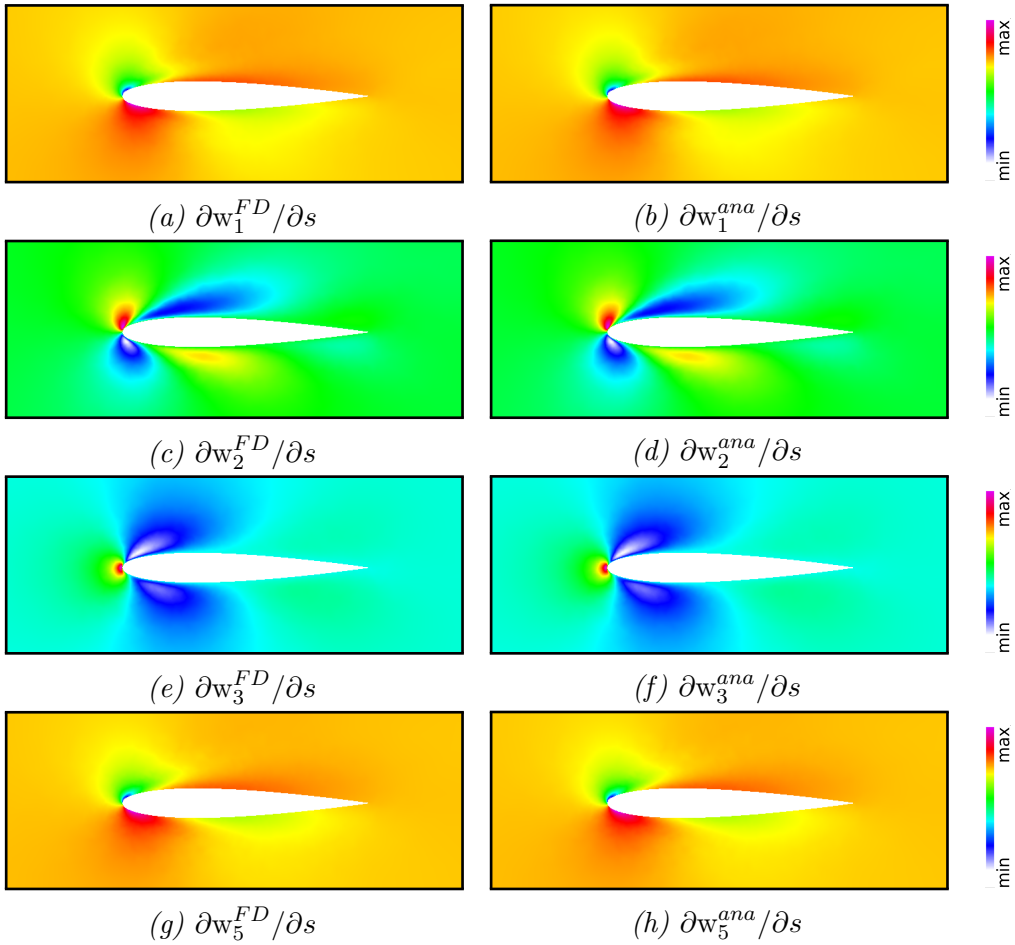


Figure 9.12: Verification of $\frac{d\mathbf{w}}{ds}$ for RANS equations in the body-fitted framework. The **FD** reference solution as described in chapter 9.1 is provided in the left column, the newly implemented analytic derivatives are visualized in the right column. **FD** and analytic solution are plotted using the same color-scheme.

Verification $\frac{d\mathbf{w}}{ds}$ for Euler equations and a embedded framework

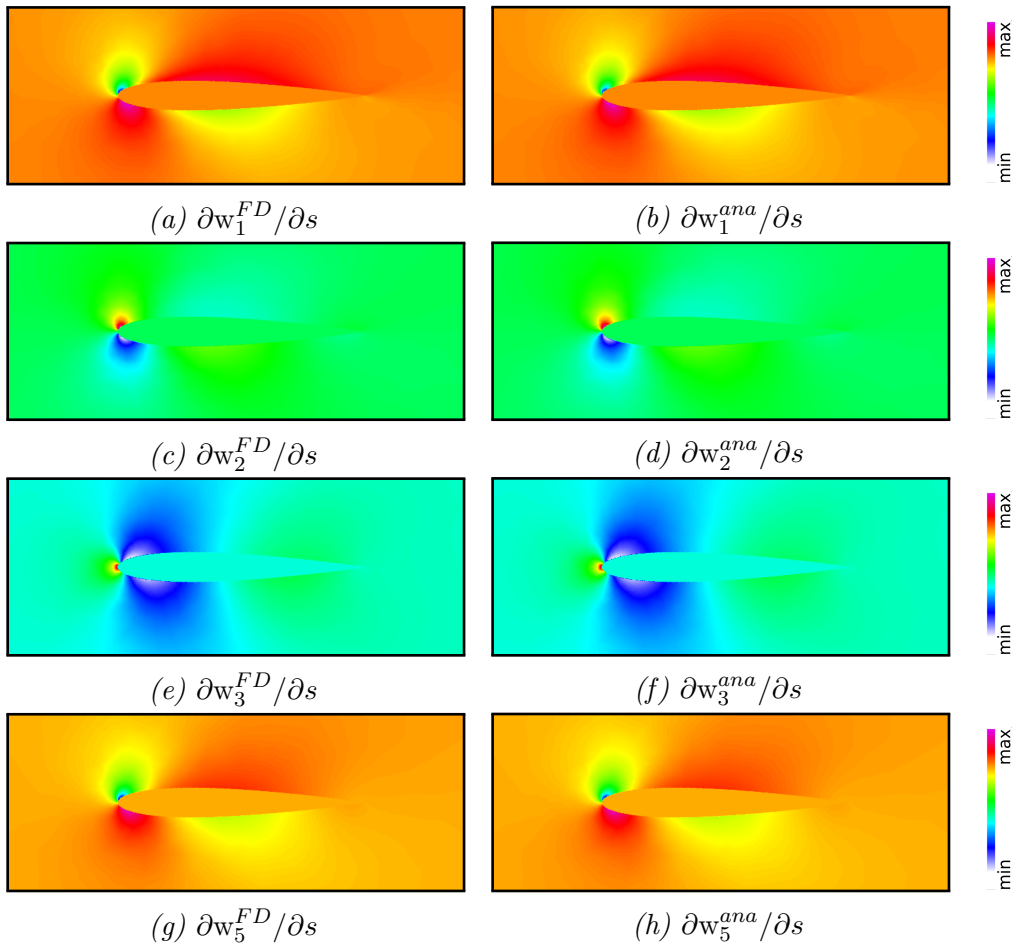


Figure 9.13: Verification of $\frac{d\mathbf{w}}{ds}$ for Euler equations in the embedded framework. The FD reference solution as described in chapter 9.1 is provided in the left column, the newly implemented analytic derivatives are visualized in the right column. FD and analytic solution are plotted using the same color-scheme.

Verification $\frac{d\mathbf{w}}{ds}$ for Laminar equations and a embedded framework

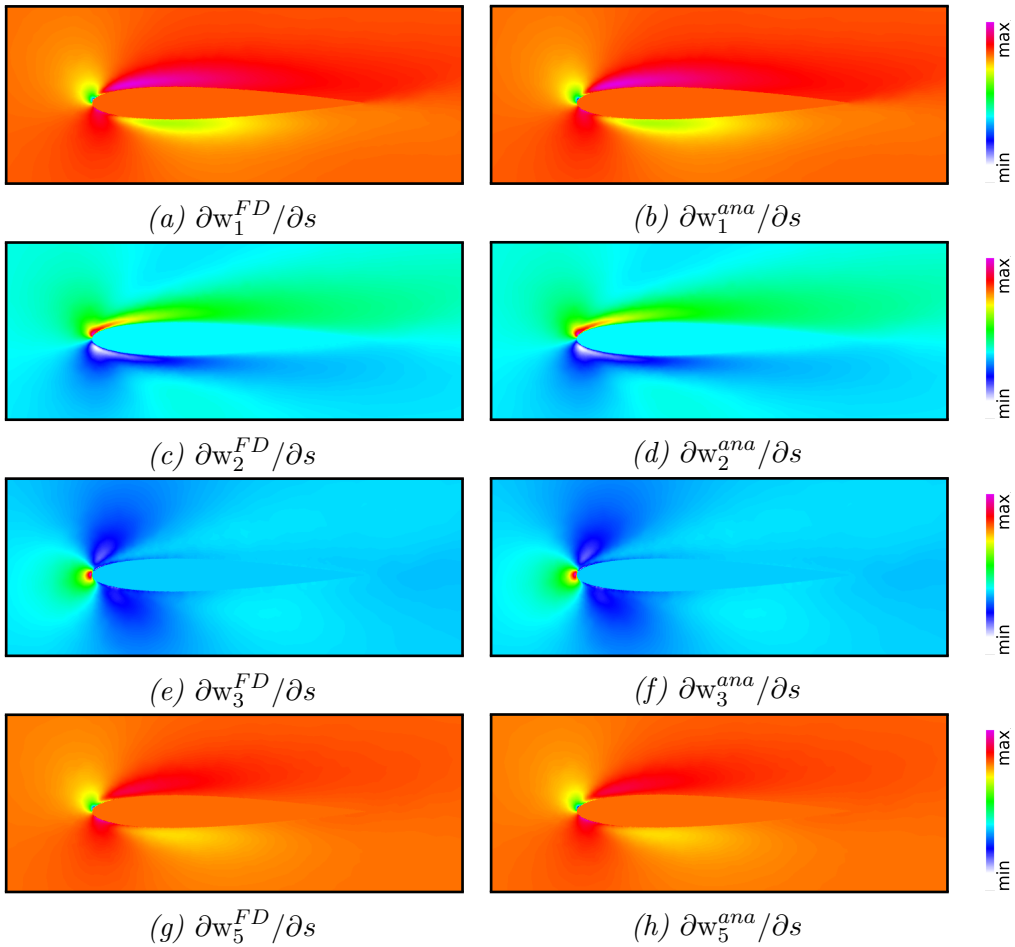


Figure 9.14: Verification of $\frac{d\mathbf{w}}{ds}$ for Laminar equations in the embedded framework. The FD reference solution as described in chapter 9.1 is provided in the left column, the newly implemented analytic derivatives are visualized in the right column. FD and analytic solution are plotted using the same color-scheme.

Verification $\frac{d\mathbf{w}}{ds}$ for RANS equations and a embedded framework

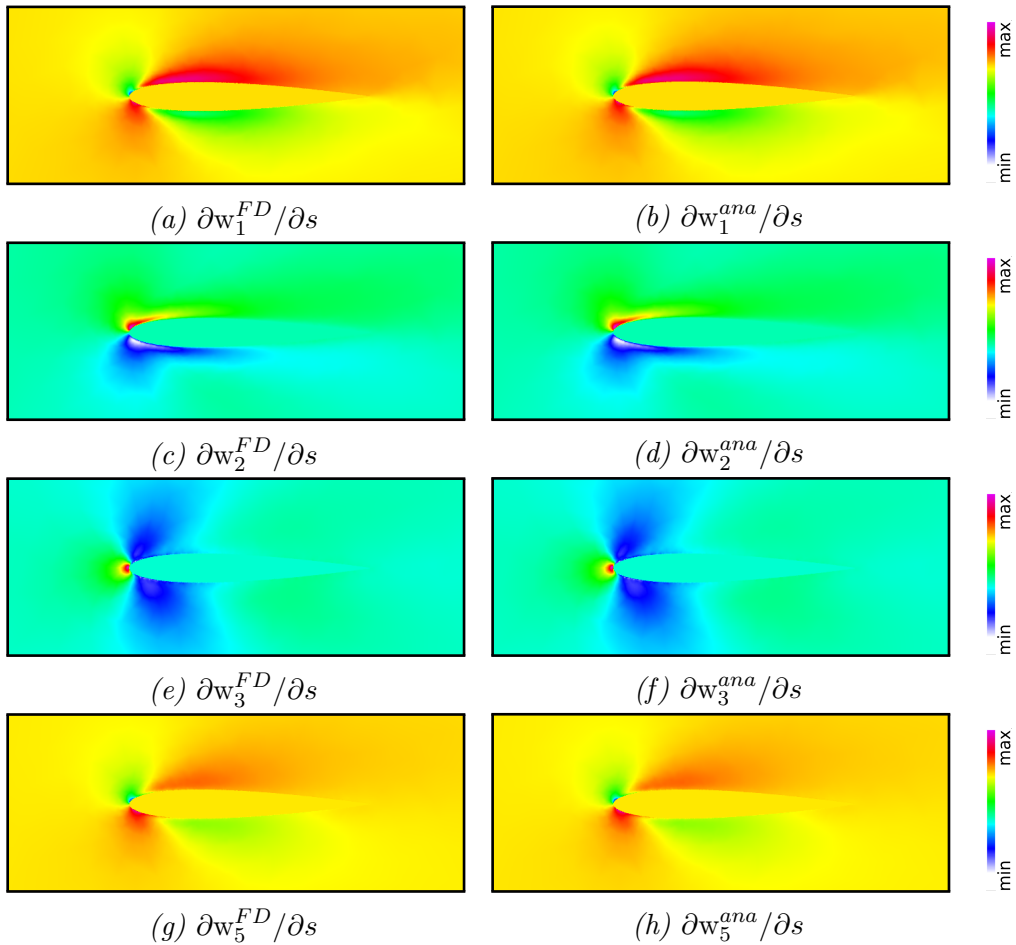


Figure 9.15: Verification of $\frac{d\mathbf{w}}{ds}$ for RANS equations in the embedded framework. The **FD** reference solution as described in chapter 9.1 is provided in the left column, the newly implemented analytic derivatives are visualized in the right column. **FD** and analytic solution are plotted using the same color-scheme.

Comparison of $\frac{d\mathbf{w}}{ds}$ in the body-fitted framework for all 3 equation types

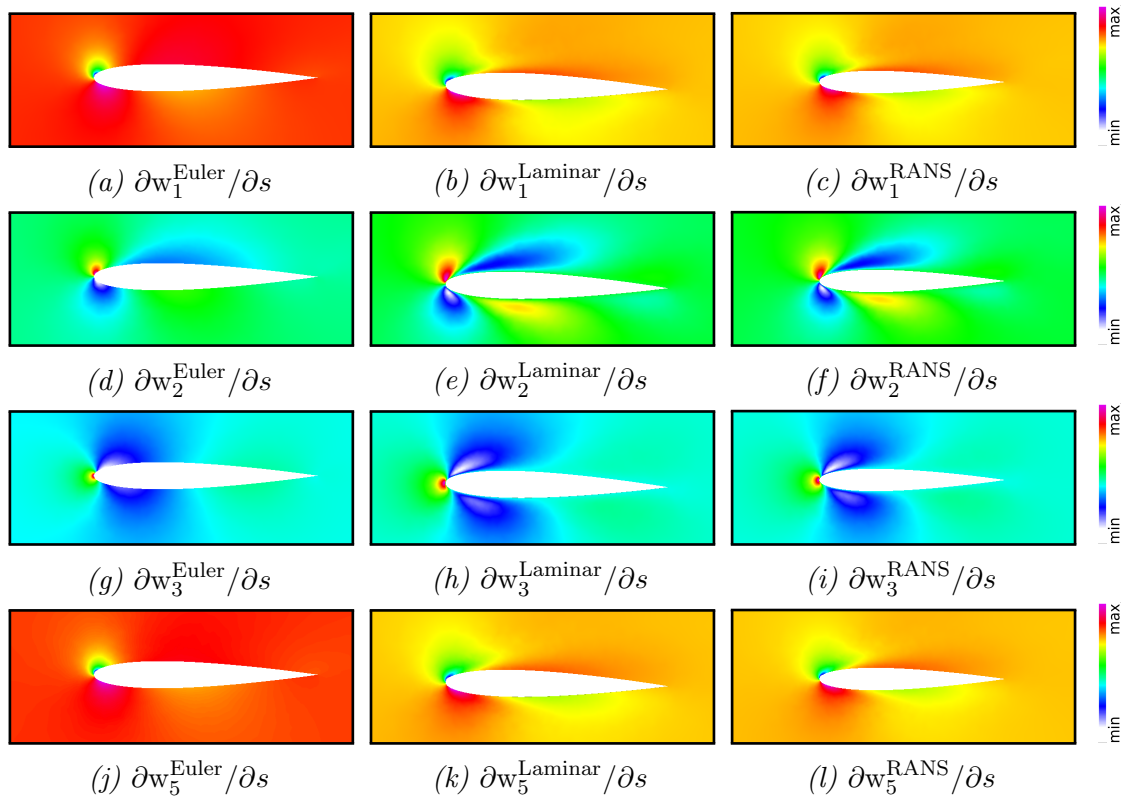


Figure 9.16: Comparison of analytic $\frac{d\mathbf{w}}{dM_\infty}$ for Euler equations (left column), laminar NSE equations (center column) and NSE equations with turbulence models (right column) in the body-fitted framework.

Comparison of $\frac{d\mathbf{w}}{ds}$ in the embedded framework for all 3 equation types

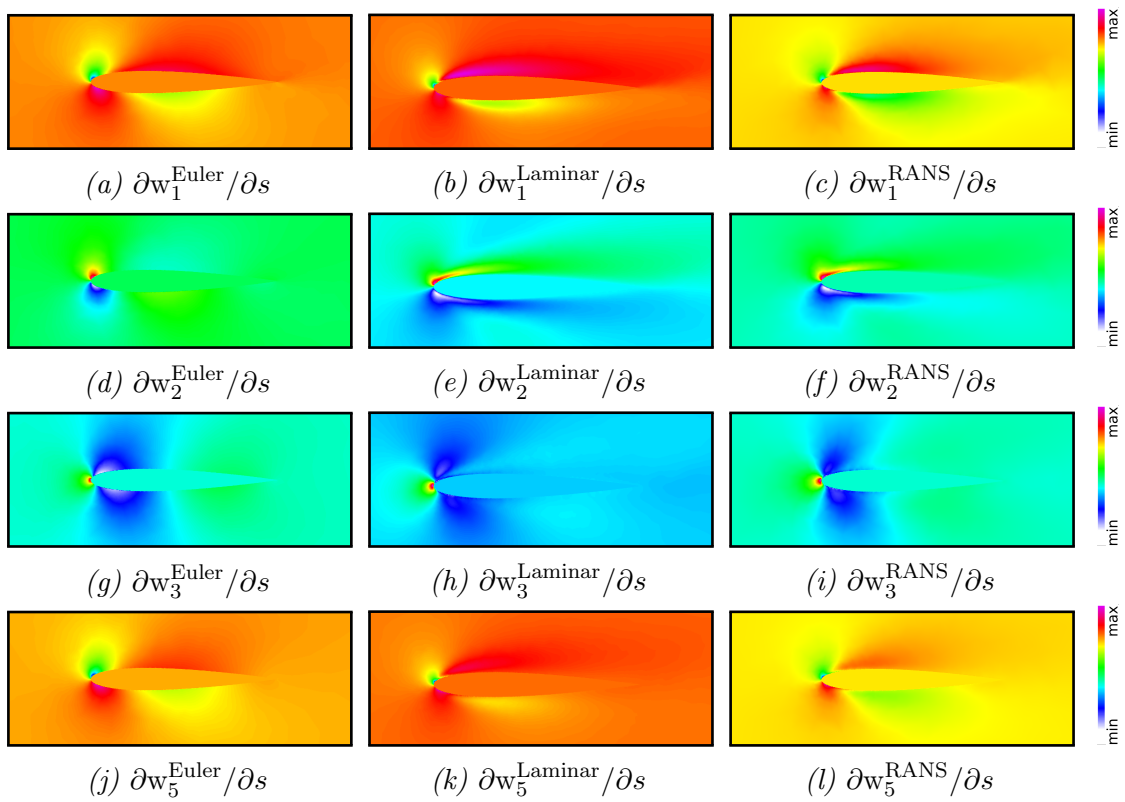


Figure 9.17: Comparison of analytic $\frac{d\mathbf{w}}{dM_\infty}$ for Euler equations(left column), laminar **NSE** equations (center column) and **NSE** equations with turbulence models (right column) in the embedded framework.

9.3 Verification of Lift and Drag results

This section deals with the verification of the actual lift and drag sensitivities, thus the final objective functions derivatives. Those sensitivities are more cumbersome to obtain than the sensitivities of the state vector $\frac{\partial \mathbf{w}}{\partial s}$, provided in section 9.2, particularly for the embedded case or for the case of shape-sensitivities, where the integration area itself is derived.

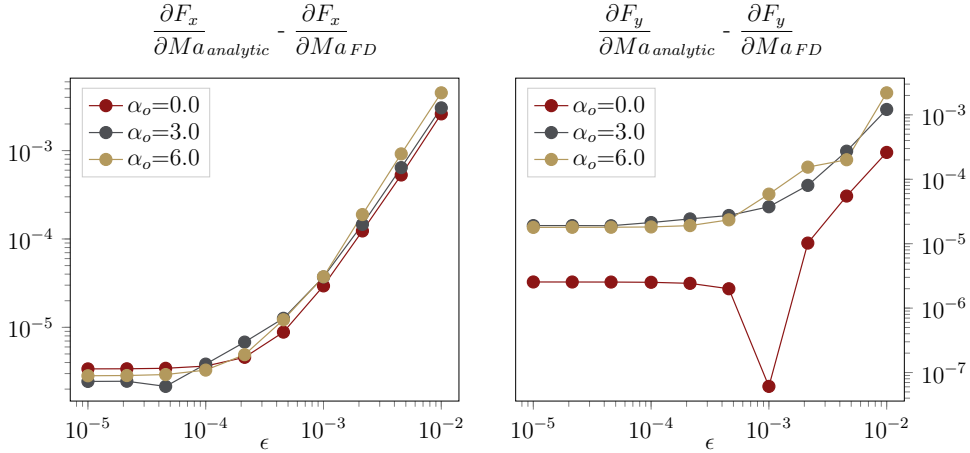
Lift and Drag sensitivity: body-fitted Euler equations


Figure 9.18: The graph shows the relative error between the Lift and Drag Mach-sensitivities obtained by **FD** of two steady states, compared to the Mach-sensitivity obtained by analytic direct evaluation. L_x denotes the Drag, L_y denotes the lift. Please note that a **FD** Jacobian has been used here, which of course introduces an approximation error. Furthermore, the finite precision of the obtained steady states is another error source. This explains why the error levels off. For all practical optimization purposes, the obtained accuracy is more than enough.

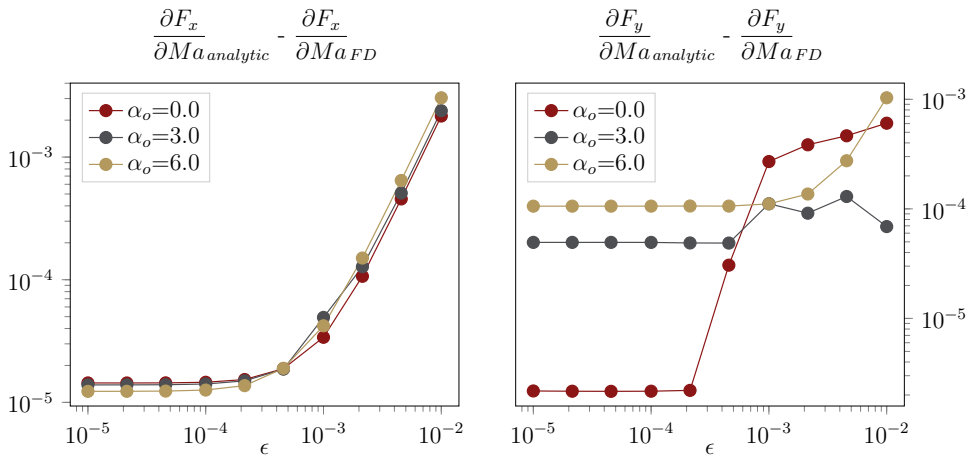
Lift and Drag sensitivity: body-fitted Laminar equations


Figure 9.19: The graph shows the relative error between the Lift and Drag Mach-sensitivities obtained by **FD** of two steady states, compared to the Mach-sensitivity obtained by analytic direct evaluation. L_x denotes the Drag, L_y denotes the lift. Please note that a **FD** Jacobian has been used here, which of course introduces an approximation error. Furthermore, the finite precision of the obtained steady states is another error source. This explains why the error levels off. For all practical optimization purposes, the obtained accuracy is more than enough.

9.3. VERIFICATION OF LIFT AND DRAG RESULTS

Lift and Drag sensitivity: body-fitted RANS equations

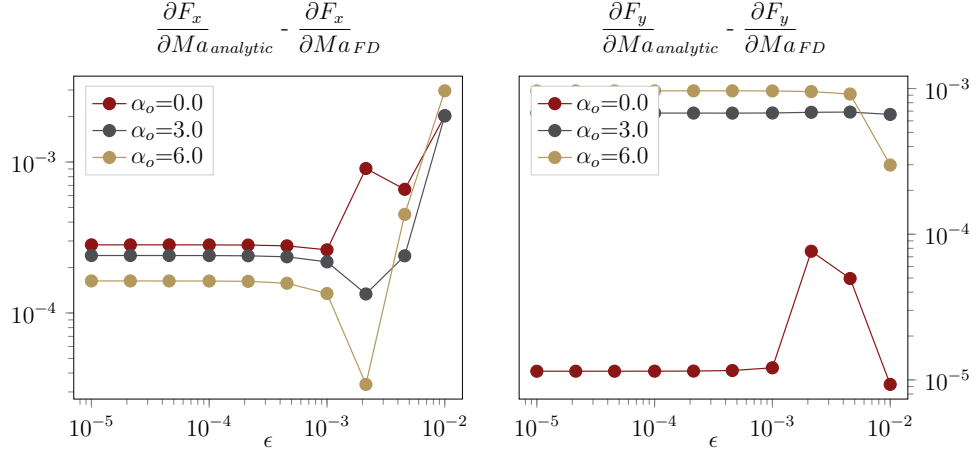


Figure 9.20: The graph shows the relative error between the Lift and Drag Mach-sensitivities obtained by FD of two steady states, compared to the Mach-sensitivity obtained by analytic direct evaluation. L_x denotes the Drag, L_y denotes the lift. Please note that a FD Jacobian has been used here, which of course introduces an approximation error. Furthermore, the finite precision of the obtained steady states is another error source. This explains why the error levels off. For all practical optimization purposes, the obtained accuracy is more than enough.

Lift and Drag sensitivity: embedded Euler equations

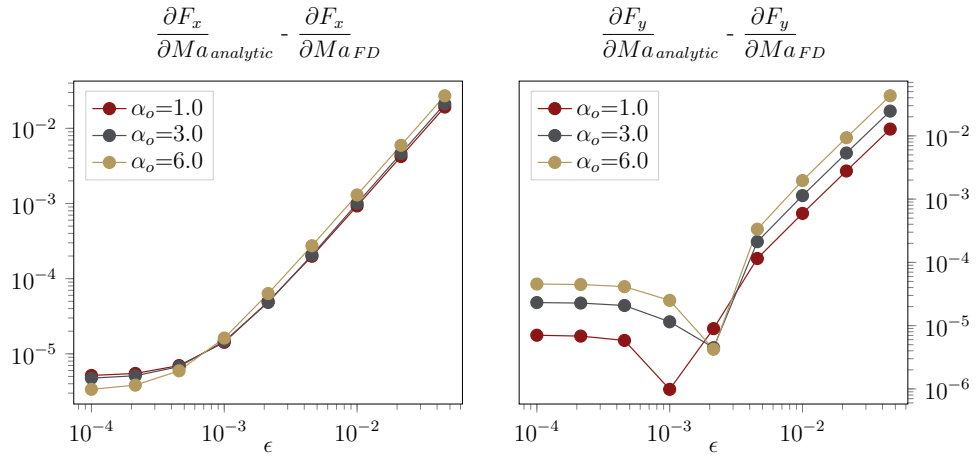


Figure 9.21: The graph shows the relative error between the Lift and Drag Mach-sensitivities obtained by FD of two steady states, compared to the Mach-sensitivity obtained by analytic direct evaluation. L_x denotes the Drag, L_y denotes the lift. Please note that a FD Jacobian has been used here, which of course introduces an approximation error. Furthermore, the finite precision of the obtained steady states is another error source. This explains why the error levels off. For all practical optimization purposes, the obtained accuracy is more than enough.

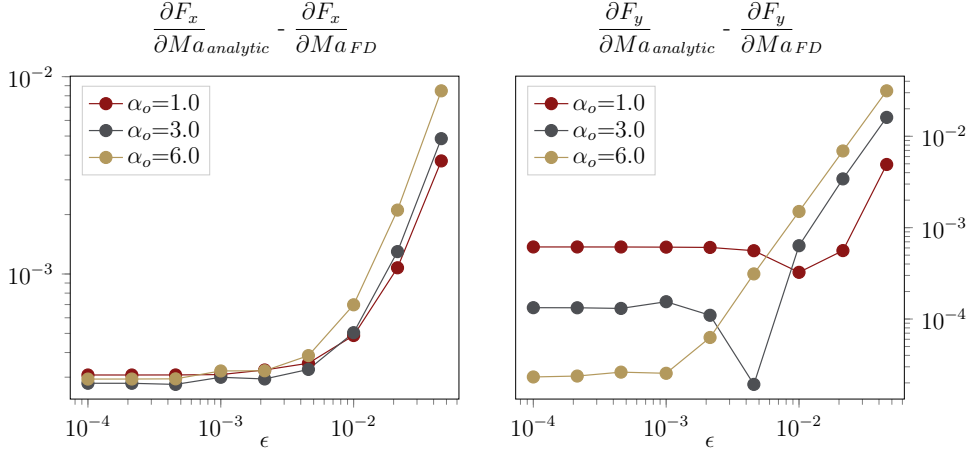
Lift and Drag sensitivity: embedded Laminar equations


Figure 9.22: The graph shows the relative error between the Lift and Drag Mach-sensitivities obtained by **FD** of two steady states, compared to the Mach-sensitivity obtained by analytic direct evaluation. L_x denotes the Drag, L_y denotes the lift. Please note that a **FD** Jacobian has been used here, which of course introduces an approximation error. Furthermore, the finite precision of the obtained steady states is another error source. This explains why the error levels off. For all practical optimization purposes, the obtained accuracy is more than enough.

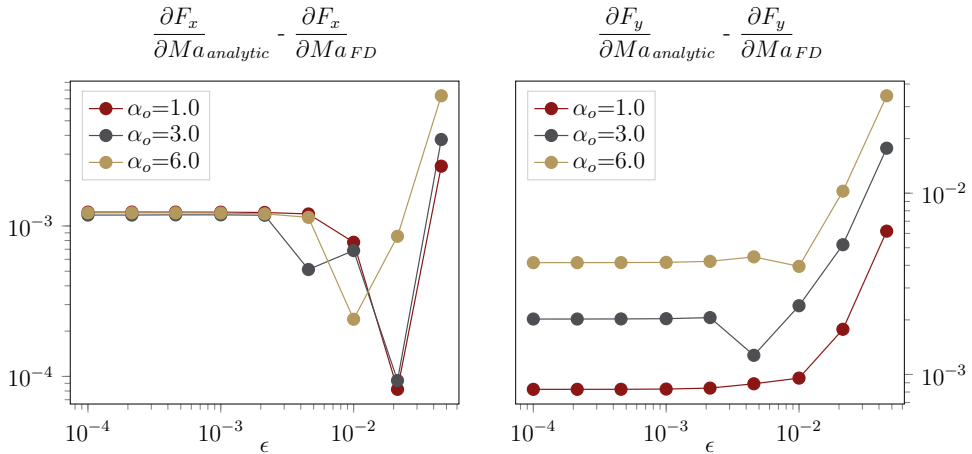
Lift and Drag sensitivity: embedded RANS equations


Figure 9.23: The graph shows the relative error between the Lift and Drag Mach-sensitivities obtained by **FD** of two steady states, compared to the Mach-sensitivity obtained by analytic direct evaluation. L_x denotes the Drag, L_y denotes the lift. Please note that a **FD** Jacobian has been used here, which of course introduces an approximation error. Furthermore, the finite precision of the obtained steady states is another error source. This explains why the error levels off. For all practical optimization purposes, the obtained accuracy is more than enough.

Chapter 10

Examples

Contents

10.1 LDR shape-optimization of a NACA0012 airfoil	97
10.1.1 Setup	97
10.1.2 Results	98
10.2 Multi-element airfoil with large kinematics	98
10.2.1 Setup	99
10.2.2 Results	99

This section is denoted to simple examples of the newly implemented analytic sensitivity framework. Due to a limited time available, we restricted our considerations to simple 2D problems. Particularly, an optimization on the NACA0012 profile, as already described in figure 9.1, is presented in section 10.1.

A slightly more cumbersome example, that nicely portrays the advantages of the embedded sensitivity framework is then provided in section 10.2. Here, the flap and slats configuration of an airfoil is maximized. This requires large deformations and would not be possible with the body-fitted sensitivity framework.

10.1 **LDR shape-optimization of a NACA0012 airfoil**

We consider the optimization of a NACA0012 airfoil for an angle of attack of $\alpha = 0.0^\circ$ and a Mach number of 0.3.

10.1.1 **Setup**

The setup has already been described in figure 9.1. The shape is described using the design variable concept (see section 4.2) with 8 abstract variables. In this particular example, the lower, front design variable has been fixed in order to prevent rigid body motions.

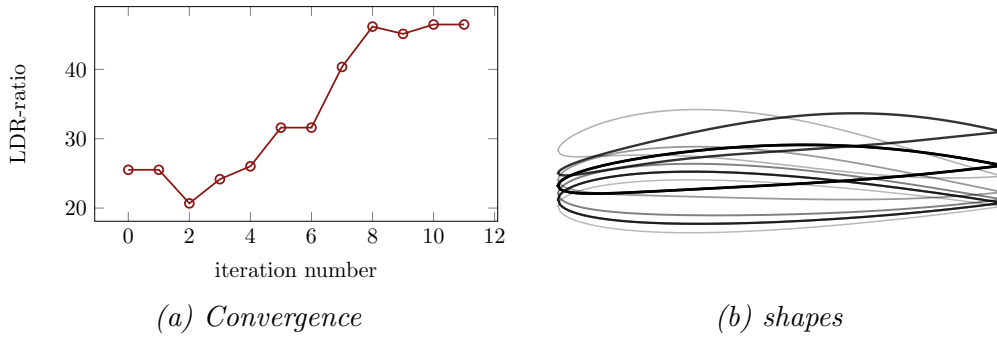


Figure 10.1: Convergence of the LDR during the optimization. A BFGS algorithm has been used for optimization. The left figure shows the convergence of the lift-to-drag ratio, the right figure displays the different airfoil shapes during the optimization process.

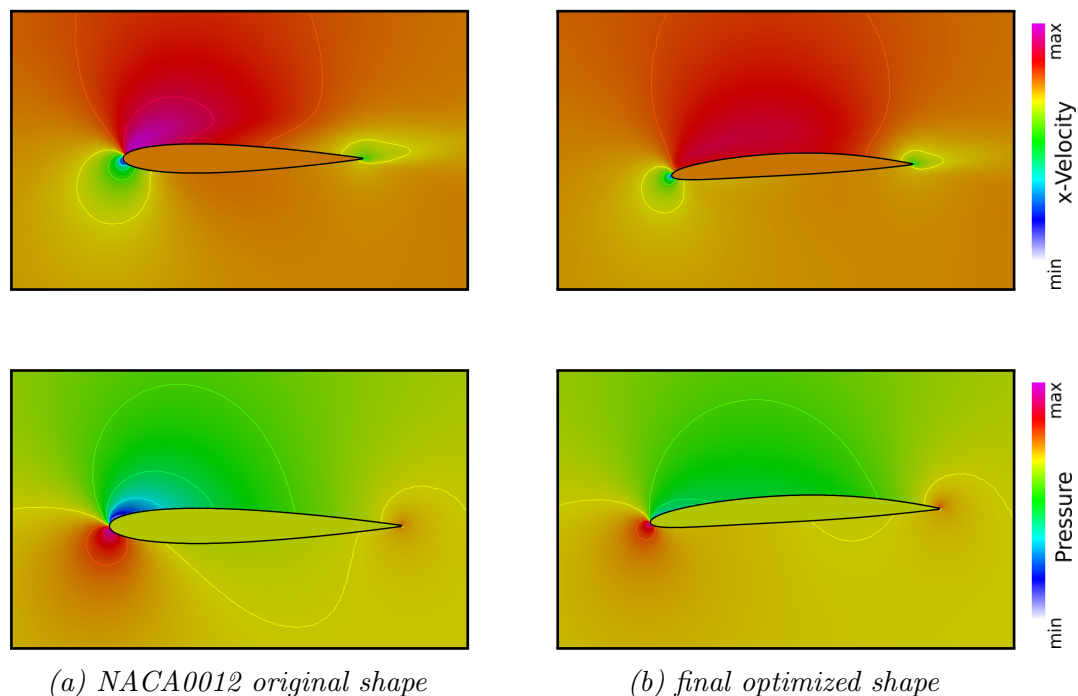


Figure 10.2: Lift over Drag optimization of a 2D airfoil in the embedded framework. The design element configuration of the embedded surface is depicted in Figure 9.1.

10.1.2 Results

The example has been run meshed with ~ 1000000 nodes and running on 60 compute cores. All forces have been evaluated on the discrete embedded surface. Both the initial and the final, converged shape are provided in figure 10.2.

10.2 Multi-element airfoil with large kinematics

The second example aims at pointing out the superiority of the embedded approach over the body-fitted approach when it comes to shape optimization. Due to the large

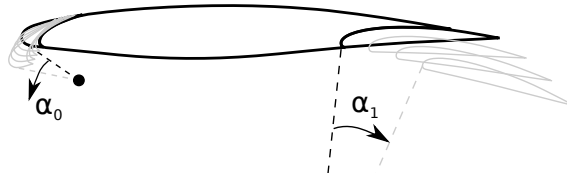


Figure 10.3: Setup for the multi-element example. A 3 element airfoil is considered. The motion of the front of back element is being described via a simple rotation. This is done on purpose to keep the parameter-space low-dimensional. This example would not be possible in the body-fitted framework.

motions involved, this example would not have been possible with a body-fitted framework. The setup is described in section 10.2.1 and the results are presented in section 10.2.2.

10.2.1 Setup

The setup is described in figure 10.3. The airfoil consists of 3 separate parts, where the front and back can perform large motions. Each motion is described by a single parameter (rotatory movement). This way, the parameter space has been kept low-dimensional, which enabled us to sample the whole space, thereby verifying that the optimizer indeed finds the correct solution

10.2.2 Results

The objective of this simulation was the minimization of the lift over drag ratio. We prescribed both minimum lift and maximum drag constraints. The optimization was then performed using an Sequential Least Squares Programming (**SLSQP**) algorithm. In order to verify the results of the optimizer, we performed a 30×30 sampling of the parameter space. The lift and drag results are visualized in figure 10.4 and the lift over drag ration is printed over the parameter space in figure 10.5.

CHAPTER 10. EXAMPLES

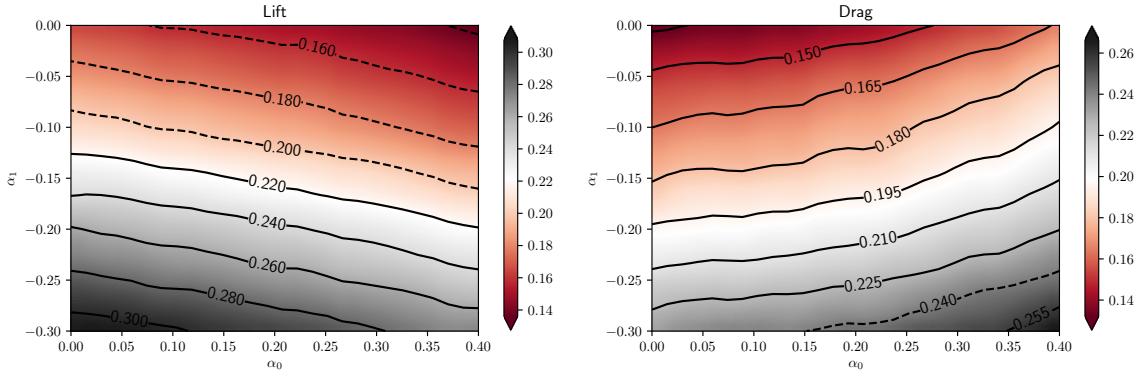


Figure 10.4: Lift(left figure)- and drag(right figure)- results plotted over the parameter space spanned by α_0 and α_1 . ISO-lines that don't fulfill the minimum lift or maximum drag requirements are plotted in dashed lines. An optimum is searched in the remaining parameter space. The optimum found is plotted in figure 10.5

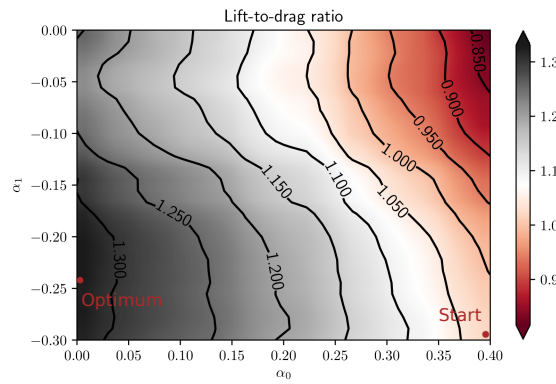


Figure 10.5: Lift over Drag Ratio (LDR) over the parameter space for the example presented in figure 10.3. α_0 is plotted over the horizontal axis, α_1 over the vertical axis. There is no local maximum, instead the optimum is on the border of the parameter space. Both the starting configuration as well as the optimum found by the optimizer are plotted. The optimization has been performed using SciPy:L-BFGS-B.

Chapter 11

Conclusions

Contents

11.1 Summary	101
11.2 Outlook	102

11.1 Summary

This thesis began with a short motivation on why analytic sensitivity analysis is desirable and what applications in the context of optimization look like. We then provided a quick overview on the basic equations of fluid mechanics in section 1. Particularly, we put emphasis on important issues for the subsequent chapters, like Eulerian and Lagrangian view or turbulence models. The Finite Volumes (**FV**) method has then been introduced in section 2 as a mean of solving those equations numerically. This chapter followed closely the approach used in AERO-F[9], the flow solver at the Farhat Research Group (**FRG**) at Stanford University. This code has a comprehensive Immersed Boundary Method (**IBM**) framework: Finite Volume Method with exact two-phase Riemann Integrals (**FIVER**)[16]. While not restricted to it, this thesis largely dealt with this framework, the body-fitted case being regarded as a subset.

The thesis then shifted towards motivating Sensitivity Analysis (**SA**) by introducing the basics of aerodynamic shape optimizations in section 4 more precisely, gradient-based optimization. The derivation of these gradients in an analytic manner has been the main focus of this thesis and was introduced in section 5 for fluid equations, and section 7 for coupled fluid-structure interaction problems.

The theory covered both, the direct and the adjoint method, the implementation was focused on implementing the direct method first.

Details on how to evaluate a number of particularly interesting derivatives have been provided in section 6.

The implemented analytic derivatives have undergone thorough verification in section 9 before they have been applied to simple demonstrative examples in section 10.

11.2 Outlook

We have successfully demonstrated the feasibility of analytic sensitivity analysis with an Immersed Boundary Method (**IBM**) and fully viscous and turbulent flows. In combination with the Finite Volume Method with exact two-phase Riemann Integrals (**FIVER**), this offers a very promising framework for aerodynamic and aeroelastic shape optimization. By utilizing the **IBM** we have been able to optimize complex and greatly changing geometries, that would not have been possible in a body-fitted framework, or would at least have required some sort of re-meshing algorithm. The examples delivered promising results for both inviscid and viscous flows.

So far, all examples and verifications have been run on first-order simulations. Future effort should therefore focus on the validation of the implemented framework on higher order schemes.

Overall, the developed framework represents a powerful and comprehensive tool for gradient-based aerodynamic shape optimization. The **IBM** framework provides unprecedented flexibility with regards to the geometry while greatly improving both the computational efficiency as well as stability compared to **FD** gradients.

Bibliography

- [1] Joseph-Frédéric Bonnans, Gilbert Jean Charles, Lemarechal Claude, and Sagastizábal Claudia A. Numerical optimization: Theoretical and practical aspects. *Numerical Optimization: Theoretical and Practical Aspects*, pages 1–494, 2006.
- [2] Charles R. Doering and J. D. Gibbon. *Applied analysis of the Navier-Stokes equations*. Cambridge University Press, Cambridge, 1995.
- [3] C. Farhat, C. Degand, B. Koobus, and M. Lesoinne. Torsional springs for two-dimensional dynamic unstructured fluid meshes. *Computer Methods in Applied Mechanics and Engineering*, 163(1-4):231–245, 1998.
- [4] Charbel Farhat and Vinod K. Lakshminarayanan. An ALE formulation of embedded boundary methods for tracking boundary layers in turbulent fluid-structure interaction problems. *Journal of Computational Physics*, 263:53–70, 2014.
- [5] Charbel Farhat, Michel Lesoinne, and Nathan Maman. Mixed explicit/implicit time integration of coupled aeroelastic problems: Three-field formulation, geometric conservation and distributed solution. *International Journal for Numerical Methods in Fluids*, 21(10):807–835, 1995.
- [6] Charbel Farhat, Arthur Rallu, and Sriram Shankaran. A higher-order generalized ghost fluid method for the poor for the three-dimensional two-phase flow computation of underwater implosions. *Journal of Computational Physics*, 227(16):7674–7700, 2008.
- [7] Farhat Research Group. SDesign: A mesh parametrization Software.
- [8] S. K. Godunov. A finite difference method for the computation of discontinuous solutions of the equations of fluid dynamics. *Matematicheskii Sbornik*, 47:357–393, 1959.
- [9] Farhat Research Group. Aero-F: A multi purpose flow solver.
- [10] Farhat Research Group. Aero-S: A multi purpose structure solver.
- [11] Ami Harten. High Resolution Schemes for Hyperbolic Conservation Laws. *Journal of Computational Physics*, 135:260–278, 1983.
- [12] Adam Larat. The embedded boundary method for turbulent flows - Internal FRG report. pages 1–38, 2012.

BIBLIOGRAPHY

- [13] Michel Lesoinne, Marcus Sarkis, Ulrich Hetmaniuk, and Charbel Farhat. A linearized method for the frequency analysis of three-dimensional fluid/structure interaction problems in all flow regimes. *Computer Methods in Applied Mechanics and Engineering*, 190(24):3121–3146, 2001.
 - [14] Randall J. LeVeque. *Numerical Methods for Conservation Laws*, volume 33. Birkhäuser Basel, 1992.
 - [15] Frank Losasso and R. Fedkiw. Simulating Water and Smoke with an Octree Data Structure. pages 457–462, 2003.
 - [16] Alexander Main. *Implicit and higher-order discretization methods for compressible multi-phase fluid and fluid-structure problems*. Phd thesis, Stanford University, 2014.
 - [17] Alexander Main and Charbel Farhat. A second-order time-accurate implicit finite volume method with exact two-phase Riemann problems for compressible multi-phase fluid and fluid-structure problems. *Journal of Computational Physics*, 258(C):613–633, 2014.
 - [18] K. Maute, M. Nikbay, and C. Farhat. Coupled analytical sensitivity analysis and optimization of three-dimensional nonlinear aeroelastic systems. *AIAA Journal*, 39(11):2051–2061, 2001.
 - [19] K. Maute, M. Nikbay, and C. Farhat. Sensitivity analysis and design optimization of three-dimensional non-linear aeroelastic systems by the adjoint method. *International Journal for Numerical Methods in Engineering*, 2003.
 - [20] Charles Peskin. Flow patterns around heart valves: A numerical method. *Journal of Computational Physics*, 271(0021-9991):252–271, 1972.
 - [21] Serge Piperno and Charbel Farhat. Design of Efficient Partitioned Procedures for the Transient Solution of Aeroelastic Problems. *Revue Européenne des Éléments Finis*, 9(6-7):655–680, jan 2000.
 - [22] P. Roe. Approximate Riemann solvers, parameter vectors, and difference schemes. *Journal of Computational Physics*, 372:357–372, 1981.
 - [23] K. Schittkowski, C. Zillober, and R. Zotemantel. Numerical comparison of nonlinear programming algorithms for structural optimization. *Structural Optimization*, 7(1-2):1–19, 1994.
 - [24] J. A. Sethian. *Level Set Methods and Fast Marching Methods*. Cambridge University Press, Berkeley, 1999.
 - [25] Jaroslaw Sobieszczanski-Sobieski. Sensitivity of complex, internally coupled systems. *AIAA Journal*, 28(1):153–160, 1990.
 - [26] P. R. Spalart and S. R. Allmaras. A one-equation turbulence model for aerodynamic flows. *La Recherche Aerospatiale*, 1(1):5–21, 1994.
-

BIBLIOGRAPHY

- [27] G. D. van Albada, B. van Leer, and W. W. Roberts. A Comparative Study of Computational Methods in Cosmic Gas Dynamics. *Astronomy and Astrophysics*, 108:76–84, 1982.
- [28] Bram van Leer. Towards the ultimate conservative difference scheme. V. A second-order sequel to Godunov’s method. *Journal of Computational Physics*, 32(1):101–136, 1979.
- [29] Guanyuan Wang. *A computational framework based on an embedded boundary method for nonlinear multi-phase fluid-structure interactions*. PhD thesis, Stanford University, 2011.
- [30] K. Wang, J. Grétarsson, A. Main, and C. Farhat. Computational algorithms for tracking dynamic fluid-structure interfaces in embedded boundary methods. *International Journal for Numerical Methods in Fluids*, 70(4):515–535, oct 2012.
- [31] K. Wang, A. Rallu, J.-F. Gerbeau, and C. Farhat. Algorithms for interface treatment and load computation in embedded boundary methods for fluid and fluid-structure interaction problems. *International Journal for Numerical Methods in Fluids*, 67(9):1175–1206, nov 2011.